



National Library  
of Canada

Bibliothèque nationale  
du Canada

Canadian Theses Service

Services des thèses canadiennes

Ottawa, Canada  
K1A 0N4

## CANADIAN THESES

### NOTICE

The quality of this microfiche is heavily dependent upon the quality of the original thesis submitted for microfilming. Every effort has been made to ensure the highest quality of reproduction possible.

If pages are missing, contact the university which granted the degree.

Some pages may have indistinct print especially if the original pages were typed with a poor typewriter ribbon or if the university sent us an inferior photocopy.

Previously copyrighted materials (journal articles, published tests, etc.) are not filmed.

Reproduction in full or in part of this film is governed by the Canadian Copyright Act, R.S.C. 1970, c. C-30.

**THIS DISSERTATION  
HAS BEEN MICROFILMED  
EXACTLY AS RECEIVED**

## THÈSES CANADIENNES

### AVIS

La qualité de cette microfiche dépend grandement de la qualité de la thèse soumise au microfilmage. Nous avons tout fait pour assurer une qualité supérieure de reproduction.

S'il manque des pages, veuillez communiquer avec l'université qui a conféré le grade.

La qualité d'impression de certaines pages peut laisser à désirer, surtout si les pages originales ont été dactylographiées à l'aide d'un ruban usé ou si l'université nous a fait parvenir une photocopie de qualité inférieure.

Les documents qui font déjà l'objet d'un droit d'auteur (articles de revue, examens publiés, etc.) ne sont pas microfilmés.

La reproduction, même partielle, de ce microfilm est soumise à la Loi canadienne sur le droit d'auteur, SRC 1970, c. C-30.

**LA THÈSE A ÉTÉ  
MICROFILMÉE TELLE QUE  
NOUS L'AVONS REÇUE**

THE UNIVERSITY OF ALBERTA

POTENTIOMETRIC SURFACE ANOMALIES DUE TO FLOW THROUGH HIGHLY  
PERMEABLE, LENTICULAR CLASTIC ROCKS AND THEIR APPLICATION IN  
PETROLEUM EXPLORATION

by

 Kaushik Rakhit

A THESIS

SUBMITTED TO THE FACULTY OF GRADUATE STUDIES AND RESEARCH  
IN PARTIAL FULFILMENT OF THE REQUIREMENTS FOR THE DEGREE  
OF MASTER OF SCIENCE

DEPARTMENT OF GEOLOGY

EDMONTON, ALBERTA

SPRING 1987

Permission has been granted to the National Library of Canada to microfilm this thesis and to lend or sell copies of the film.

The author (copyright owner) has reserved other publication rights, and neither the thesis nor extensive extracts from it may be printed or otherwise reproduced without his/her written permission.

L'autorisation a été accordée à la Bibliothèque nationale du Canada de microfilmer cette thèse et de prêter ou de vendre des exemplaires du film.

L'auteur (titulaire du droit d'auteur) se réserve les autres droits de publication; ni la thèse ni de longs extraits de celle-ci ne doivent être imprimés ou autrement reproduits sans son autorisation écrite.

ISBN 0-315-37791-7

THE UNIVERSITY OF ALBERTA

RELEASE FORM

NAME OF AUTHOR      Kaushik Rakhit  
TITLE OF THESIS      POTENTIOMETRIC SURFACE ANOMALIES DUE TO FLOW  
THROUGH HIGHLY PERMEABLE, LENTICULAR CLASTIC  
ROCKS AND THEIR APPLICATION IN PETROLEUM  
EXPLORATION

DEGREE FOR WHICH THESIS WAS PRESENTED      MASTER OF SCIENCE

YEAR THIS DEGREE GRANTED      SPRING 1987

Permission is hereby granted to THE UNIVERSITY OF ALBERTA LIBRARY  
to reproduce single copies of this thesis and to lend or sell such copies for private,  
scholarly or scientific research purposes only.

The author reserves other publication rights, and neither the thesis nor extensive  
extracts from it may be printed or otherwise reproduced without the author's written  
permission.

(SIGNED) 

PERMANENT ADDRESS:

5428 Ladbroke Dr., S.W.

Calgary, Alberta

(403) 249-8793

DATED Jan. 11 1987

THE UNIVERSITY OF ALBERTA  
FACULTY OF GRADUATE STUDIES AND RESEARCH

The undersigned certify that they have read, and recommend to the Faculty of Graduate Studies and Research, for acceptance, a thesis entitled POTENTIOMETRIC SURFACE ANOMALIES DUE TO FLOW THROUGH HIGHLY PERMEABLE, LENTICULAR CLASTIC ROCKS AND THEIR APPLICATION IN PETROLEUM EXPLORATION submitted by Kaushik Rakhit in partial fulfilment of the requirements for the degree of MASTER OF SCIENCE.

*T. J. Ott*

Supervisor

*Frank W. Schwartz*  
*Frederick J. ...*

Date *Jan. 9, 1987*

## ABSTRACT

A highly permeable 'lenticular' rock body within a less permeable matrix, will distort the fluid-potential field and hence the formation-fluid flow directions in the vicinity of the lens. The effect is comparable to that of iron masses on the earth's magnetic field or electrically conductive bodies on telluric currents and potentials. As a result, fluid-flow lines converge towards the permeable body and flow rates increase through it. Consequently, negative potential (and formation pressure) anomalies are generated at the upstream end of a permeable body, and positive potential anomalies at its downstream end, with little drop in potential across it. Theoretical analyses of potentiometric anomalies indicate that their areal extent and magnitude are directly proportional to the hydraulic gradient, and highly sensitive to the geometry of the permeable body and its permeability contrast with the surrounding matrix.

An initial field investigation was conducted by mapping the potentiometric surface of the Bow Island Formation in southern Alberta, which shows several anomalies possibly attributable to the effect of lenticularity. Detailed geological studies at two areas of such anomalies, Keho Lake and Chin Lakes have confirmed the presence of highly permeable sandstone lenses, which are also hydrocarbon reservoirs. The cause-and-effect relation between the lenses and the potentiometric anomalies has been verified by numerical simulation of fluid-flow. Furthermore, the results indicate that under a sufficient hydraulic gradient (i.e. greater than  $10\text{m/km} \sim 0.01$ ) and with sufficient permeability contrast between lens and matrix (generally greater than 100 times) the fluid potential distortion may be detected by formation pressure measurement, provided that an acceptable data point density exists.

The method of analysis developed during this study could prove to be an effective exploration tool for discontinuous lenticular reservoirs that are difficult to detect seismically or by wide spaced drilling and established mapping techniques. It is best suited to areas that have already undergone an initial phase of exploration and offer good data distribution. Other applications may include delineation of pool boundaries and reservoir development planning.

## ACKNOWLEDGEMENTS

The many delightful discussions with colleagues too numerous to mention and the study leading to the preparation of this manuscript have, upon reflection, been the most stimulating of my education. I am deeply grateful to my mentor Dr. J. Tóth for providing me with the opportunity of doing this study. The enthusiasm with which he undertakes his science served as constant inspiration through the late-nights, disappointments, triumphs and sometimes, monotony inherent with graduate work. Patient review and the many useful comments forwarded by my advisory committee of Dr. F.W. Schwartz, Dr. G.S. Pemberton and Dr. F.W. Jones have been invaluable in improving the original manuscript. However, any omissions or misinterpretations contained within are solely my responsibility.

This study has been supported by a Geological Research Grant from Texaco Canada Ltd., a Grant-In-Aid from the American Association of Petroleum Geologists and a scholarship from the Canadian Society of Petroleum Geologists. Drill stem test data provided by the Canadian Institute of Formation Evaluation (Calgary, Alta.) and permeability analyses conducted by Core Labs (Calgary, Alta.) are gratefully acknowledged.

I am also much indebted to my friends and colleagues J.T. Freeman and D. Barson for their constant support and willing help throughout this undertaking.

## Table of Contents

Chapter	Page
1. INTRODUCTION .....	1
1.1 THESIS OBJECTIVES.....	2
2. FLUID MECHANICS THEORY AND FIELD IMPLEMENTATION .....	4
2.0.1 DARCY'S LAW .....	4
2.1 Fluid Potential, Hydraulic Head and Formation Pressure .....	8
2.1.1 Determining Hydraulic Head From Drill Stem Test Pressure Measurements .....	8
2.1.2 Calculating $P_{max}$ By The Horner Method .....	9
2.1.3 Permeability Calculations From Drill Stem Tests .....	11
2.1.4 Equations of Groundwater Flow .....	12
3. THE LENS ASSOCIATED POTENTIAL ANOMALY .....	18
3.1 ANALYTICAL SOLUTION-Governing Equation .....	19
3.1.1 Solution and Interpretation .....	20
3.2 DESCRIPTIVE NOMENCLATURE OF POTENTIAL ANOMALIES .....	23
3.2.1 Anomaly .....	23
3.2.2 Anomaly Threshold .....	23
3.2.3 Relative Anomaly .....	24
3.2.4 Glossary Of Variables .....	24
3.3 NUMERICAL SOLUTION-The Finite Difference Method .....	24
3.3.1 Implementation Of The USGS Groundwater Flow Model .....	26
3.3.2 Output Processing .....	27
3.4 COMPARISON OF NUMERICAL AND ANALYTICAL SOLUTIONS .....	30
3.5 NUMERICAL SIMULATIONS .....	31
3.5.1 Effects Of Varying Permeability Contrast And Geometry On The Anomaly .....	33
3.5.2 Areal Extent Of Anomalies .....	33
3.5.3 Effect of Varying Flow Directions On Anomalies .....	36



3.5.4 Effect Of Vertical Anisotropy .....	37
3.5.5 Multiple Lens Configurations .....	37
3.6 THE LENS AS A FOCAL AND TRAPPING MECHANISM FOR HYDROCARBONS .....	39
4. FIELD STUDIES .....	51
4.1 STUDY AREA .....	51
4.2 REGIONAL BOW ISLAND FORMATION GEOLOGY .....	51
4.2.1 Regional Structure .....	51
4.2.2 Regional Stratigraphy And Lithology .....	52
4.3 REGIONAL HYDRODYNAMICS .....	53
4.3.1 The Erosional Rebound Theory .....	56
4.3.2 Effects Of Complex Flow Systems .....	57
4.4 POTENTIOMETRIC SURFACE MAPPING .....	63
4.4.1 Potentiometric Surfaces - First Bow Island S.S. and Second White Specks S.S. ....	63
4.4.2 Method Of Selection And Study Of Potentiometric Anomalies .....	64
4.5 KEHO LAKE STUDY AREA .....	69
4.5.1 Keho Lake Study - Geology .....	69
4.5.2 Potentiometric Surface and Interval Permeability Distribution .....	70
4.5.3 Verification of Observed Anomaly By Numerical Simulation .....	71
4.5.4 Predictive Modelling-Inferred Permeability Distribution .....	72
4.5.5 Fluid Distribution .....	74
4.6 CHIN LAKES STUDY AREA .....	88
4.6.1 Geology .....	88
4.6.2 Detailed Potentiometric Surface .....	89
4.6.3 Permeability Distribution .....	89
4.6.4 Verification of Anomaly by Numerical Simulation .....	90
4.6.5 Fluid Distribution .....	91

CONCLUSIONS AND DISCUSSION .....	103
REFERENCES .....	105
5. APPENDICES .....	114
Appendix 2A.1 - Schematic charts for determination of DST quality .....	115
Appendix 2A.2 - Schematic charts for qualitative DST permeability determination .....	116
Appendix 2B.1 - DST description for the WESTCOAST TABERS 15-36-8-18W4M well ...	117
Appendix 2B.2 - DST description for THE GNOC CIGOL TABERS 6-15-8-17W4M well	126
Appendix 3A - Glossary of Terms .....	135
Appendix 3B.1 - Input data for the USGS-GWFM Basic Package .....	138
Appendix 3B.2 - Input data for the USGS-GWFM Block Centered Flow Package .....	140
Appendix 3C - Potentiometric surface and anomaly maps for various numerical simulations. ....	141
Appendix 4A - Regional potentiometric surface maps from which the hydraulic cross-section A-A' (Figure 4.4) was constructed. ....	151
Appendix 4B.1 - Description of cores logged in the Keho Lake study area .....	155
Appendix 4B.2 - Description of cores logged in the Chin Lakes study area .....	163

## List of Tables

Table	Page
3.1 Comparison of relative anomalies calculated analytically ( $AN_{\Delta\Phi_r}$ ) and numerically numerically ( $NM_{\Delta\Phi_r}$ ) for ellipses approximated by rectangles. ....	32
3.2 Calculated relative anomalies ( $\Delta\Phi_r$ ) for lenses of varying L:W, hydraulic conductivity contrast $\epsilon$ , and potential gradients. ....	34
3.3 Approximate conductivity contrast ( $\epsilon$ ) required for a rectangular lens of varying L:W to attain $\Delta\Phi_r$ levels of 0.25, 0.5, 0.75 and 0.9. ....	35
4.1 Averaged formation water salinities through study area. ....	55
4.2 Intervals and locations of cores logged in the Keho Lake study area. ....	75
4.3 Intervals and locations of cores logged in the Chin Lakes study area. ....	92

## List of Figures

Figure	Page
1.1 Flow chart outlining thesis approach. ....	3
2.1 Experimental apparatus for the illustration of Darcy's Law (adapted from Freeze and Cherry 1979). ....	6
2.2 Data for calculation of mechanical energy of unit mass of fluid (adapted from Freeze and Cherry 1979). ....	14
2.3 Relationship of hydraulic head to pressure head (adapted from Hubbert, 1953). ....	15
2.4 Typical dual shut-in drill stem test chart (from Johnston, 1962). ....	16
2.5 Elemental control volume for flow through porous media (from Freeze and Cherry 1979). ....	17
3.1 Calculated potential distribution around an ellipsoid of permeability $k'$ placed in an infinite homogeneous medium of permeability $k$ (adapted from Tóth, 1962). ....	21
3.2 Calculated anomalies ( $\Delta\Phi$ ) of an infinite-uniform potential field, at the endpoints of ellipsoidal bodies of varying properties, $e$ is the eccentricity of the ellipse and $\epsilon$ is the permeability contrast between the ellipse and its surrounding matrix, (adapted from Tóth, 1962). ....	22
3.3 Illustration of the concepts of anomaly ( $\Delta\Phi$ ), threshold anomaly ( $\Delta\Phi_{\epsilon_t}$ ) and relative anomaly ( $\Delta\Phi_r$ ). $\Phi_a$ is the distorted hydraulic head at $P_1$ and $\Phi_o$ is the original undistorted head. $L$ is the length of the lens parallel to flow and $\ell$ is the distance from the endpoint of the lens to $P_1$ at which $\Delta\Phi$ is calculated. $\Delta\Phi_r$ is calculated at ( $\ell=0$ ) eg. at $P_1$ and is equal to unity at a permeability contrast between lens and matrix of greater than $\epsilon_t$ . ....	25
3.4 Flow chart outlining the procedure for using the USGS Groundwater Flow Model. ....	28
3.5 Discretized model of an ellipse which is used for the numerical simulation of flow. Flow occurs normal to constant head boundaries and parallel to no flow boundaries. Node points are the locations at which solutions for hydraulic head are obtained. The mesh dimension is 24 columns by 22 rows. ....	29
3.6 Ellipses of varying eccentricity solved for analytically and their substitute geometry for numerical simulation. ....	41
3.7 Family of curves indicating the relative anomaly $\Delta\Phi_r$ produced by ellipsoidal bodies (discretized by a rectangular mesh) of varying properties - NUMERICAL SOLUTION. The permeability contrast required to obtain $\Delta\Phi_r = 0.95$ ( $\Delta\Phi_r = \Delta\Phi/\Delta\Phi_{\epsilon_t}$ ) is $\epsilon_t$ . ....	42

Figure	Page
3.8 Family of curves indicating the relative anomaly $\Delta\Phi_r$ produced by ellipsoidal bodies of varying properties - ANALYTICAL SOLUTION. ....	42
3.9 Potentiometric surface and anomaly maps for lens of $L:W = 2:1$ (a,b) and $L:W = 5:1$ (c,d), $\epsilon = 100$ , $\frac{\partial\phi}{\partial x} = 0.02$ , flow is from right to left. ....	43
3.10 Anomaly attenuation parallel to flow and normal to flow measured from the extremities of a body $L:W = 1:1$ , (a). Anomaly attenuation parallel to flow for varying $L:W$ ratios. Note that the anomaly attains a maximum magnitude at a distance of $\ell/L = 0.05-0.1$ from the end of the lens. $L$ is the length of the lens and $\ell$ is the distance from the end of the lens at which the attenuation is calculated. ....	44
3.11 Changes in $\Delta\Phi$ due to rotation of lens with respect to flow direction. ....	45
3.12 Potentiometric surface and anomaly maps illustrating the effect of vertical anisotropy, isotropic a, b and $k_h = 2Xk_v$ c, d. Flow is from right to left. ....	46
3.13 Potentiometric surface and anomaly maps illustrating the effect of vertical anisotropy, $k_h = 5Xk_v$ a, b and $k_h = 10Xk_v$ c, d. Flow is from right to left. ....	47
3.14 Potentiometric surface and anomaly maps due to interference effect of adjacent lenses, separation $\ell/L = 1/6$ for two lenses of $L:W = 5:1$ a, b, and for a lens of $L:W = 3:1$ adjacent to a lens of $L:W = 5:1$ c,d. ....	48
3.15 Attenuation of anomaly shift from the interference of adjacent lenses as they undergo separation a) parallel to flow and b) normal to flow. ....	49
3.16 Illustration of the conditions of relative permeability and impelling forces due to capillarity at sand-shale interfaces (from Tóth, 1970). ....	50
4.1 Study area in regional context. ....	58
4.2 Table of formations, showing correlative stratigraphy, adapted from Stelck, 1981. ....	59
4.3 Regional structural elements given on top of the Base of Fish Scales Marker, structural contours modified from the E.R.C.B. Area No.1, 1978 and Area No.2, 1969 maps. ....	60
4.4 Regional hydraulic cross-section A-A' (from Tóth and Corbet, 1986), location given in Figure 4.3 ....	61
4.5 Conceptual evolution of hydraulic head distribution in simple basin at times : a) $t_0$ , b) $t_1$ , c) $t_2$ and d) $t_\infty$ , adapted from Tóth and Corbet, 1986. ....	62

4.6	Potentiometric surface of the Bow Island Formation. Circular points are hydraulic head values calculated near the top of the Bow Island, the square points are values influenced by production induced drawdown. ....	67
4.7	Potentiometric surface of the Second White Specks zone. The square data points appear to be influenced by production induced drawdown, and the hexagonal points are anomalously super-hydrostatic. These were not used in the contouring. ....	68
4.8	Keho Lake study area location map. ....	76
4.9	Composite strip log through Keho Lake area, of average permeability range, typical geology with corresponding gamma ray, spontaneous potential and resistivity log responses. The cross-hatched and solid areas are estimated and observed permeability ranges, respectively. ....	77
4.10	Structural cross-section B-B', the correlations are based on gamma-ray logs, see Figure 4.8 for location. ....	78
4.11	Structural cross-section C-C', the correlations are based on gamma-ray logs, see Figure 4.8 for location. ....	79
4.12	Structural contours relative to sea level on top of the Bow Island Formation, elevations obtained from borehole logs. ....	80
4.13	Observed potentiometric surface, top of the BIS 1 sandstone, squares represent values influenced by production induced drawdown. ....	81
4.14	Interval permeability distribution for the BIS 1 sandstone and conglomerate. Solid data points are permeabilities calculated and estimated from DST's, solid squares and squares are core derived and estimated permeabilities from lithology as correlated to borehole logs. ....	82
4.15	Discretized model of the Keho Lake study area (using the interval permeability distribution of Figure 4.14) and the calculated potentiometric surface. ....	83
4.16	Relative permeability relations of fluids to varying saturations, adapted from Golubev, 1959. ....	84
4.17	Calculated potentiometric surface based on the inferred permeability distribution. ....	85
4.18	Inferred permeability distribution after three iterations adjusting the interpretation of the observed permeability distribution... the trial and error method of "inverse modelling." ....	86

4.19	Fluid distribution and apparent contact relationships within the study area. Pool outlines at $A_{1,2}$ were obtained from the E.R.C.B. Oil and Gas Pools Map, 1981, and only represent the locations of established hydrocarbon reserves, not the actual reservoir boundaries. Locations $A_{1,2}$ are based on hydrocarbon distribution defined during the present study. ....	87
4.20	Location map of Chin Lakes study area. ....	93
4.21	Structural Cross-Section D-D' (see Figure 4.20 for location), correlations are based on gamma-ray log response. ....	94
4.22	Structural Cross-Section E-E' (see Figure 4.20 for location), correlations are based on gamma-ray log response. ....	95
4.23	Structural contours relative to sea level on top of the Bow Island Formation, elevations were determined from borehole logs. ....	96
4.24	Composite strip log of the Chin Lakes study area indicating typical permeability range and lithology with corresponding gamma-ray, spontaneous-potential and resistivity log responses. The cross-hachured and solid areas represent estimated and observed permeability ranges, respectively. ....	97
4.25	Detailed potentiometric surface distribution for the upper BIS 1 sandstone, squares designate values influenced by production induced drawdown. ....	98
4.26	Interval permeability distribution for the BIS 1 sandstone and conglomerate. Solid data points are permeabilities calculated (numbers) and estimated (qualitative range). The designations $L_{1,1,1}$ ... and $S_1$ are for the main permeable trends defined in the area. ....	99
4.27	Production history (from the E.R.C.B. of Alberta), indicating the DST date, cumulative production if any, and date production started. ....	100
4.28	Discretized model and the calculated potentiometric surface distribution of Chin Lakes study area. The permeability distribution used is from Figure 4.26, $k_r = 0.1 k_e$ was used due to gas at $L_1$ . ....	101
4.29	Fluid distribution and apparant contact relationships observed in the Chin Lakes study area. Designations $A_{1,2,3}$ ... refer to areas that have corresponding potentiometric surface anomalies. Reservoir outlines shown are based on E.R.C.B. Oil and Gas Pool Maps (1981). ....	102
5.1	Potentiometric surface and anomaly maps for lenses of $L:W = 5:4$ and $10:1$ and $\epsilon = 100$ , flow is from right to left. ....	142
5.2	Potentiometric surface and anomaly maps for a lens of $L:W = 2:1$ and flow at $45^\circ$ a, b and $90^\circ$ c, d. ....	143
5.3	Potentiometric surface and anomaly maps for a lens of $L:W = 5:1$ and flow at $45^\circ$ a, b and $90^\circ$ c, d. ....	144

Figure	Page
5.4 Multiple lens configurations used to determine interference effects (anomaly shift $\Delta\Phi_i$ ) with, horizontal separation (a-d) and vertical separation (e-g) . . . . .	145
5.5 Multiple lens configurations used to determine reduction in anomaly shift ( $\Delta\Phi_i$ ) with progressive overlap of subjacent lenses. . . . .	146
5.6 Potentiometric surface and anomaly maps due to interference effect of adjacent lenses, separation $\ell/L = 1/6$ a, b and $\ell/L = 1/2$ c, d. . . . .	147
5.7 Potentiometric surface and anomaly maps for subjacent lens with vertical separation of $\ell/L = 1/4$ a, b and $\ell/L = 3/5$ c, d. . . . .	148
5.8 Potentiometric surface and anomaly maps for subjacent lenses with a vertical separation of $\ell/L = 2/5$ and overlap of 20% a, b and 50% c, d. . . . .	149
5.9 Potentiometric surface and anomaly maps for subjacent lenses with 100% overlap and vertical separation of $\ell/L = 3/5$ a, b and $4/5$ c, d. . . . .	150
5.10 Potentiometric surface of the Milk River Formation, adapted from Tóth and Corbet, 1986. . . . .	151
5.11 Potentiometric surface of the Bow Island Formation, adapted from Tóth and Corbet, 1986. . . . .	152
5.12 Potentiometric surface of the Lower Mannville Group, adapted from Tóth and Corbet, 1986. . . . .	153
5.13 Potentiometric surface of the Ellis Group, adapted from Tóth and Corbet, 1986. . . . .	154



## 1. INTRODUCTION

In the subsurface geologic environment, fluids saturating the rock framework move due to a variety of forces exerted on them. These forces arise from mechanical, chemical, thermal and fluid-potential gradients created by geologic, tectonic, geomorphological and meteoric processes. Of these, a fluid-potential gradient is perhaps the major process controlling groundwater motion in a mature sedimentary basin where compaction and primary migration is no longer significant. Whether a fluid-potential gradient is gravity induced (from water table topography), dilational (from uplift or erosion, i.e. unloading) or due to loading (by deposition, glaciation or tectonic forces), it is detectable in the subsurface by measuring formation pressures and calculating the fluid-potential or hydraulic head. The ability of the fluid to move and the path it takes under the impetus of a potential gradient depends upon the permeability of the rock framework and physical properties of the fluid.

The laws governing fluid-flow in a hydraulic system are similar to those of thermal, electrical and magnetic systems. In each case, materials with differing thermal or electrical conductivities and magnetic susceptibility occurring within a homogeneous medium will distort an otherwise uniform potential field. This principle is widely used in geophysical exploration (see Telford et al, 1977), where economic minerals with physical properties differing from those of their host rock are detected by various geophysical techniques. An example is the distortion of the earth's magnetic field by an ultramafic dike emplaced within leucocratic or sedimentary rock. In this case the difference in the magnetic susceptibility of the rocks will distort the otherwise uniform magnetic field of the earth. The contrast in the magnetic susceptibility between the dike and its surroundings, the geometry of the dike and its attitude with respect to the magnetic field will determine the magnitude and shape of the distortion.

Isolated, lenticular bodies, commonly associated with sandstone deposition (i.e. channel sands, point bars, barrier bars, offshore bars etc.) and in some cases with biostromal bodies in carbonates, are widely sought in hydrocarbon exploration and provide prolific and subtle petroleum reservoirs in western Canada and the continental United States. They are difficult to detect by seismic methods and, due to their erratic areal distribution, are easily

missed by widely spaced drill holes, often requiring dense, possibly random, wildcat drilling for their discovery. In cases where a hydraulic gradient occurs across the medium containing the lenticular reservoir, a distortion of the otherwise uniform potentiometric surface will occur, as in the analogy of the dike in the earth's magnetic field. If this potentiometric distortion is detectable, then its measurement and correct interpretation may provide a successful exploration method.

## 1.1 THESIS OBJECTIVES

The objective of studying the lens associated fluid-potential anomaly is to determine the feasibility of using this physical phenomenon as a petroleum exploration tool. The approach used is best summarized by the flow chart shown in Figure 1.1. Chapter 2 is basically a review of the physical laws governing groundwater flow through porous media and the method of applying these laws to field studies. It is intended as a reference for those unfamiliar with the principles of hydrogeology and drill stem testing. The nature of the lens associated fluid-potential anomaly is analyzed by a two-step approach in Chapter 3: first, analytical solutions for relatively simple mathematical models are obtained and used to compare and calibrate a numerical code and second, the numerical code is used to determine the relationship between varying geologic and hydraulic parameters. Chapter 4 uses the knowledge gained from the theoretical considerations for the study of potentiometric anomalies in the field.

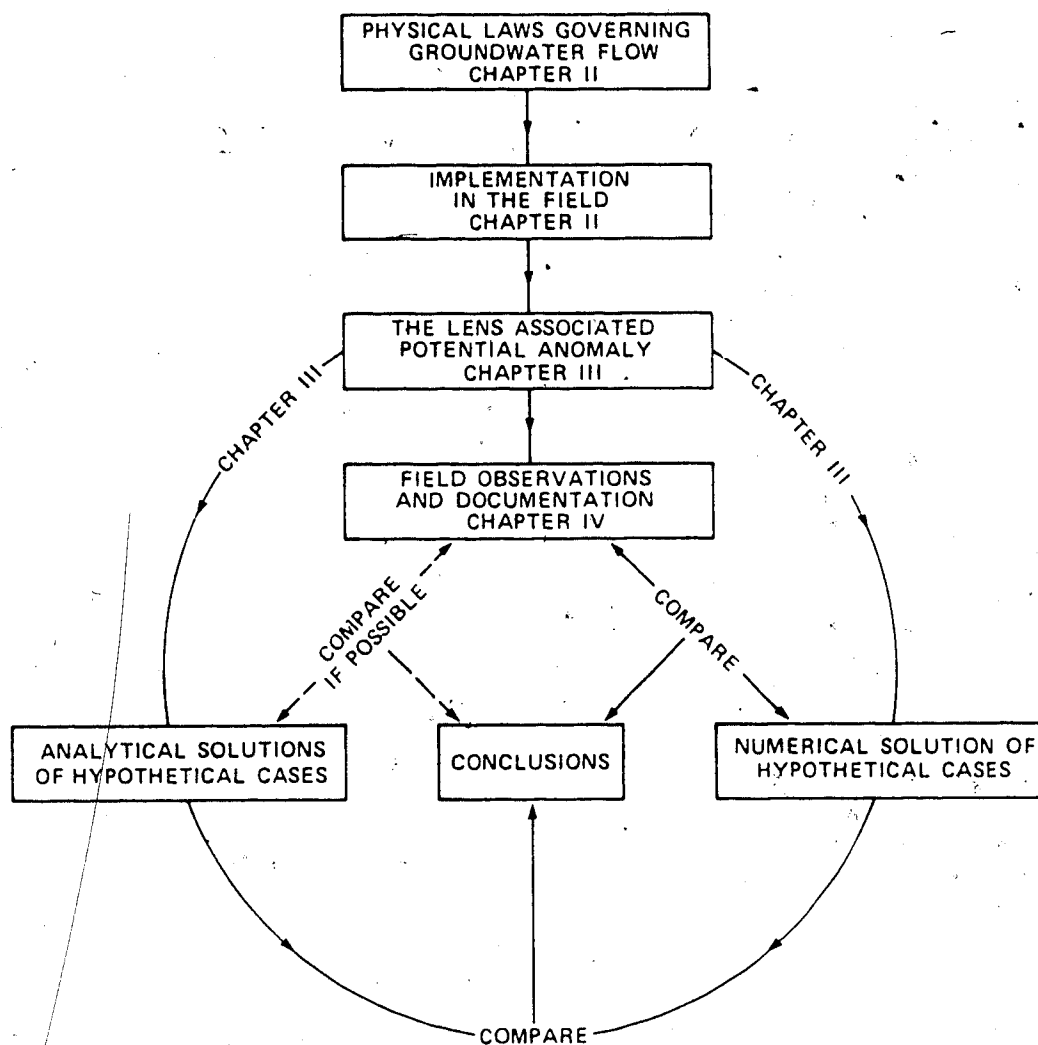


Figure 1.1 Flow chart outlining thesis approach.

## 2. FLUID MECHANICS THEORY AND FIELD IMPLEMENTATION

The analysis of a physical process or system involving flow requires the recognition and documentation of an energy gradient. In the case of heat flow through solids, the direction of flow is from higher temperatures to lower. Another well known example is the flow of electrons from a higher electric potential to a lower one. In both cases, the temperature and electric potential represent quantities of energy, and the rates of flow are proportional to their gradients and the conductivity of the medium. The following sections consider the laws governing fluid-flow in a porous medium and how the various hydraulic-dynamic parameters are obtained in the field.

### 2.0.1 DARCY'S LAW

Fluid-flow through porous media was first analyzed by Henry Darcy in 1856, with his now classic experiment which provided us with the empirical Darcy's Law. Consider an apparatus as shown in Figure 2.1, a circular cylinder filled with sand, the ends of which contain inflow and outflow tubes and manometers. Let  $Q$  equal the volume flow rate through the tube when the sand is completely saturated. Let the arbitrary datum be  $z=0$ , the elevations of the manometer intakes be  $z_1$  and  $z_2$ , the elevations of the fluid levels be  $h_1$  and  $h_2$ , and the distance between the manometer intakes be  $\Delta l$ . The volumetric rate of flow or specific discharge is then equal to:

$$v = \frac{Q}{A} \quad (2.1)$$

where  $Q$  is in  $[L^3/T]$ ,  $A$   $[L^2]$  and  $v$  has dimensions  $[L/T]$ . By means of this apparatus Darcy found the empirical relationship, now referred to as Darcy's Law :

$$v = -K \frac{dh}{dl} \quad (2.2)$$

or

$$Q = -K \frac{dh}{dl} A \quad (2.3)$$

In Eq. (2.2) and Eq. (2.3)  $h$  is the hydraulic head and  $dh/dl$  is the hydraulic gradient. By inspection it is seen that the flow rate is proportional to the hydraulic gradient and a constant of proportionality  $K$ , the hydraulic conductivity. The hydraulic conductivity is dependent on

fluid and porous medium properties

$$K = \frac{k \rho g}{\mu} \quad (2.4)$$

where  $k$  is equal to the permeability of the medium,  $\rho$  is the fluid density,  $\mu$  the dynamic fluid viscosity and  $g$  the acceleration due to gravity. The permeability is usually given in darcys, where, 1 darcy(d) =  $10^{-8}$  cm<sup>2</sup>, and is defined as "the permeability leading to a specific discharge of 1 cm/s for a fluid of viscosity 1 Cp (centipoise = m Pa s) under a hydraulic gradient that makes the  $g \, dh/dl$  equal 1 atm/cm" (Freeze and Cherry, 1979, p. 28).

### 2.1 Fluid Potential, Hydraulic Head and Formation Pressure

Hubbert (1940, p.794) defines fluid potential as "a physical quantity, capable of measurement at every point in a flow system, whose properties are such that flow always occurs from regions in which the quantity has higher values to those in which it has lower, regardless of the direction in space." The fluid potential ( $\Phi$ ), is the mechanical energy per unit mass ( $m$ ) at a given point P (Figure 2.2), which is expressed by the general formula (Bernoulli Equation):

$$\Phi = m g z + \frac{m v^2}{2} + m \int_{p_0}^p \frac{dp}{\rho} \quad (2.5)$$

where the first term on the right hand side is the work required to lift a unit mass of fluid from  $z=0$  to point P (at elevation  $z$ ); the second term is the work required to accelerate the fluid from velocity  $v=0$  to velocity  $v$ ; and the third term is the work required to raise the fluid pressure from  $p=p_0$  to  $p$ . Letting  $m=1$ , the equation becomes

$$\Phi = g z + \frac{v^2}{2} + \int_{p_0}^p \frac{dp}{\rho} \quad (2.6)$$

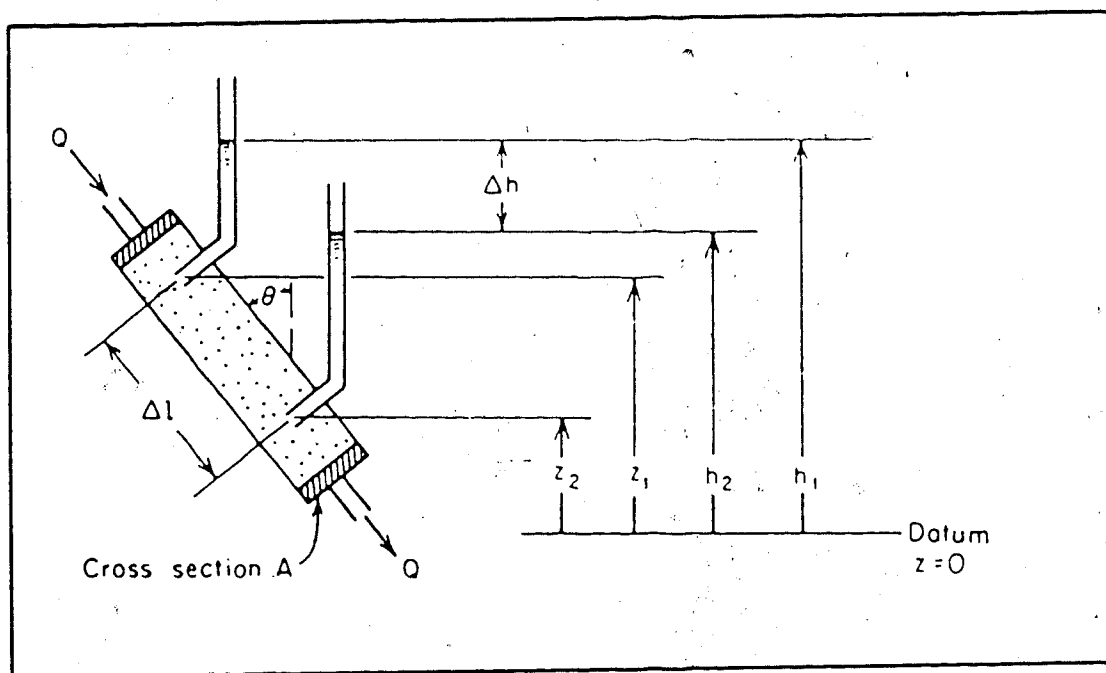


Figure 2.1 Experimental apparatus for the illustration of Darcy's Law (adapted from Freeze and Cherry 1979).

In porous media, flow velocities tend to be extremely slow, so that the second term ( $v^2/2$ ) becomes negligible in most cases and for incompressible fluids (e.g. fluids with constant density)  $\rho$  is not a function of  $p$ . With these two assumptions, Eq.(2.6) reduces to:

$$\Phi = g z + \frac{p - p_0}{\rho} \quad (2.7)$$

It is common in measuring subsurface water levels and pressures to let  $p_0$  = atmospheric pressure and consider the gauge pressure, which further simplifies Eq. (2.7) to:

$$\Phi = g z + \frac{p}{\rho} \quad (2.8)$$

Equation (2.8) describes the fluid potential at any point to be equal to the work required to transport a unit mass of fluid from a standard datum (usually sea level) and atmospheric pressure to the elevation and pressure being considered.

Since the elevation ( $z$ ) and pressure ( $p$ ) can be measured at any point in space (subsurface for this study), it should also be possible to determine the fluid potential at this location. The simplest method of determining and representing fluid potential is to place an open topped manometer terminating at the point (P) (Figure 2.3) where the value of the fluid potential is to be obtained. In Figure 2.3, ( $z$ ) is the elevation of point (P) and ( $p$ ) the pressure of the fluid; also termed pore-pressure or formation-pressure. In response to the formation-pressure the fluid will rise statically in the manometer (piezometer) to a height ( $h$ ) from point (P) above the datum. The relationship between hydraulic head and formation pressure is given by the hydrostatic equation (Hubbert, 1953).

$$\phi = g z + \frac{p - p_0}{\rho} = g z + \frac{\rho g (h - z)}{\rho} = h g \quad (2.9)$$

When this is substituted into Eq. (2.8) the fluid potential is obtained. Since acceleration due to gravity at the earth's surface is approximately the same everywhere, Eq(2.9) suggests that the fluid potential is linearly proportional to the hydraulic head.

From this it can be seen that the manometer (or piezometer) is a device which is capable of measuring the fluid potential at any point. The importance of the fluid potential relationship is best summarized by Hubbert (1953),

*"The potential is determinable not only in space but also at any point capable of being occupied by that fluid. Thus fresh-water potentials have values not only in space saturated with fresh water, but also in space occupied by other fluids such as air, salt water, oil or gas. In each case the potential is the amount of work required to transport a unit mass of fluid to that point from the standard state."*

### 2.1.1 Determining Hydraulic Head From Drill Stem Test Pressure Measurements

In most cases when petroleum exploration wells are drilled it is uneconomic and too time consuming to install a manometer (piezometer) to determine fluid potential or hydraulic head. Instead, a drill stem test (DST) is used, whereby the formation pressure is measured at the point of interest and then converted to hydraulic head using the relationship :

$$h = \frac{p}{\rho g} + z \quad (2.10)$$

For a thorough discussion of drill stem test tools and procedures, the reader is referred to Lynch (1962).



The DST isolates a given section of formation, and allows the formation fluids to enter the drill pipe (that is opened to atmospheric pressure by a system of valves), which provides a temporary completion of the well. Formation pressure and fluid-flow pressure are then systematically recorded by down-hole sensors on a pressure vs. time chart (Figure 2.4). There are two essential components to the test, a) the flow period (pt C-D) and b) the shut-in period (pt D-E). The number and duration of these periods are varied according to specific needs, but present convention is represented by the breakdown of the chart in Figure 2.4. Analysis of the DST allows many reservoir characteristics to be determined (i.e. reservoir pressure, permeability, well bore damage, depletion, radius of investigation and in some cases the presence of barriers to flow). Johnston (1964). Appendix 2A, contains a set of schematic DST charts that may be used as a guide for determining the quality of a DST, and hence its usefulness for reservoir calculations.

### 2.1.2 Calculating $P_{\max}$ By The Horner Method

Stabilized reservoir pressure ( $P_{\max}$ ) can be calculated from the shut-in pressure build-up curve of a DST by constructing a Horner plot. The mathematical background and procedure are discussed in detail by Horner(1951). A brief description of the Horner plot construction procedure is presented below.

The Horner method is based on the solution of the build-up equation or the zero flow equation,

$$P_o - P_f = 2121 \frac{Q \mu B}{k_e b} \log \left( \frac{t_c + \Delta t}{\Delta t} \right) \quad (2.11)$$

where  $P_o$  is the pressure at the drainage radius,  $P_f$  the formation pressure during build-up at the well after an elapsed time ( $\Delta t$ ) counted from the beginning of the shut-in period,  $b$  is the thickness of the producing interval,  $k_e$  the effective permeability to the produced fluid,  $t_c$  the

total time of production at a rate  $Q$  and  $B$  the formation volume factor (which accounts for the change in the volume of a given mass of fluid between formation conditions and atmospheric conditions). When  $\Delta t$  approaches infinity ( $\infty$ ),  $(t_c + \Delta t)/\Delta t$  approaches unity and  $P_o = P_f$ . A straight line fitted through a  $P_f$  vs.  $\log (t_c + \Delta t)/\Delta t$  plot represents the stabilized pressure-build-up and has a slope  $M$  (of  $2121 Q\mu B/k_e b$ ). The intercept of the stabilized pressure-build-up line with  $(t_c + \Delta t)/\Delta t = 1$ , represents  $P_{max}$ , also referred to as the extrapolated pressure or the static formation pressure. These are only an approximation of the formation pressure at the time the DST is conducted. Therefore, when  $P_{max}$  is calculated from a DST, it does not necessarily indicate the "virgin formation pressure", which is the original undisturbed (i.e. unaffected by production or injection of fluids) pressure of the formation. In some cases (such as very small reservoirs), production of reservoir fluids during the flow period of a DST will deplete reservoir pressure, therefore, the extrapolated shut-in-pressure will be less than the virgin reservoir pressure. An example of a DST description, incremental pressure build-up curve and a Horner plot for the WESTCOAST TABERS 15-36-8-18W4M well, which recovered water from the top of the Bow Island Formation, is provided in Appendix 2B.1.

In cases where gas is the fluid recovered during a drill stem test, a slightly different format is used in the Horner analysis, which plots  $(t_c + \Delta t)/\Delta t$  vs.  $(P_f^3/10^6)$ . The extrapolated pressure is determined by plotting a straight line through the stabilized pressure curve and reading  $P_f = (P_o \cdot 10^6)^{1/3}$  at  $(t_c + \Delta t)/\Delta t = 1$ , which is the static reservoir pressure ( $P_{max}$ ). An example of a DST description, incremental pressure build-up and a Horner plot for the GNOC CIGOL TABERS 6-15-8-17W4M well, which recovered gas from the Bow Island Formation is given in Appendix 2B.2.

Once the formation pressure at the zone of interest has been calculated it may be substituted back into Eq. (2.10) and converted into hydraulic head. The calculated hydraulic head value, however, can be affected by external stresses such as reservoir production or injection. These factors must be taken into account when constructing a potentiometric surface map, which should be based on-virgin (original) formation pressures whenever

possible.

### 2.1.3 Permeability Calculations From Drill Stem Tests

The shut-in pressure build-up equation [Eq. (2.11)] allows the calculation of the effective permeability of the zone being tested, if the constants in the equation are known. Assuming that Eq. 2.11 is linear, Horner (1951), the slope of the line (M) is :

$$M = (P_o - P_f) / \log \left( \frac{t_o + \Delta t}{\Delta t} \right) = 2121 \frac{Q \mu B}{k_e b} \quad (2.12)$$

The value of M is obtained from the straight line portion of the Horner plot, as  $\Delta P_f / \log$  cycle. Reorganizing Eq. 2.12 yields the effective permeability ( $k_e$ ) of the tested interval in millidarcy's (md) :

$$k_e = \frac{2121 \cdot Q \mu B}{M b} \quad (2.13)$$

For wells that produce gas the permeability equation takes the form :

$$k_e = \frac{1491 \cdot Q \mu T Z}{M b} \quad (2.14)$$

where Z equals the gas deviation factor (from the perfect gas law), T the temperature in degrees Kelvin ( $^{\circ}\text{K} = ^{\circ}\text{C} + 273$ ) and M the build up constant (slope) for gas, which is equal to

$$(P_o^2 - P_f^2) / \log \left( \frac{t_o + \Delta t}{\Delta t} \right) \quad (2.15)$$

Most of the permeability calculations used in this study were determined using the above method. Appendix 2B.1 and 2B.2 contains a list of the calculated permeabilities for the 15-36-8-18W4M and 6-15-8-17W4M wells which produced water and gas respectively.

#### 2.1.4 Equations of Groundwater Flow

When Darcy's Law is coupled with the equation of continuity, which describes the conservation of fluid mass during flow through a porous medium, a partial differential equation describing groundwater flow results.

If a unit volume of saturated porous medium (elemental control volume) is considered, the law of mass conservation for steady-state flow requires that the rate of fluid mass flow into the elemental control volume must be equal to the rate of flow out of that volume. The concept is illustrated in Figure 2.5 and is described mathematically by the 'equation of continuity.'

$$0 = -\frac{\partial(\rho v_x)}{\partial x} - \frac{\partial(\rho v_y)}{\partial y} - \frac{\partial(\rho v_z)}{\partial z} \quad (2.16)$$

The quantity  $\rho v$  has the dimension of mass rate of flow across a unit cross-sectional area of the elemental control volume. For incompressible fluids,  $\rho(x,y,z)$  is constant and the  $\rho$ 's can be removed from Eq. (2.16). Even if the fluid is compressible, that is  $\rho(x,y,z)$  is not constant, the terms of the form  $\rho \partial v_x / \partial x \gg v_x \cdot \partial \rho / \partial x$  (which arise when Eq. (2.16) is expanded using the chain rule), because the change in fluid velocity is much greater than the change in fluid density due to flow. Therefore, Eq. 2.16 can be simplified to :

$$0 = -\frac{\partial v_x}{\partial x} - \frac{\partial v_y}{\partial y} - \frac{\partial v_z}{\partial z} \quad (2.17)$$

Recalling Darcy's Law [Eq. (2.2)], which is valid for flow in any direction, and substituting for  $v_x$ ,  $v_y$  and  $v_z$  into Eq. (2.17) yields the equation of steady state flow through an anisotropic saturated porous medium :

$$0 = \frac{\partial}{\partial x} \left( K_x \frac{\partial h}{\partial x} \right) + \frac{\partial}{\partial y} \left( K_y \frac{\partial h}{\partial y} \right) + \frac{\partial}{\partial z} \left( K_z \frac{\partial h}{\partial z} \right) \quad (2.18)$$

For a homogeneous, isotropic medium  $K(x,y,z)$  is constant and  $K_x=K_y=K_z$ , so that Eq. (2.18) can be reduced to the Laplace Equation :

$$0 = \frac{\partial^2 h}{\partial x^2} + \frac{\partial^2 h}{\partial y^2} + \frac{\partial^2 h}{\partial z^2} \quad (2.19)$$

The solution of Equations (2.18 and 2.19) is a function of  $h(x,y,z)$ , which describes the hydraulic head ( $h$ ) at any point in a three-dimensional flow field.

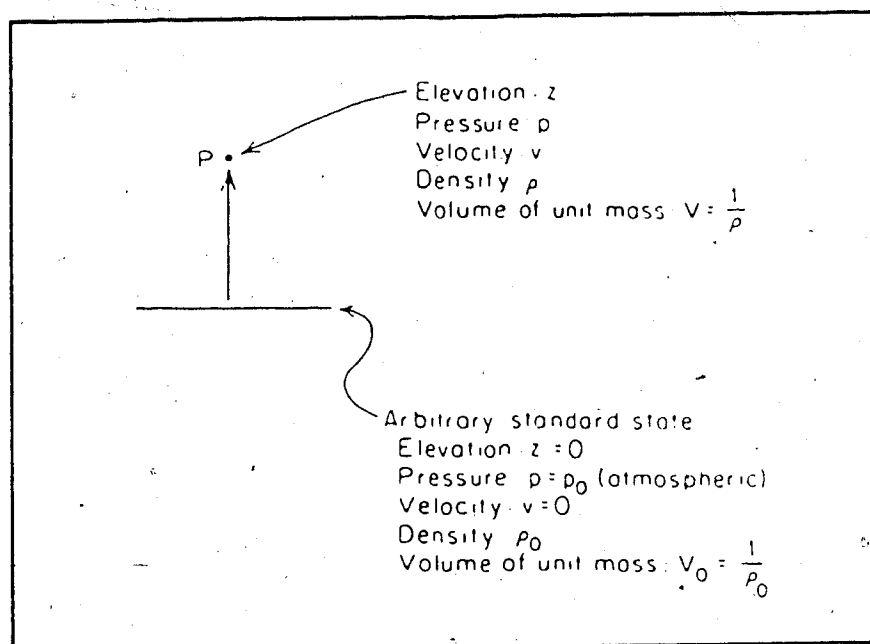


Figure 2.2 Data for calculation of mechanical energy of unit mass of fluid (adapted from Freeze and Cherry 1979).

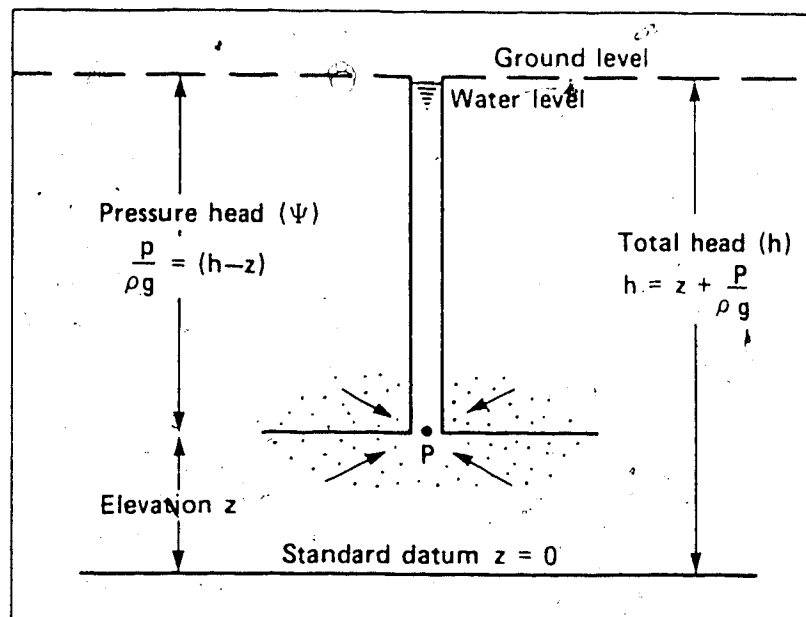


Figure 2.3 Relationship of hydraulic head to pressure head (adapted from Hubbert, 1953).

This figure has been omitted due to copyright restrictions on the material.

Source :


Johnston, 1964, Review of basic formation evaluation: Society of Petroleum Engineers, Paper 965, 29 p. 

Figure Number : 1

Page Number : 3



This figure has been omitted due to copyright restrictions on the material.

Source :

Freeze, R.A., and J.A. Cherry, 1979, Groundwater: Prentice-Hall Inc., Englewood Cliffs,  
N.J., 604 p.

Figure Number : 2.24

Page Number : 63

### 3. THE LENS ASSOCIATED POTENTIAL ANOMALY

A highly permeable rock body of limited areal extent (or lens), enclosed in a less permeable matrix tends to distort the fluid-flow and fluid-potential fields. The principle is based on the physics of groundwater flow, similar cases having been discussed for heat flow through composite media (Carslaw and Jager, 1959) and distortion of the earth's magnetic potential field by rocks of varying magnetic properties (Vacquier et al, 1954). The application of these principles for fluid-flow through an ellipsoid of greater permeability than the surrounding matrix was first considered and solved analytically by Tóth (1962). The phenomenon was later found to occur in the Tertiary Paskapoo Formation during groundwater resource investigations near Olds, Alberta (Tóth, 1966). Freeze (1969a), and Freeze and Witherspoon (1967) conducted numerical mathematical simulations for a variety of hydrogeologic situations, including the effect of permeable lenses, and confirmed Tóth's conclusions.

In the literature, consideration given to the effects of permeable bodies on the fluid potential distribution has, however, been relatively limited in scope. Originally, it was intended that by simulating potentiometric distortions created by varying hydraulic parameters, a working guide would be established for the interpretation of field data. Through this investigation several relationships between the simulated parameters were observed, these are discussed in the following sections. The approach used for the investigation is outlined in Figure 1.1. The analytical (or exact) solution is considered first, and is compared to the numerical (approximate) solution. The numerical method is then used to consider more complex cases that are difficult to treat by analytical mathematics.

### 3.1 ANALYTICAL SOLUTION-Governing Equation

Tóth (1962, p.4384) incorporated the solution derived by Carslaw and Jager (1959, p.427) for heat flow in a medium of permeability ( $k$ ) surrounding an ellipsoid of permeability ( $k'$ ) (Figure 3.1), where the potentials inside ( $\Phi_i$ ) and outside ( $\Phi_o$ ) the ellipsoid are described by:

$$\Phi_i = \frac{x(\partial\Phi/\partial x)}{1+A_o(\epsilon-1)} + \frac{y(\partial\Phi/\partial y)}{1+B_o(\epsilon-1)} + \frac{z(\partial\Phi/\partial z)}{1+C_o(\epsilon-1)} \quad (3.1)$$

and

$$\begin{aligned} \Phi_o = & x(\partial\Phi/\partial x) + y(\partial\Phi/\partial y) + z(\partial\Phi/\partial z) - \frac{(\epsilon-1)A_\lambda x(\partial\Phi/\partial x)}{1+A_o(\epsilon-1)} \\ & - \frac{(\epsilon-1)B_\lambda y(\partial\Phi/\partial y)}{1+B_o(\epsilon-1)} - \frac{(\epsilon-1)C_\lambda z(\partial\Phi/\partial z)}{1+C_o(\epsilon-1)} \end{aligned} \quad (3.2)$$

The uniform potential field ( $\Phi$ ) of Figure 3.1, is distorted by the presence of an ellipsoid of contrasting permeability  $\epsilon = k'/k$ .  $A_\lambda$ ,  $B_\lambda$  and  $C_\lambda$  are integrals describing an oblate spheroid, which upon solution for  $b=c < a$  (where  $a$  is the major axis and  $b$  and  $c$  are the minor axes of the ellipsoid), is expressed by:

$$A_\lambda = \frac{1-e^2}{e^3} \left( \frac{1}{2} \ln \frac{1+e'}{1-e'} - e' \right) \quad (3.3)$$

and

$$B_\lambda = C_\lambda = \frac{1-e^2}{2e^{1/2}} \left( \frac{e'}{1-e'} - \frac{1}{2} \ln \frac{1+e'}{1-e'} \right) \quad (3.4)$$

where

$$e' = \left( \frac{a^2 - b^2}{a^2 - \lambda} \right)^{1/2} \quad (3.5)$$

$A_0$ ,  $B_0$  and  $C_0$  equal  $A_\lambda$ ,  $B_\lambda$  and  $C_\lambda$  for  $\lambda=0$  (at the boundary of the ellipse, where  $\lambda$  is the distance from the endpoint of the ellipse in the downstream or upstream direction),  $e'$  describes the eccentricity of the confocal ellipse through the external points considered and  $e'=e$  when  $\lambda=0$ , which represents the eccentricity of the permeable (generating) ellipse.

### 3.1.1 Solution and Interpretation

Equations 3.1 to 3.5 describe flow through a lens in a three-dimensional flow-field. Tóth's (1962) analytical solution is based on a vertical cross-section through the domain in the  $x$ - $z$  plane, where the hydraulic gradient  $\partial\Phi/\partial x=0.02$  and  $\epsilon=1, 10, 100$ , and  $1000$  for ellipses of varying eccentricity ( $e$ ), (see Equation 3.5).

In Figure 3.1 equipotential distributions are given for  $\epsilon=1$  (homogeneous),  $\epsilon=10$ , and  $\epsilon=1000$  for an ellipse of  $e=.99$  or a length to width ratio of 10:1 ( $a=500$ ,  $b=50$ ). In the homogeneous case ( $\epsilon=1$ ) the potential drop over the distance  $a$ , is 3m(10ft). As  $\epsilon$  is increased to 10, and 1000 the potential drop decreases to 2.6m(8.4ft) and 0.15m(0.5ft) respectively. This results in increased hydraulic gradients and anomalously low potentials at the upstream end of the ellipse and anomalously high potentials at its downstream end. The permeability contrast is the major factor which controls the potential distortion for ellipse's with eccentricities ( $e$ )  $< 0.86$  ( $L:W=2:1$ ), see Figure 3.2. However, for highly eccentric ellipses ( $e$  approaching unity) the distortion is considerably reduced at all  $\epsilon$  values, causing

Undisturbed equipotentials:  $\varepsilon = \frac{k'}{k} = 1$

Equipotential lines when:  $\varepsilon = \frac{k'}{k} = 10$   $\frac{\partial \phi}{\partial x} = 0.02 \text{ L/L}$

Equipotential lines when:  $\varepsilon = \frac{k'}{k} = 1000$

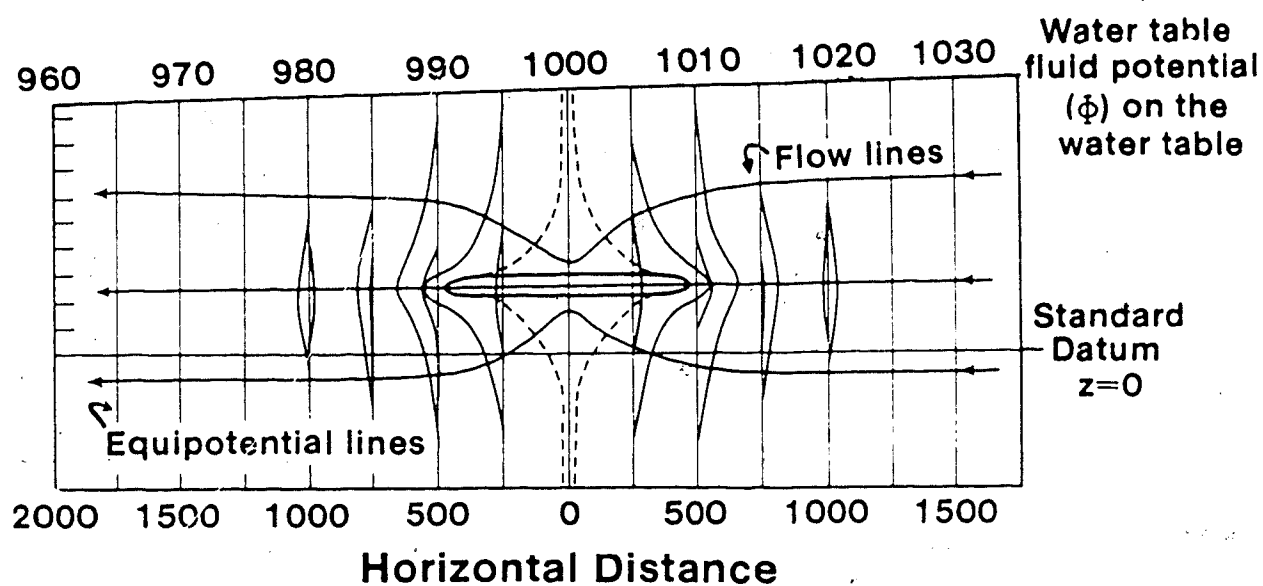


Figure 3.1 Calculated potential distribution around an ellipsoid of permeability  $k'$  placed in an infinite homogeneous medium of permeability  $k$  (adapted from Tóth, 1962).

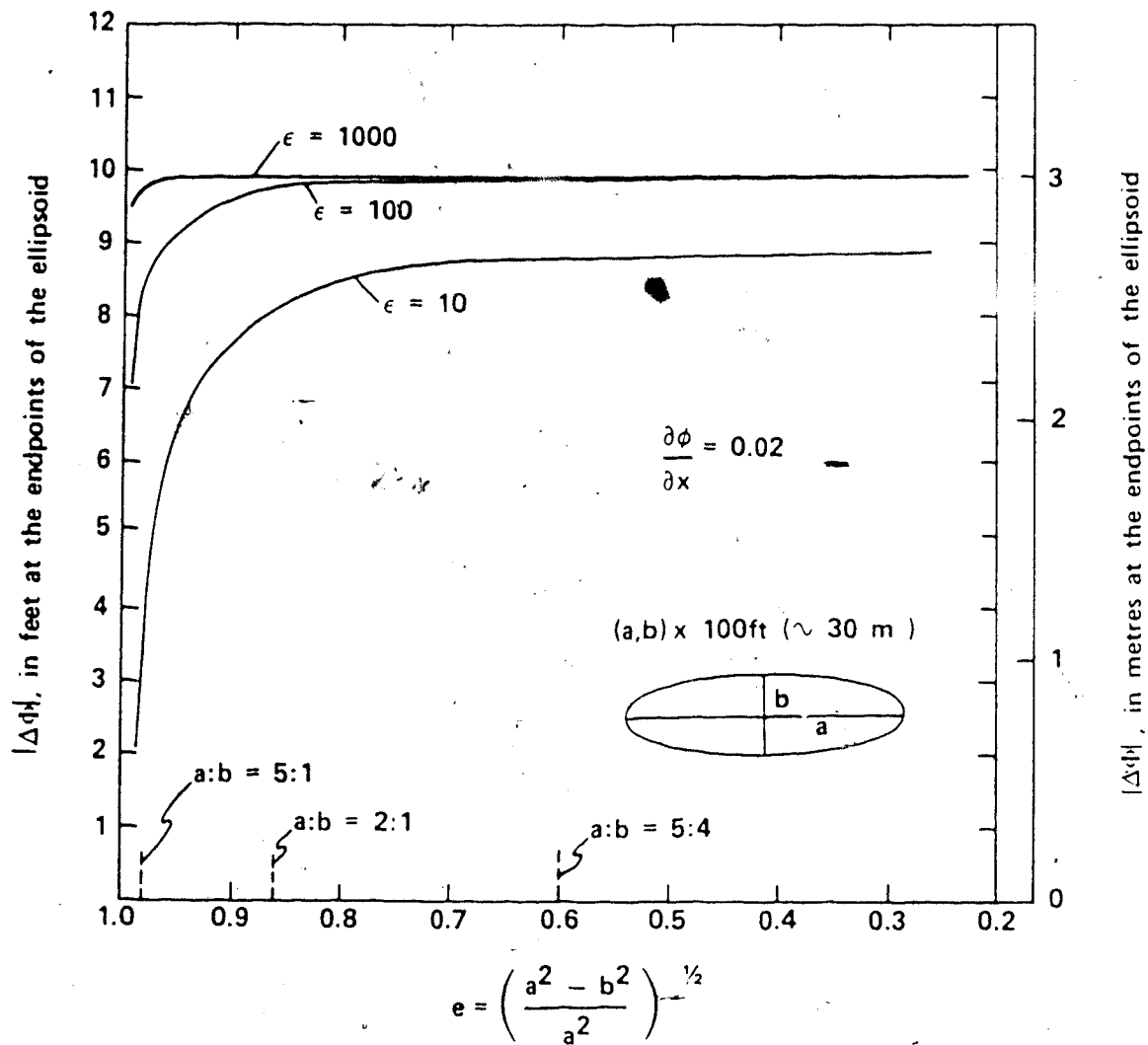


Figure 3.2 Calculated anomalies ( $\Delta\Phi$ ) of an infinite-uniform potential field, at the endpoints of ellipsoidal bodies of varying properties,  $e$  is the eccentricity of the ellipse and  $\epsilon$  is the permeability contrast between the ellipse and its surrounding matrix, (adapted from Tóth, 1962).

the  $\Delta\Phi$  vs.  $e$  curve (Figure 3.2) to become asymptotic to the  $\Delta\Phi$  axis. Furthermore, solutions of equations 3.1 and 3.2 suggest that the magnitude of the distortion is directly related to the hydraulic gradient, eg. the magnitude of the anomaly for  $\epsilon=1000$  and  $e=0.6$  is  $3m(10')$  when  $\partial\Phi/\partial x=0.02$ ,  $1.5m(5')$  for  $\partial\Phi/\partial x=0.01$  and  $0.75m(2.5')$  for  $\partial\Phi/\partial x=0.005$ .

### 3.2 DESCRIPTIVE NOMENCLATURE OF POTENTIAL ANOMALIES

This section is designed to serve as a guide to the nomenclature introduced in the present study and to develop the concept of potential anomalies. It will be shown how a given anomaly may be quantified and normalized for the purpose of comparison with anomalies created by other geologic-hydraulic situations.

#### 3.2.1 Anomaly

The potential anomaly ( $\Delta\Phi$ ) is defined as:

$$\Delta\Phi = \Phi_a - \Phi_o \quad (3.6)$$

where  $\Phi_a$  is the distorted potential at some point in the flow region and  $\Phi_o$  is the corresponding undistorted potential for a homogeneous case (Figure 3.3).

#### 3.2.2 Anomaly Threshold

Tóth's analytical solutions (Figure 3.2) for lenses of varying geometry showed that beyond a certain contrast in permeability between the lens and matrix, here termed  $\epsilon_t$  (the threshold permeability contrast), there is effectively no drop in potential between the upstream and downstream extremities of the lens. An increase in the permeability contrast beyond  $\epsilon_t$ , does not increase the magnitude of the anomaly, the anomaly having effectively reached an upper limit (threshold), given by :

$$\Delta\Phi_{\epsilon_t} = \frac{L(x,y,z)}{2} \cdot \frac{\partial\Phi}{\partial(x,y,z)} = a \cdot \frac{\partial\Phi}{\partial(x,y,z)} \quad (3.7)$$

The threshold anomaly ( $\Delta\Phi_{\epsilon_t}$ ), illustrated in Figure 3.3, is determined by calculating the undistorted potential gradient component  $\partial\Phi/\partial(x,y,z)$  occurring across the length  $L(x,y,z)$ , or  $a$ , of the permeable body and solving Equation 3.7.

### 3.2.3 Relative Anomaly

To facilitate the comparison of permeable bodies with differing geometric configurations and hydraulic parameters, a normalized anomaly scale is required. In this way the effect of differing geometries of permeable bodies and their ability to distort fluid-flow and fluid-potential fields may be compared. The relative anomaly ( $\Delta\Phi_r$ ) is defined as:

$$\Delta\Phi_r = \frac{\Delta\Phi_{\chi=0}}{\Delta\Phi_{\epsilon_t}} \quad (3.8)$$

where  $\Delta\Phi_{\chi=0}$  is always calculated at the upstream or downstream extremity of the permeable body (Figure 3.3).  $\Delta\Phi_r$  equals unity when  $\Delta\Phi_{\chi=0}$  is equal to  $\Delta\Phi_{\epsilon_t}$ , i.e. when the threshold anomaly occurs. The value of  $\Delta\Phi_r$  is independent of areal scale, as well as direction or magnitude of the hydraulic gradient.

### 3.2.4 Glossary Of Variables

A listing of the variables used in this study are given in Appendix 3A.

## 3.3 NUMERICAL SOLUTION-The Finite Difference Method

Since the advent of digital computers, various techniques have been developed to solve partial differential equations, which have since been applied to the groundwater flow equations. Basic solution and application techniques of the Finite-Difference Method and the Finite-Element Method may be found in Wang and Anderson, 1982, and the Boundary-Integral Method in Liggett and Liu, 1983. The numerical simulations conducted in



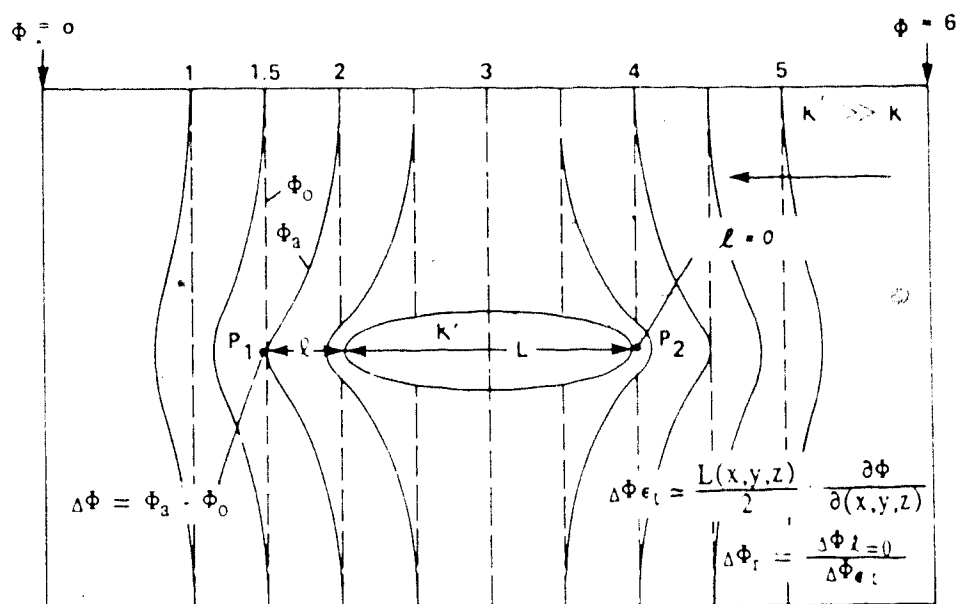


Figure 3.3 Illustration of the concepts of anomaly ( $\Delta\Phi$ ), threshold anomaly ( $\Delta\Phi_{\epsilon_t}$ ) and relative anomaly ( $\Delta\Phi_r$ ).  $\Phi_a$  is the distorted hydraulic head at  $P_1$  and  $\Phi_0$  is the original undistorted head.  $L$  is the length of the lens parallel to flow and  $l$  is the distance from the endpoint of the lens to  $P_1$  at which  $\Delta\Phi$  is calculated.  $\Delta\Phi_r$  is calculated at ( $l=0$ ) eg. at  $P_1$  and is equal to unity at a permeability contrast between lens and matrix of greater than  $\epsilon_t$ .

this study use a finite-difference code developed by the United States Geological Survey (McDonald and Harbough, 1983) called "A Modular Three-Dimensional Finite-Difference Groundwater Flow Model" (GWFM). The reader is referred to the Users Manual referenced above for details on code implementation.

The basic premise of the finite-difference method is to replace the continuous system described by Equation 2.18 by a finite set of discrete points in space and time, where the partial derivatives are replaced by differences between functional values at these points. The process yields a system of simultaneous linear algebraic functions whose solution gives values for the hydraulic head at specific points and time. These values are an approximation of the hydraulic head distribution that would be obtained by an analytical solution of the partial differential equation of flow.

A simplifying step taken during the numerical simulations as well as during the analytical, is the implementation of the steady-state condition, which removes the time varying aspects of the hydraulic head distribution. Under steady-state conditions, the mass of fluid entering the system is equal to that leaving the system eg. there is no storage or release of fluid by the system. This will cause the calculated head distortion around a permeable lens to be symmetrically distributed about its upstream and downstream ends.

### 3.3.1 Implementation Of The USGS Groundwater Flow Model

The following is a brief account of the operation of the model, with sample input and output files that have been appended to the text. The flow chart in Figure 3.4 shows the code modules used in the simulations and the method of processing.

The Basic Package handles tasks which are part of the model as a whole. Among these tasks are : specification of boundaries, determination of time step lengths (for transient simulations) and establishment of initial conditions. The printing of results is handled by the Output Control Package which is attached to the Basic Package. A listing of Basic Package Input is given in Appendix 3B.1 for the model shown in Figure 3.5. The Block Centered Flow Package calculates terms of the finite-difference equations representing flow within the

porous medium; specifically, flow from cell to cell and flow into storage (for transient simulations). Grid dimensions, type of simulation (steady-state, transient, confined or unconfined) and transmissivity distribution are specified in this package (see Appendix 3B.2 for a listing of the input record). The Stress Package which can be used for specifying recharge or discharge (and their mode of occurrence) in the flow system, is not used in this study.

The Solver Package is called by the main program when the input data have been processed and the finite-difference equations formulated. The user has the option of using one of two solution techniques, a) the Strongly Implicit Procedure (SIP) or b) the Slice-Successive Overrelaxation (SSOR) method, both of which use an iterative solution technique. Since the obtained solution is only an approximation, the Solver Package input must define the tolerance level or accuracy to which the solution is required to converge. In most cases this level was set at :

$$\text{Tolerance} = | \text{HNEW} - \text{HOLD} | = 0.01 \quad 3.9$$

HOLD represents the head distribution at the beginning of an iteration and HNEW represents the head distribution at the end of an iteration at any given node point.

A sample lens problem is illustrated in Figure 3.5 indicating the manner in which a given domain is discretized to obtain the appropriate input data.

### 3.3.2 Output Processing

The University of Alberta's "ice 2" program was used to plot the results obtained from the numerical simulations:

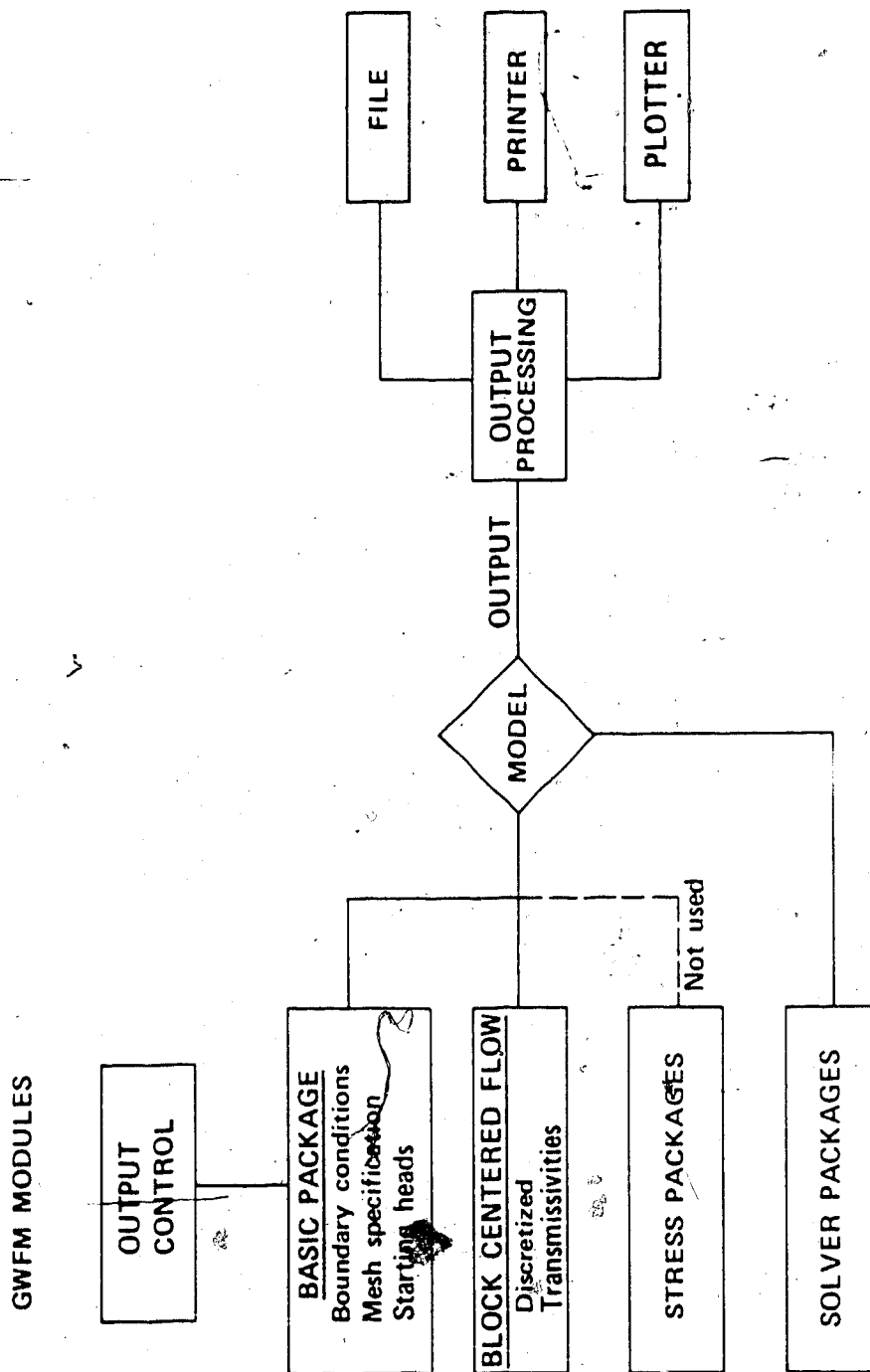


Figure 3.4 Flow chart outlining the procedure for using the USGS Groundwater Flow Model.

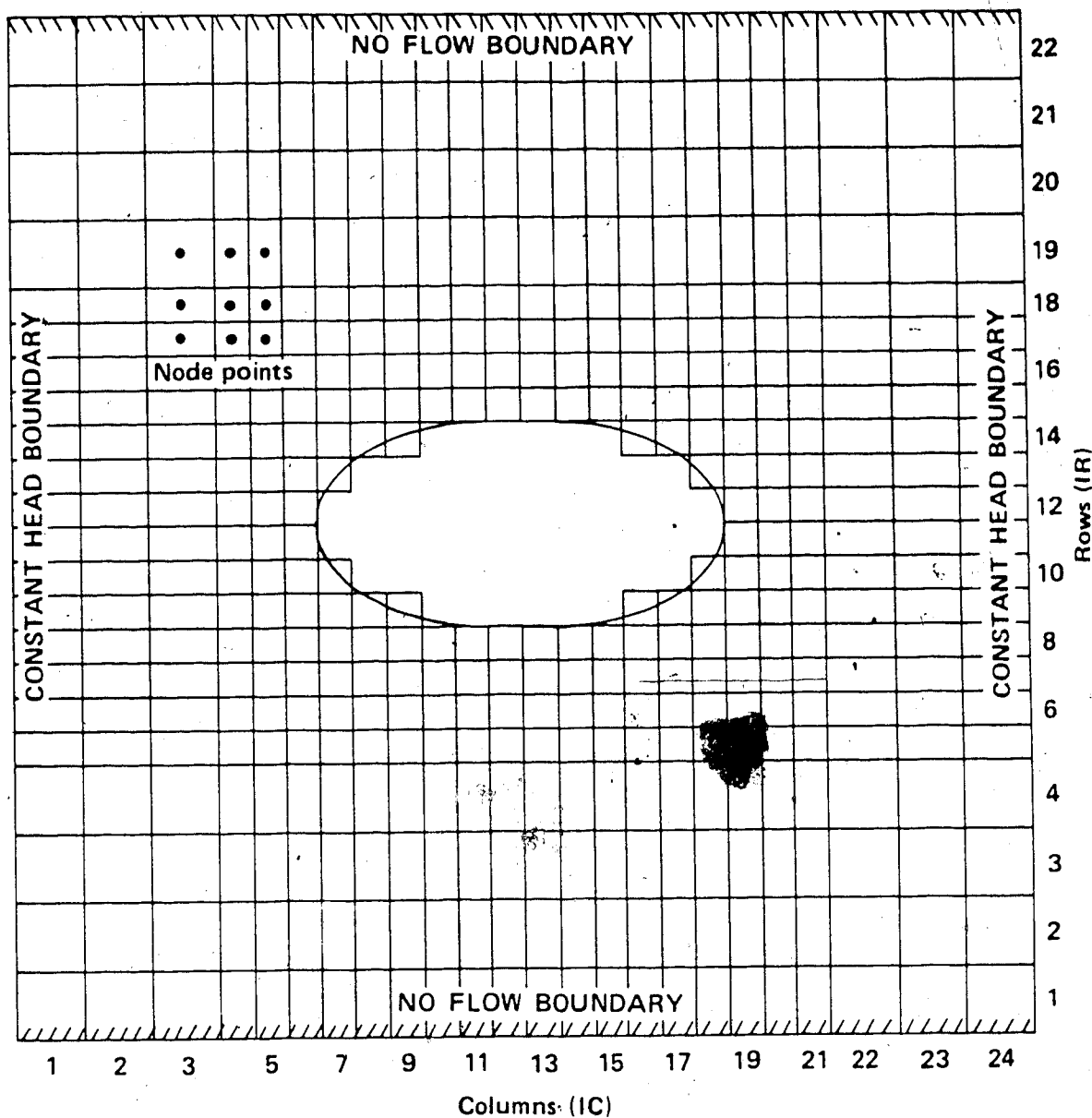


Figure 3.5 Discretized model an ellipsoid used for the numerical simulation of flow. Flow occurs normal to constant head boundaries and parallel to no flow boundaries. Node points are the locations at which solutions for hydraulic head are obtained. The mesh dimension is 24 columns by 22 rows.

### 3.4 COMPARISON OF NUMERICAL AND ANALYTICAL SOLUTIONS

When conducting numerical simulations, various simplifying assumptions are made to reduce the problem size and hence the calculation time. The assumptions used in this study are:

1. Distortion of the fluid-potential field is negligible at distances greater than the length parallel to flow, of the distorting body. Reflection from constant head boundaries should therefore be insignificant.
2. The permeable ellipse (described mathematically) used in the analytical solution may be sufficiently approximated by the finite-difference mesh.

A typical finite-difference mesh used for the numerical simulations is given in Figure 3.5. The mesh size was adjusted (enlarged) to maintain a minimum distance of 1.5 L between the lens extremities and constant head boundaries. Figure 3.6 illustrates the discretization of the various ellipses modelled using the finite-difference grid.

The analytical solution produced a family of curves which relate the degree of isopotential distortion ( $\Delta\Phi_r$ ), the permeability contrast ( $\epsilon$ ) and the eccentricity of an ellipse ( $e = L:W$ ). The families of curves produced by the numerical and analytical solution methods is given in Figures 3.7 and 3.8 respectively. The results are also tabulated in Table 3.1.

For ellipses of  $L:W=5:4$  (almost circular) the numerical and analytical solutions are in close agreement (Table 3.1). However, as the  $L:W$  ratio is increased beyond 2:1 a systematic departure between the analytically and numerically calculated solutions occurs. The analytical method represents an exact solution of the problem whereas the numerical method represents an approximation of the exact solution. One possible explanation of the departure that was investigated is the representation of highly eccentric ellipses with rectangles, Figure 3.6 (i.e., an ellipse of  $a:b=5:1$  was discretized by a 10:2 node rectangle), which does not adequately define the converging ends of the ellipse. Increasing the number of nodes in the finite-difference grid (thereby producing a finer mesh) to 45 by 35 nodes (the original grid had 28 by 22 nodes), and discretizing an ellipse of  $a:b=5:1$  by a 15:3 node array, allows a better representation of the ellipse's converging boundary. When flow is simulated using the

above grid at a permeability contrast of  $\epsilon = 10$ , the numerical (NM) solution converges from an original value  $NM_{\Delta\Phi_r} = 0.59$  to a new  $NM_{\Delta\Phi_r} = 0.50$ . As the grid is further extended to 65 by 35 nodes, and the ellipse is discretized with a 25 by 5 node array,  $NM_{\Delta\Phi_r}$  attains a value of 0.45. A 105 by 35 node grid and 35 by 7 node ellipse produced an  $NM_{\Delta\Phi_r}$  value of 0.43. By increasing the mesh size it appears that the numerical solution for an eccentric ellipse may converge with the analytical solution for that ellipse of  $AN_{\Delta\Phi_r} = 0.33$ . However, a decrease in the convergence rate with the last and largest mesh used, suggests a very large grid would be required to obtain satisfactory results.

The analyses conducted above suggests that it is not possible to describe flow through an ellipse adequately by using a rectangle to represent that ellipse. Examination of the analytical solution for flow through a rectangle indicates that the integrals describing the boundaries of an ellipse are of considerably different form than those describing a rectangle (pers. comm. G.D. Swaters, Dept. of Mathematics, U. of Alberta). The parallel boundaries of a rectangle allow flow lines to enter and leave only at its upstream and downstream ends. An ellipse, on the other hand, has flow lines diverging from it at the point where its boundaries begin to converge, hence it is a less efficient conductor than the rectangle. The analytical solution of flow through a rectangle however, is considerably more complex than through an ellipse and requires the construction of a complex computer code for its solution. In essence, the analytical and numerical solutions are only comparable for non-eccentric ellipses that are relatively easy to represent by numerical methods. This fact however, does not reduce the utility of the numerical method for further modelling; provided one realizes that the solutions are case specific and generalizations must be made with caution.

### 3.5 NUMERICAL SIMULATIONS

The patterns of lithologic variation and the resulting hydraulic heterogeneities associated with lenticular strata are usually complex. Important limiting cases of lens associated fluid potential distortions can be investigated by observing the effects of varying lens geometries, anisotropic media and multiple lens configurations. It is hoped that these

Table 3.1 Comparison of relative anomalies calculated analytically ( $AN_{\Delta\Phi_r}$ ) and numerically ( $NM_{\Delta\Phi_r}$ ) for ellipses approximated by rectangles.

$\epsilon$	L:W = 5:4		L:W = 2:1		L:W = 5:1		L:W = 10:1	
	$AN_{\Delta\Phi_r}$	$NM_{\Delta\Phi_r}$	$AN_{\Delta\Phi_r}$	$NM_{\Delta\Phi_r}$	$AN_{\Delta\Phi_r}$	$NM_{\Delta\Phi_r}$	$AN_{\Delta\Phi_r}$	$NM_{\Delta\Phi_r}$
3	.66	.58	.49	.38	.10	.24	0.04	.16
10	.89	.87	.81	.79	.33	.59	.16	.45
100	.99	.98	.98	.97	.85	.94	.66	.90
1000	1.0	0.99	.99	.99	.98	.99	.95	.98



investigations will provide a useful framework to guide the interpretation of field data.

### 3.5.1 Effects Of Varying Permeability Contrast And Geometry On The Anomaly

The variation of the relative anomaly ( $\Delta\Phi_r$ ), due to a changing permeability contrast is an exponential relationship defined by the family of curves given in Figure 3.7, tabulated values for which are given in Table 3.2. A lens with  $L:W$  approaching unity is able to distort the fluid potential field to a greater extent than a lens with  $L:W$  approaching  $(\infty)$ . This is clearly shown, in that a value of  $\Delta\Phi_r = 0.5$  is attained by an  $\epsilon$  value of 3.4 for a lens of  $L:W = 5:4$ , but requires an  $\epsilon$  value of 18 for a lens of  $L:W = 15:1$  (Table 3.3). In this respect, the geometry being proportional to the area of the permeable body, is also exponentially related to the relative anomaly developed. Contoured potentiometric surface and anomaly ( $\Delta\Phi$ ) maps for lenses of length to width ratios of 2:1 and 5:1 at  $\epsilon$  values of 100 are given in Figure 3.9. Appendix 3C contains similar maps for  $L:W = 1:1$  and 10:1.

Inspection of Table 3.3 suggests that even the least favourable geometry of lens ( $L:W = 15:1$ ) can cause large potentiometric distortions at relatively low contrasts in permeability (1-2 orders of magnitude) with its surroundings. A typical sandstone petroleum reservoir will have a permeability of 100md or greater, whereas the surrounding argillaceous rocks may have permeabilities of 0.1md to 1.0 $\mu$ d, (Brace, 1980). In principle, therefore, the development of potentiometric anomalies due to the presence of relatively permeable rock bodies should be a common occurrence in the field.

### 3.5.2 Areal Extent Of Anomalies

The previous section showed that variation of a lenses geometry and permeability contrast to its surrounding matrix systematically affected the relative anomaly produced. A natural extension to this line of investigation is to determine the areal extent of anomalies (i.e. how far away from the endpoints of the lens does the anomaly persist). These results are expressed as the attenuation of the anomaly from the downstream or upstream extremities of the lens.

Table 3.2 Calculated relative anomalies ( $\Delta\phi_r$ ) for lenses of varying L:W, hydraulic conductivity contrast  $\epsilon$ , and potential gradients.

$\Delta\phi_r$ CALCULATED NUMERICALLY FOR RECTANGULAR LENSES									
$\epsilon$	L:W = 5:4		L:W = 2:1		L:W = 5:1		L:W = 10:1		L:W = 15:1
	$\frac{\partial\phi}{\partial x}=0.01$	$\frac{\partial\phi}{\partial x}=0.02$	$\frac{\partial\phi}{\partial x}=0.01$	$\frac{\partial\phi}{\partial x}=0.02$	$\frac{\partial\phi}{\partial x}=0.01$	$\frac{\partial\phi}{\partial x}=0.02$	$\frac{\partial\phi}{\partial x}=0.01$	$\frac{\partial\phi}{\partial x}=0.02$	$\frac{\partial\phi}{\partial x}=0.02$
3	-	.58	-	.38	-	.24	-	.16	.10
5	-	-	.64	.63	.38	.39	.26	.28	-
10	.86	.87	.81	.79	.59	.59	.44	.46	.36
30	-	.95	-	.90	-	.82	-	.73	-
100	.97	.98	.98	.97	.94	.94	.90	.90	.86
1000	.99	.99	.99	.99	.99	.99	.98	.98	.97

Table 3.3 Approximate conductivity contrast ( $\epsilon$ ) required for a rectangular lens of varying L:W to attain  $\Delta\phi_r$  levels of 0.25, 0.5, 0.75 and 0.9.

$\Delta\phi_r$	$\epsilon$ @ L:W RATIOS OF:				
	5:4	2:1	5:1	10:1	15:1
.25	0.8	1.2	3.0	4	7.1
.5	3.4	4.2	7.5	12	18
.75	5	10	20	35	50
.9	13	30	60	100	160

Figure 3.10 shows the attenuation of  $\Delta\Phi$  parallel to flow of for hydraulic gradients of  $\partial\Phi/\partial x = 0.01$  and  $0.02$ , as well as the attenuation normal to flow (for  $\partial\Phi/\partial x = 0.02$ ), through a lens of  $L:W = 1:1$ . The attenuation is the fraction of the anomaly  $\Delta\Phi$  remaining at some distance  $\ell/L$  relative to  $\Delta\Phi$  at  $\ell/L = 0$ , where  $L$  is the total length of the lens parallel to flow and  $\ell$  is the map distance to the point of measurement of  $\Delta\Phi$ , (see Figures 3.3 for illustration). A significant effect of lens associated anomalies is that the anomaly ( $\Delta\Phi$ ) attains a maximum magnitude at an approximate distance of  $\ell/L = 0.1-0.15$  for bodies of  $L:W = 1:1$ , and that both the magnitude and distance are reduced with elongation of the body (Figure 3.10).

The areal extent of anomalies appears to be sensitive to lens geometry (relative area) and flow direction (i.e., attenuation is faster normal to flow than parallel to flow) (Figure 3.10). An anomaly created by a square body is more than three times greater in areal extent than that created by a long rod like lens eg. the anomaly attenuates to 50% at a distance of  $\ell/L = 0.8$  for a square body versus  $\ell/L = 0.24$  for a highly elongate body ( $L:W = 10:1$ ).

### 3.5.3 Effect of Varying Flow Directions On Anomalies

The numerical simulations in the previous sections maintained the potential gradient parallel to the long axis of the permeable body. However, if the potential gradient is at an oblique angle to the long axis orientation, a reduction of the anomaly occurs. The condition is due to a reduction in  $L$  (length parallel to flow) as the lens is rotated through  $90^\circ$  (Figure 3.11). A series of simulations for  $L:W = 2:1$  and  $5:1$  at  $45^\circ$  and  $90^\circ$  are used to illustrate the effect of rotation, for which contoured potentiometric and anomaly maps are presented in Appendix 3C.

Flow occurring obliquely to the long axis of a permeable body (which would probably represent the most realistic field cases, since parallel and normal flow directions are special conditions) causes an apparent offset or asymmetry of the equipotential distribution; reaching a maximum when flow is at  $45^\circ$  to the long axis.

### 3.5.4 Effect Of Vertical Anisotropy

To determine the effect of vertical anisotropy on the areal extent and magnitude of lens associated anomalies, a series of simulations were conducted for a lens of  $L:W = 2:1$ , a value of 100 and potential gradient of 0.02 using vertical anisotropy factors of 2, 5 and 10 ( $k_h > K_v$ ). The results are presented as contoured potentiometric surfaces and corresponding anomaly maps in Figure 3.12 and 3.13.

Vertical anisotropy, of the type which may be expected to occur in a layered sequence of sedimentary rocks does not effect the anomaly magnitude, as shown by the constant magnitudes ( $\Delta\Phi$ ) occurring in the isotropic and highly anisotropic cases (Figure 3.12b versus 3.13d). Vertical anisotropy does, however, affect the shapes of the distortions and their areal extents. In Figure 3.12a,b (isotropic case,  $k_h = K_v$ ) the equipotentials are oriented symmetrically about the lens with the anomaly contours assuming an elliptical shape, the major axes of which are normal to flow. As the vertical anisotropy is increased, a systematic elongation of the equipotentials and the anomaly contours occurs parallel to flow. The effect suggests that potentiometric anomalies in normally (layered, argillaceous) anisotropic sedimentary rocks would tend to be bounded stratigraphically, and therefore, have limited vertical extent. However, further work is required with 3-D simulators to substantiate this hypothesis and determine its limitations.

### 3.5.5 Multiple Lens Configurations

Most lenticular geologic strata will not contain just one isolated lens, but rather be composed of diverse arrays of lenses whose specific positions and sizes will be dependent on depositional process. The combination of lenses, their sizes, relative permeabilities and positions are infinite. However, simulations of relatively simple cases may be of aid in the interpretation of the more complex field situations.

As an example, a lens of  $L:W = 10:1$  ( $k' \gg k$ ), within a uniform potential field has negative and positive anomalies of equal magnitude symmetrically disposed about its upstream and downstream ends. If this lens is split into two individual bodies, each of  $L:W = 5:1$ ,

continuity of flow would be broken; causing the positive anomaly of the upstream body to be juxtaposed onto the negative anomaly of its downstream counterpart (Figure 3.14a,b). The resulting interference causes an increase of the potential gradient and a decrease in the anomaly between the two bodies (the interfered location) with a corresponding increase (shift) of the anomaly at their exterior upstream and downstream (uninterfered) locations. The degree of interference is expressed by the 'anomaly shift,' defined as  $\Delta\Phi_i$ .

$$\Delta\Phi_i = \frac{\Delta\Phi}{(|\Delta\Phi| + |\Delta\Phi_i|) \cdot 0.5} \cdot 100\% \quad 3.9$$

where,  $\Delta\Phi$  and  $\Delta\Phi_i$  equal the anomaly at the upstream and downstream ends of the lens respectively. As the separation between the bodies is increased to a large distance, the interference effect is reduced to the point where they behave as individual entities. The attenuation of the anomaly shift as the lens separation is increased parallel to flow is given in Figure 3.15a, and in Figure 3.15b for separation normal to flow.

For cases where adjacent lenses are not of the same length (L) the interference pattern developed tends to be asymmetrical. To investigate this effect, further simulations were conducted for two adjacent lenses of  $L:W=3:1$  and  $5:1$  at a separation of,

$$\frac{2}{(L_a + L_b)} = 1/4$$

The resulting interference pattern is shown in Figures 3.14c, and 3.14d. An anomaly shift of 45% occurred in the smaller downstream lens  $L_a$  whereas the larger upstream lens  $L_b$  only underwent an anomaly shift of 14%. The asymmetry is due to the difference in the uninterfered anomaly magnitudes created by each lens (ie.  $\Delta\Phi_b > \Delta\Phi_a$ ). These impart an anomaly shift to the adjacent lens corresponding to their individual anomaly magnitudes.

A series of simulations were conducted by varying the overlap and vertical separation between lenses, the corresponding potentiometric surface maps and anomaly maps for some of these are given in Appendix 3C. The simulations indicate that the anomaly shift due to the

interference effect is reduced in proportion to the amount of overlap. These simulations also serve as a practical guide for the interpretation of field data.

### 3.6 THE LENS AS A FOCAL AND TRAPPING MECHANISM FOR HYDROCARBONS

Due to the convergence of flow paths at the upstream end of a highly permeable lenticular body (Figure 3.1) an effective focal mechanism for fluid-flow is created by the lens. The cross-sectional area through which a given volume of fluid mixture moves is greater outside than inside the lens, and is a direct result of the focusing effect.

The specific mechanism(s) responsible for the movement of hydrocarbons from the poorly permeable source rock (primary migration) to the relatively permeable reservoir rock (where secondary migration occurs) is a widely debated issue (Roberts and Cordell, 1980). The only clear thing about primary migration is that it must occur (as evidenced by the abundance of petroleum reservoirs). A recent review of the mechanism(s) that may control primary migration is given in North, 1985. Discussion of the primary migration processes is beyond the scope of this study, and it must suffice to say that the majority of the hypothesis forwarded to date favour transport of hydrocarbons within formation water as molecular, micellar or gas charged solutions. Migration along micro-fractures or kerogen networks in the source rock have also been suggested.

According to the Hydraulic Theory of Petroleum Migration (Tóth 1980) the principal agent responsible for the transport and accumulation of hydrocarbons is gravity-induced cross-formational flow. However, gravity induced fluid-flow patterns may be modified by the presence of force fields due to deformation of the rock framework. If the moving formation water is hydrocarbon bearing, when it impinges upon the matrix (poor permeability) - reservoir (good permeability) boundary, the impelling force and capillary pressure acting upon an elemental volume of hydrocarbon in a water wet environment, favour its entrance into the coarse grained, permeable reservoir (Figure 3.16), Hubbert, 1953, Tóth, 1970, North, 1985. The fact that hydrocarbons can be recovered from a reservoir, means that they can move within it, therefore secondary migration must occur. The exact mechanism of secondary

migration, whether as a separate phase, in solution or as minute globules is not of little concern. However, there are several mechanisms favouring the retention of hydrocarbons within the reservoir and transmission of water through it. Exsolution of gaseous hydrocarbons may be promoted by a decrease in formation pressure or an increase in their partial saturation pressure. Simple mechanical filtration of larger hydrocarbons (oil) will occur at the sand/shale interface, favouring their retention. Most importantly, capillary pressures oppose the transmission of hydrocarbons through the sand/shale interface, and the impelling force acting on a mass of water will be greater than that acting on a mass of oil, thereby favouring the retention of oil and transmission of water (Figure 3.16). Structural dip of the upper confining layer and divergence of the impelling forces acting on the different fluid phases will control the location and contact relationship between the hydrocarbon accumulation and the water saturated portion of the reservoir. In summary, the discontinuous lenticular reservoir is a natural hydrocarbon trap.

The concept of the hydrocarbon 'trap' has changed during the history of petroleum exploration and production. The notion of a static impermeable seal is giving way to more enlightened and sophisticated models. Roberts (1980, p.218) states some of the functional characteristics of a trap:

1. *"A trap is a paradox, because it must leak to function as a trap."*
2. *A trap is a forced-draft, flow-through system.*
3. *A trap is a center of deep water discharge.*
4. *A trap is an active-focal mechanism, not a passive sealed dead end container.*
5. *A trap is a hydrocarbon separator, in a sense a filter ...."*

The permeable lens is well suited to create hydrocarbon accumulations in petroliferous basins. Recognizable signatures, distinguishable from potentiometric anomaly noise from other sources are one of its many physical manifestations. The application of the lens associated potential anomaly theory in the search for reservoir quality rock bodies should be viewed as a geophysical method based upon the physical laws which govern groundwater flow.



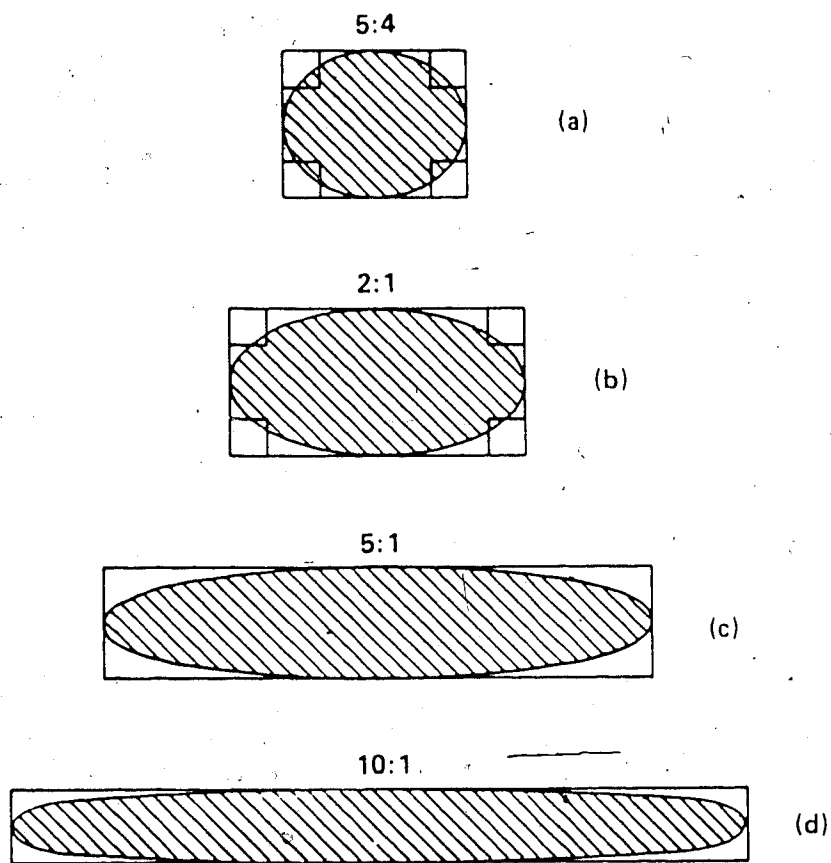


Figure 3.6 Ellipses of varying eccentricity solved for analytically and their substitute geometry for numerical simulation.

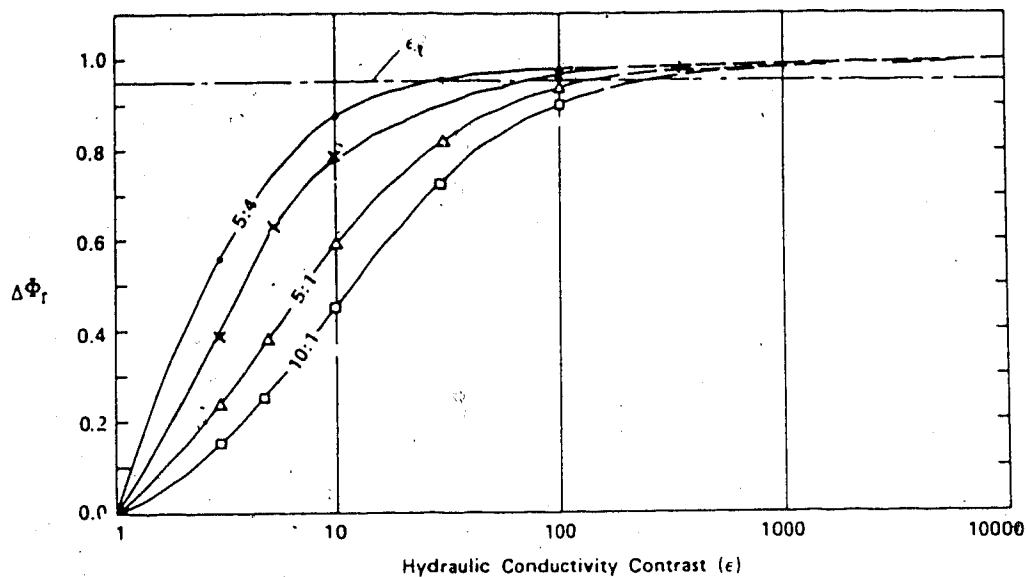


Figure 3.7 Family of curves indicating the relative anomaly  $\Delta\Phi_r$  produced by ellipsoidal bodies (discretized by a rectangular mesh) of varying properties - NUMERICAL SOLUTION. The permeability contrast required to obtain  $\Delta\Phi_r = 0.95$  ( $\Delta\Phi_r = \Delta\Phi/\Delta\Phi_{\epsilon_t}$ ) is  $\epsilon_t$ .

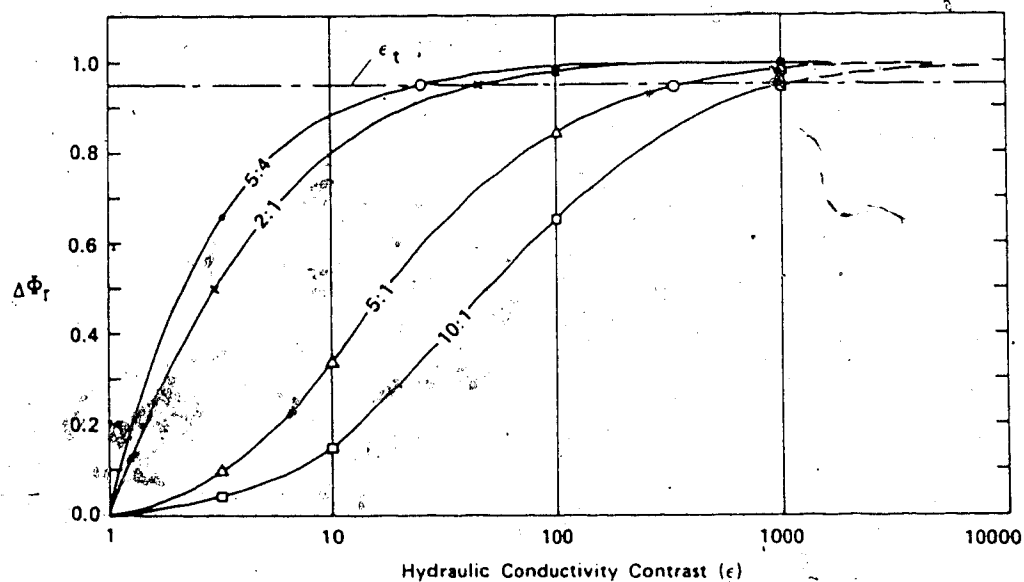


Figure 3.8 Family of curves indicating the relative anomaly  $\Delta\Phi_r$  produced by ellipsoidal bodies of varying properties - ANALYTICAL SOLUTION.

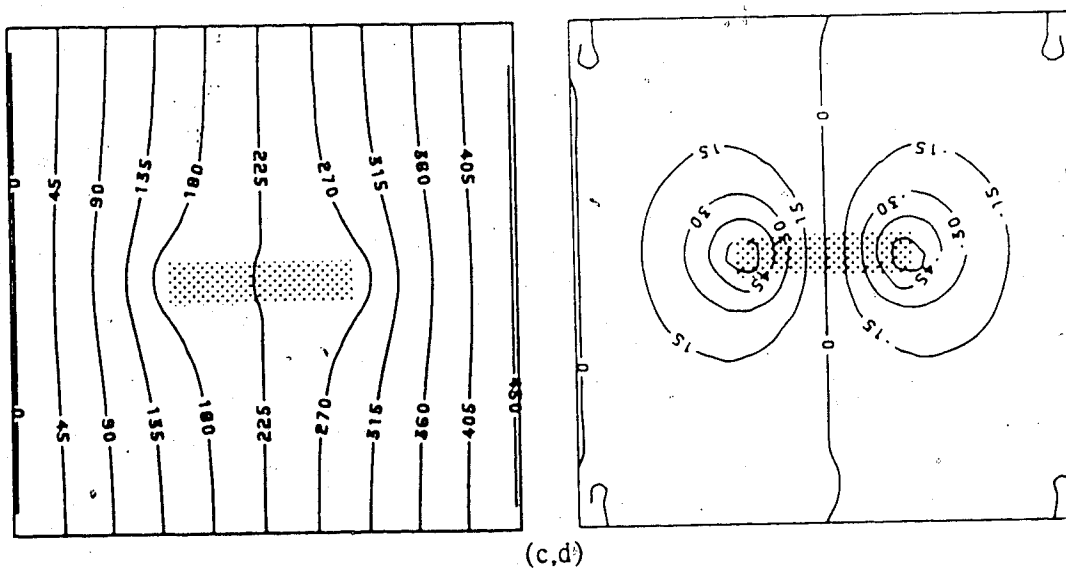
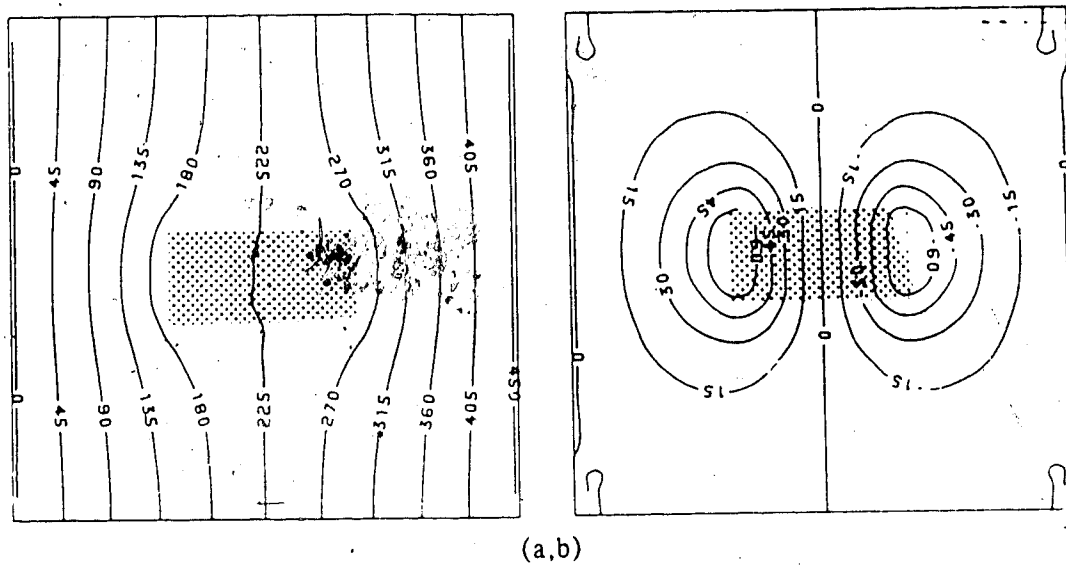


Figure 3.9 Potentiometric surface and anomaly maps for lens of  $L:W = 2:1$  (a,b) and  $L:W = 5:1$  (c,d),  $\epsilon = 100$ ,  $\frac{\partial \phi}{\partial x} = 0.02$ , flow is from right to left.

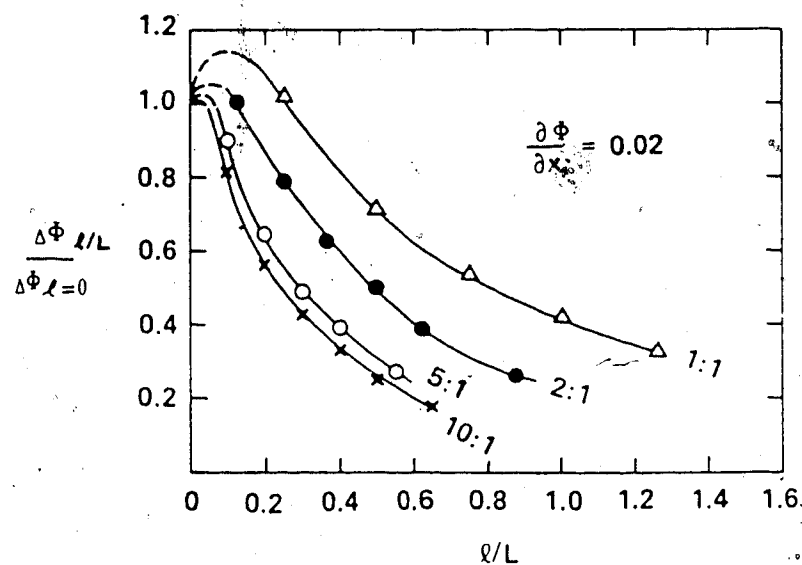
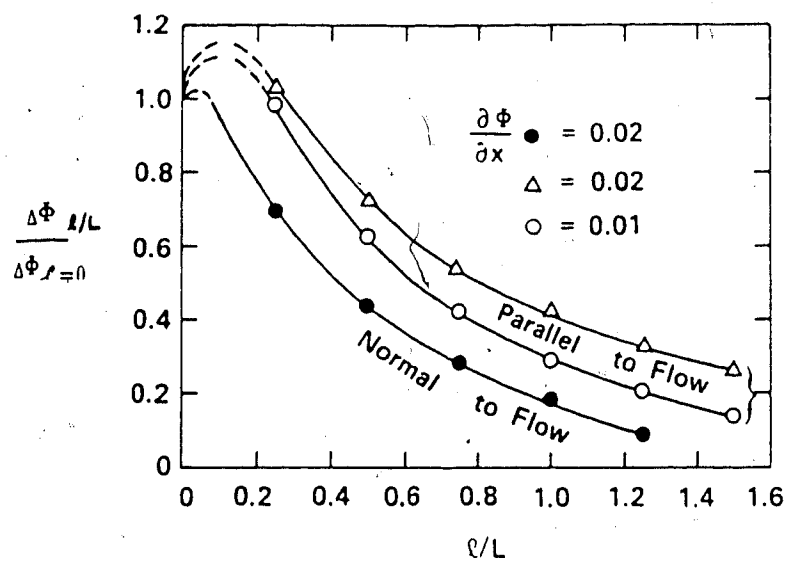


Figure 3.10 Anomaly attenuation parallel to flow and normal to flow measured from the extremities of a body  $L:W = 1:1$ , (a). Anomaly attenuation parallel to flow for varying  $L:W$  ratios. Note that the anomaly attains a maximum magnitude at a distance of  $\ell/L = 0.05-0.1$  from the end of the lens.  $L$  is the length of the lens and  $\ell$  is the distance from the end of the lens at which the attenuation is calculated.

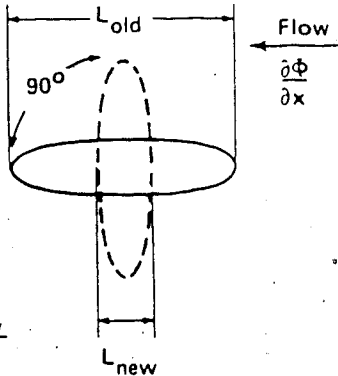


Diagram illustrating the change in potential difference  $\Delta\Phi$  due to the rotation of a lens with respect to the flow direction. The flow direction is indicated by an arrow labeled "Flow" and the velocity gradient is labeled  $\frac{\partial\Phi}{\partial x}$ . The lens is shown at a  $90^\circ$  angle to the flow direction. The length of the lens is labeled  $L_{old}$  and  $L_{new}$ .

$$\Delta\Phi_{old} = \frac{\partial\Phi}{\partial x} \frac{L_{old}}{2}$$

$$\Delta\Phi_{new} = \frac{\partial\Phi}{\partial x} \frac{L_{new}}{2}$$

$$\Delta\Phi_{old} > \Delta\Phi_{new}$$

Figure 3.11 Changes in  $\Delta\Phi$  due to rotation of lens with respect to flow direction.

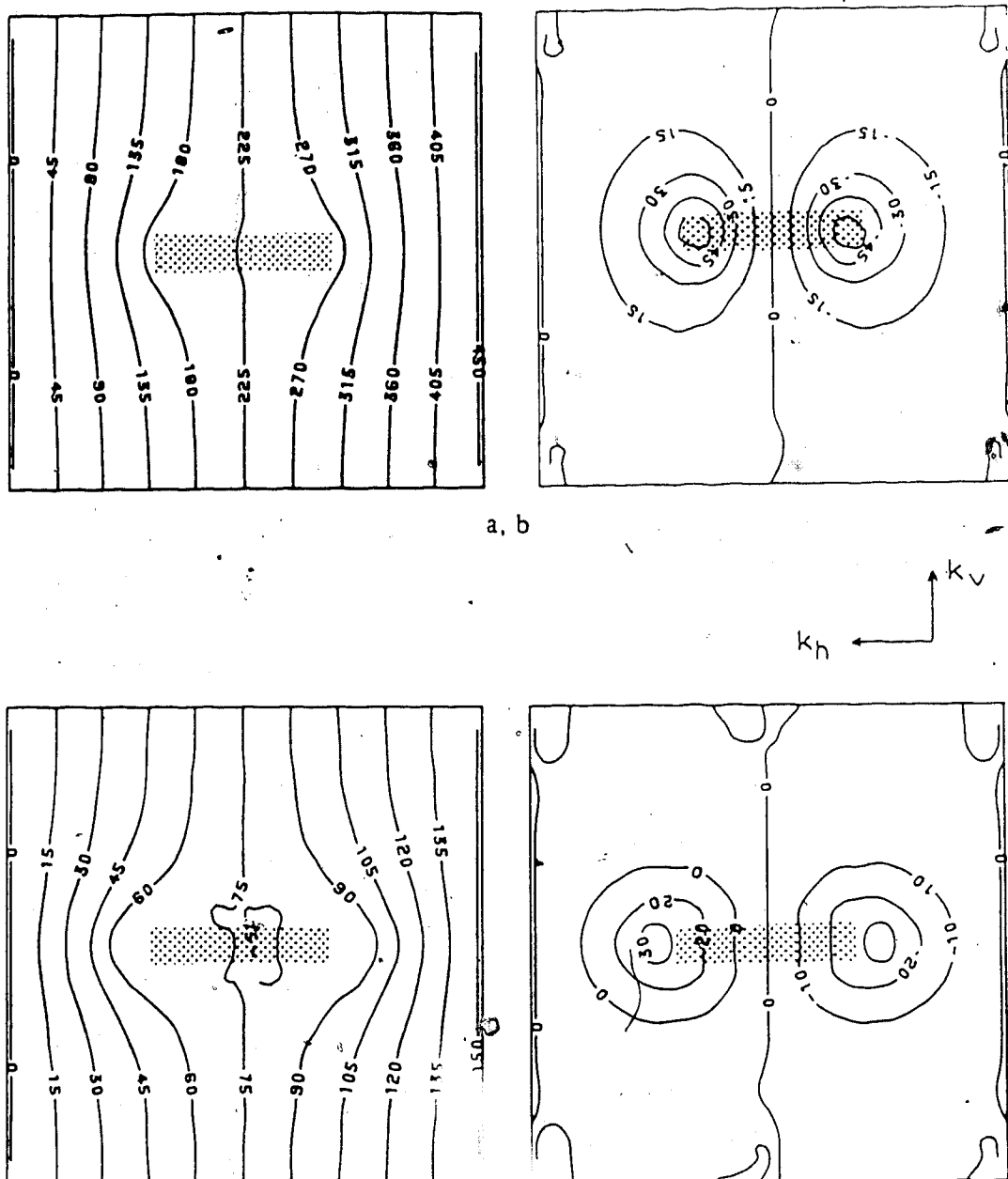


Figure 3.12 Potentiometric surface and anomaly maps illustrating the effect of vertical anisotropy, isotropic a, b and  $k_h = 2k_v$  c, d. Flow is from right to left.

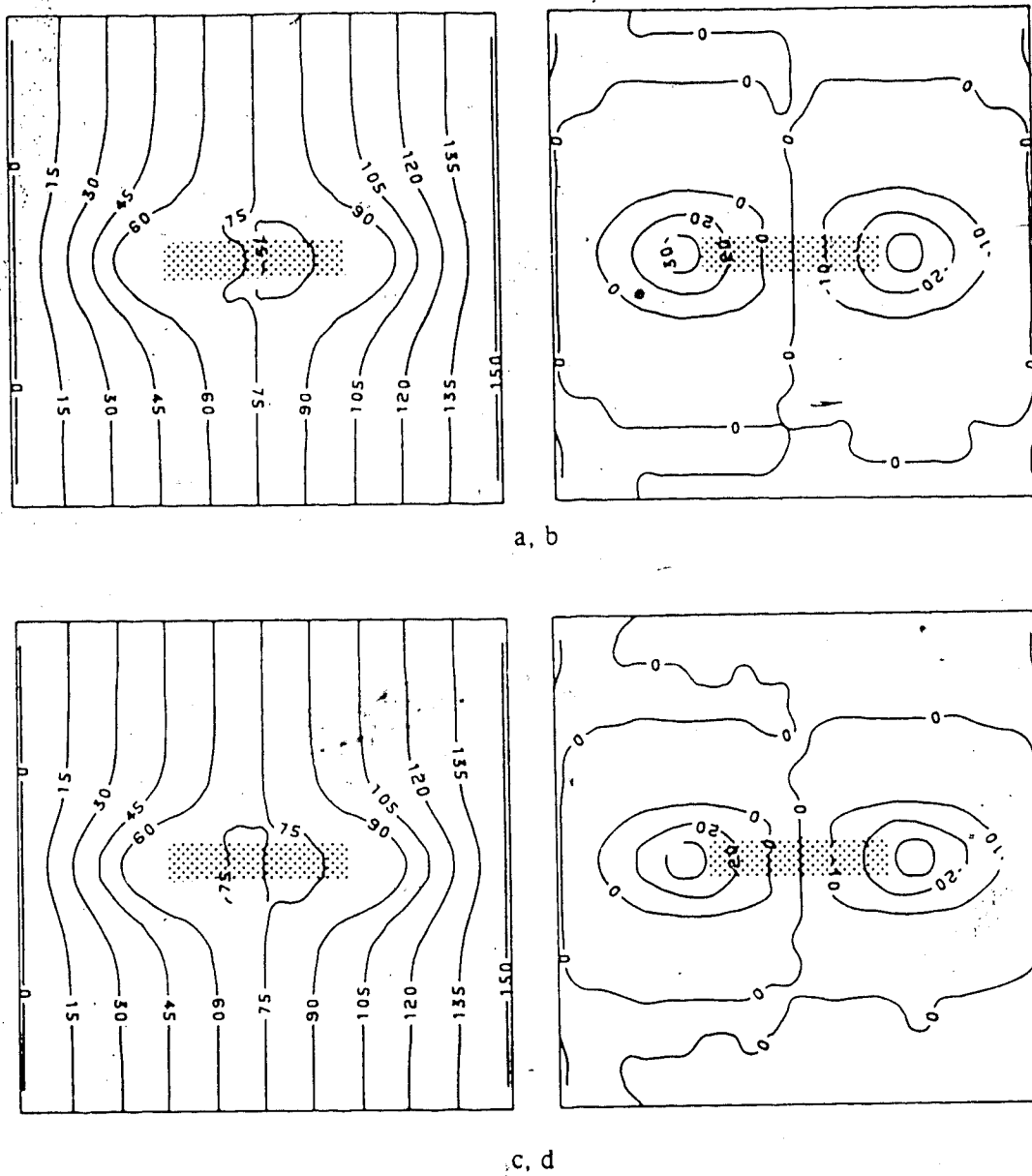


Figure 3.13 Potentiometric surface and anomaly maps illustrating the effect of vertical anisotropy,  $k_h = 5Xk_v$  a, b and  $k_h = 10Xk_v$  c, d. Flow is from right to left.

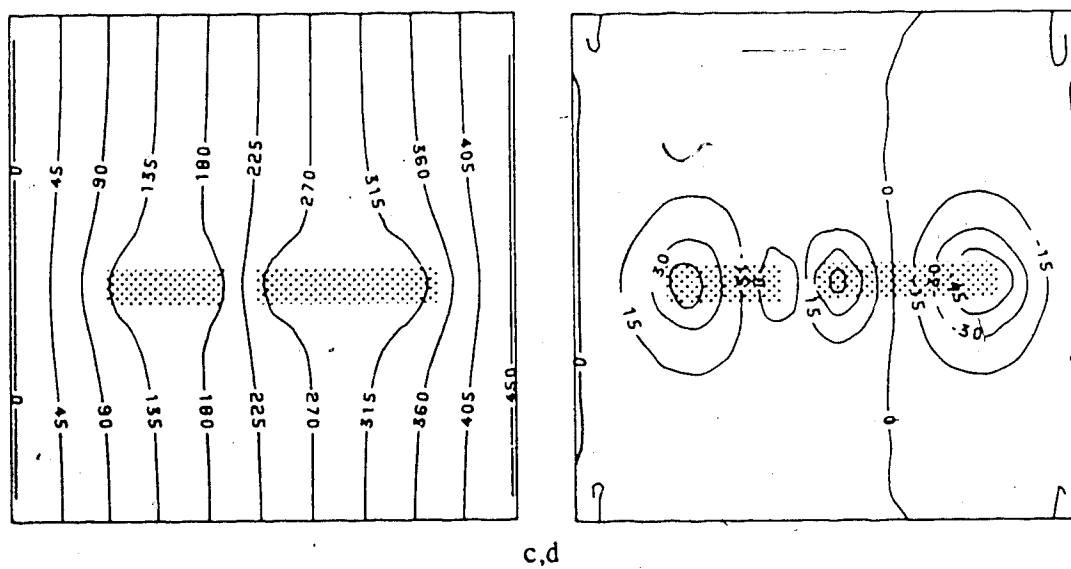
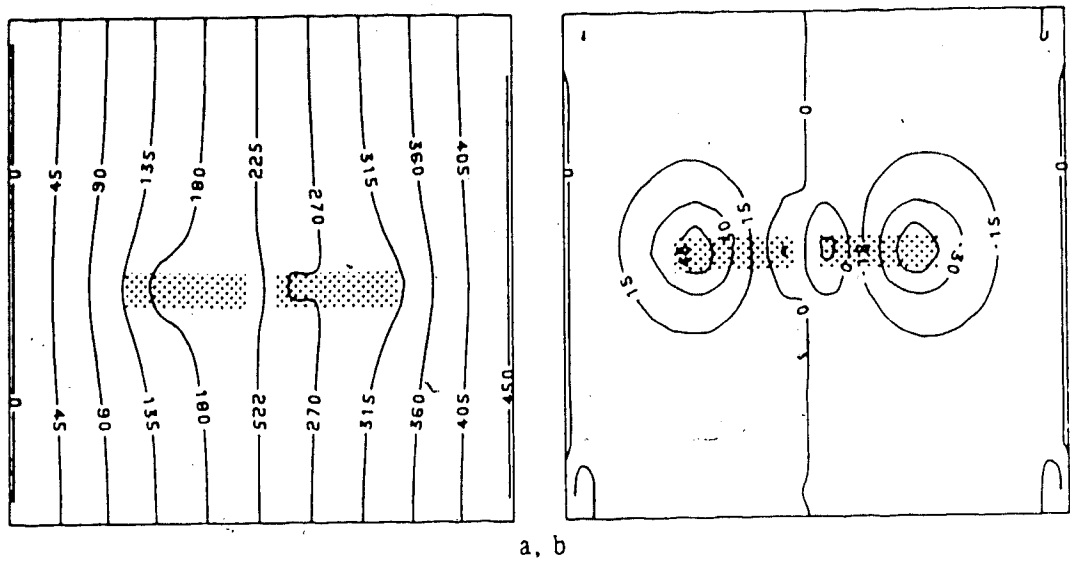


Figure 3.14 Potentiometric surface and anomaly maps due to interference effect of adjacent lenses, separation  $\ell/L = 1/6$  for two lenses of  $L:W = 5:1$  a, b, and for a lens of  $L:W = 3:1$  adjacent to a lens of  $L:W = 5:1$  c, d.



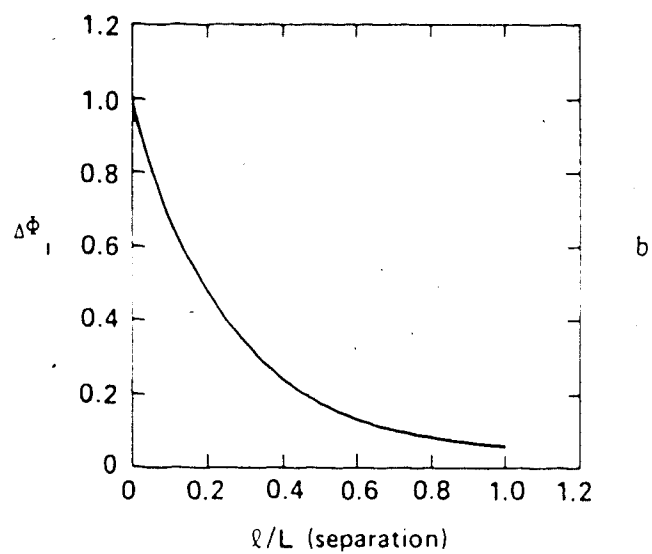
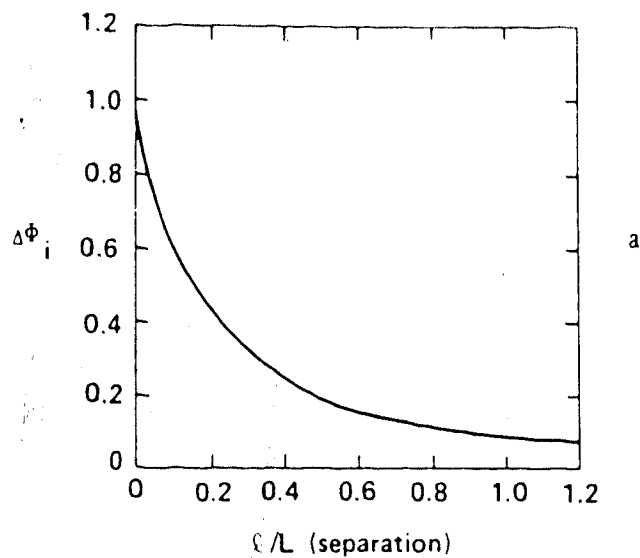


Figure 3.15 Attenuation of anomaly shift from the interference of adjacent lenses as they undergo separation parallel to flow a), and normal to flow b).

This figure has been omitted due to copyright restrictions on the material.

Source :

Tóth, J., 1970, Relation between electric analogue patterns of groundwater flow and accumulations of hydrocarbons: Canadian Journal of Earth Sciences, vol. 7, no. 3, pp. 988-1007.

Figure Number : 9

Page Number : 999

#### **4. FIELD STUDIES**

The objective of the field study is to apply the theory of the lens associated potentiometric anomaly to the exploration for reservoir quality rock bodies. The essential geologic-hydraulic components that must be satisfied prior to undertaking a field program are:

1. The stratigraphic interval of interest must contain reservoirs of a 'lenticular' nature, i.e. of limited areal extent.
2. The hydraulic gradient within the stratigraphic interval must be steep enough to develop anomalies sufficiently large to be detected by potentiometric mapping.
3. The data density must be high enough to identify anomalies and/or anomalous trends.

##### **4.1 STUDY AREA**

The field study area selected is between Townships 6-14 and Ranges 16-24W4M in southern Alberta (Figure 4.1). It lies partially within the study area treated by Tóth and Corbet (1986), on the regional groundwater flow systems of the area. Much of the petroleum exploration drilling has been limited to testing the Mesozoic section, within which the Lower Cretaceous Bow Island Formation (Figure 4.2) is frequently tested for its hydrocarbon potential. The Bow Island Formation is well known for its 'lenticular' sand developments which are sporadically distributed throughout the section with numerous intervening shales.

##### **4.2 REGIONAL BOW ISLAND FORMATION GEOLOGY**

The following section is a brief outline of the Bow Island Formations geology and is presented as an aid to hydrodynamic interpretation. Specific sedimentologic, depositional and stratigraphic-structural problems are not discussed in detail as they are beyond the scope of this study.

###### **4.2.1 Regional Structure**

The study area is flanked by two major structural features (Figure 4.3). To the east is the northward trending extension of the Sweetgrass arch, a large positive feature originating in

central Montana and intruded by the Kevin-Sunburst (K-S) dome in the vicinity of the international border. At the northerly terminus of the K-S dome the Sweetgrass arch diverges into a series of positive fingerlike ridges plunging northward towards the Suffield saddle. The western portion of the study area is flanked by the axis of the Alberta syncline, which underwent rapid subsidence during Upper Cretaceous through Tertiary sedimentation (Glaister, 1959). The structural elements shown on Figure 4.3 are based on Herbaly's (1974) contours on the top of the Devonian system, and presented on the structural contours of the lower Cretaceous Base of Fish Scales Marker (modified from E.R.C.B. Area No.1, 1978 and Area No.2, 1969, maps). Due to the Sweetgrass arch and K-S dome, the strike of the Base of Fish Scales Marker changes from an east-west orientation in the south-east part of the study area to a north-south orientation at the western edge of the study area, where it undergoes homoclinal flexure into the Alberta syncline. Other major features in the study area include, a northwesterly trending ridge which Herbaly (1974) termed the Taber-Enchant axis, and deep (down to basement) vertical to subvertical faults in the western portion of the study area. Hayes (1982) also noted the presence of faults of various types affecting Cretaceous, Jurassic and Mississippian strata in the vicinity of the Sweetgrass arch.

#### 4.2.2 Regional Stratigraphy And Lithology

The Bow Island Formation is part of the Blackleaf Member of the lower Cretaceous Colorado Group. It is the equivalent of the Taft Hill and Vaughn Members of the Black Leaf Formation in Montana and the Viking and Joli Fou Formations in east-central Alberta and Saskatchewan (Stelck and Armstrong, 1981) (Figure 4.2). The Bow Island Formation is underlain by a thick sequence of shales, silts and sands of the lower Cretaceous upper Mannville Formation and overlain by the upper Colorado shales, containing minor local sand developments (Barons sandstone and Second White Specks sandstone). The Base of Fish Scales Marker is generally agreed to be the boundary between the lower and upper Cretaceous (Stelck and Armstrong, 1981)

The Bow Island sands and conglomerates are believed to be derived from a westerly source and to have been deposited in a marine environment (Glaister, 1959). However, considerable controversy exists over the type of depositional system(s) that controlled the sedimentation process. Depositional processes proposed include turbidity currents (Beach, 1955, Roessing, 1959), tidal currents (Off, 1963, Evans, 1970) and storms (Simpson, 1975, Koldjik, 1976). Types of depositional sequences proposed are barrier bars (Tizzard and Lerbekmo, 1975, Boething, 1977), regressive sequences (Gammel, 1955, DeWiel, 1956, Jones, 1961, 1962), and transgressive sequences (Thomas, 1977).

The Bow Island Formation consists of interbedded dark grey (salt and pepper) protoquartzites and argillaceous protoquartzites. The percentage of feldspars, rock fragments and clay matrix increases towards the western source area (Glaister, 1959). Green shales, grey-green bentonitic shales and light grey bentonites containing abundant biotite and often some zeolite minerals (believed to be an alteration product of volcanic ash, Glaister, 1959, Tizzard and Lerbekmo, 1975) occur throughout the upper portions of the Bow Island Formation. Although the bentonitic beds are sporadically developed (due to their tendency to be eroded away when deposited in a high energy environment), they provide an excellent time marker for the purpose of stratigraphic correlation and are easily detected by gamma-ray, resistivity and density logs. At the top of the Bow Island Formation a chert rich pebble conglomerate bed is frequently developed which represents the best reservoir facies of the interval.

#### 4.3 REGIONAL HYDRODYNAMICS

Tóth and Corbet (1986) found the middle of the Colorado Group in the Taber area to be a zone of potentiometric minima, suggesting that the Bow Island Formation acts as a hydraulic sink. The present study confirms this observation. The hydraulic cross-section A-A' (Figure 4.4) indicates that flow is into the Bow Island Formation from the overlying Milk River Formation, and underlying lower Mannville Formation. The potentiometric surface maps from which Figure 4.4 was constructed are given in Appendix 4A. Previous

hydrodynamic studies conducted in the Bow Island Formation and its stratigraphic equivalent the Viking Formation by Berry (1960), Berry and Hanshaw (1960), Hill (1961), Hitchon (1969b), Dickey and Cox (1977), Schwartz et al (1981) have all presented data showing the Bow Island Formation's pressure to be sub-hydrostatic (subnormal). Subnormal pressures have also been reported in the Appalachian region (Russell, 1972), Anadarko basin (Marousa, 1973), San Juan and Arkoma basins (Dickey and Cox, 1977) and Michigan basin (Short, 1979). Clearly the phenomenon of subhydrostatic formation pressure is not uncommon, and a host of different theories have been forwarded to explain it. These have been summarized by Bradley (1975) and include:

1. The chemico-osmotic effect.
2. Compaction and capillary pressure differentials.
3. Temperature changes due to orogenic movements or erosion and deposition.
4. Erosion with a resultant dilation of pore-volume.
5. A combination of transient, gravity induced flow systems and pore dilation due to erosional unloading.

Early studies by Berry (1960), Berry and Hanshaw (1960), Hill et al (1961) and Hitchon (1969b) attributed the Bow Island-Viking underpressuring to osmotic pressure imbalances across semi-permeable (shale) membranes. According to Hill (1961):

*"for highly compacted shale membranes having an abundance of clay minerals, osmotic pressures can reach 83-103 KPa (12-15 psi) for each 1,000 ppm difference in water salinity".*

Formation water salinities in the study area (see Table 4.1) generally increase progressively with depth, the only major salinity contrast occurring at the Devonian-Mississippian boundary. However, since formation pressures do not vary significantly across this boundary, it would appear that the marked salinity contrast fails to produce any chemico-osmotic effect. It seems very unlikely therefore, that the osmotic pressure imbalances play any significant role in the maintenance of sub hydrostatic pressures within the Bow Island Formation.

Table 4.1 Averaged formation water salinities through study area.

STRATIGRAPHIC INTERVAL	AVERAGE SALINITY TOTAL DISSOLVED SOLIDS X 1000 PPM
Upper Cretaceous	4 - 7
Lower Colorado	5 - 13
Lower Cretaceous	7 - 25
Jurassic-Carboniferous	10 - 30
Upper Devonian	< 100

### 4.3.1 The Erosional Rebound Theory

The dilation effect proposed by the Erosional Rebound Theory is based upon the slightly elastic nature of consolidated sedimentary rocks. The deformation of a rock in response to changes in the vertical component of effective stress is expressed as the modulus of compressibility, for a sandstone, a pressure of 1 psi results in a change of  $7 \cdot 10^{-6}$  pore volumes, with shale having even higher compressibility Fatt, 1958. The removal of a portion of the vertical stress (i.e. by erosion) allows an elastic expansion of the rock, although the expansibility is generally less than the compressibility (depending upon rock type and loading history). If the rock expansibility is greater than that of water ( $3 \cdot 10^{-6}$  volumes/psi), the dilated pore volume will not be completely taken up by expanding water, resulting in a decrease of the pore-pressure, and a proportional reduction of the fluid potential. Neuzil and Pollock (1983) suggested that erosional unloading could conceivably yield negative pore-pressure or tension in thick aquitards. When erosion occurs at a faster rate than fluid-flow (which is a response to the changing boundary conditions), the flow system will remain transient until adjusted to the new boundary conditions. Pore-pressure adjustment rates due to erosional modification of the landsurface were first calculated by Tóth and Millar, 1983 for the Red Earth region of northern Alberta and later applied to the Taber area of southern Alberta by Tóth and Corbet, 1986.

A conceptual model of the evolution of groundwater flow systems due to erosional unloading in a simple basin is presented in Figure 4.5. The established steady-state flow system at  $t = t_{\infty}$ , under topography  $S_1$  is given in Figure 4.5a. When the topography is altered to  $S_2$  at  $t = t_0$  (Figure 4.5b) the aquitard dilates and an underpressured zone develops, causing disruption of the  $S_1$  flow system. At  $t = t_1$  the  $S_1$  flow system has all but dissipated, and the aquitard acts as a hydraulic sink (Figure 4.5c). This figure represents the present day situation of the Colorado aquitard in southern Alberta. In Figure 4.5d the flow system has completely adjusted to the  $S_2$  land surface and the hydraulic sink has equilibrated,  $t = t_{\infty}$ .

Using the above concept Tóth and Corbet (1986) have classified three distinct flow regimes in southern Alberta, these are:



1. The Modern Land Surface System, reaching a depth of 300m (mostly post-Colorado strata).
2. The Erosional Rebound System, Colorado Group and upper Mannville Formation.
3. The Cypress Plains System, lower Mannville and subjacent strata, which is a relict flow system adjusted to Paleocene (58Ma) to Eocene (36Ma) paleo-topography.

#### 4.3.2 Effects Of Complex Flow Systems

The discussion presented above suggests that the regional flow systems of southern Alberta are complex and not all at steady-state. But, the important factors to consider when searching for lens associated potentiometric anomalies are the following:

1. Basinal flow systems do not develop or dissipate instantaneously due to the generally small flow velocities, and should be considered over the geologic time scale.
2. Potentiometric anomalies and hydrocarbon accumulations may be transient, but once developed, the introduction of alternate boundary conditions requires an adjustment time through which dissipating ghost or relic anomalies and hydrocarbons accumulations will persist.
3. If potentiometric data indicate the presence of an anomaly and the hydraulic conditions for hydrocarbon entrapment exist; then the steady or transient nature of the flow system (regardless of its generative process) should not affect the utility of the lens associated potentiometric anomaly as an exploration tool.

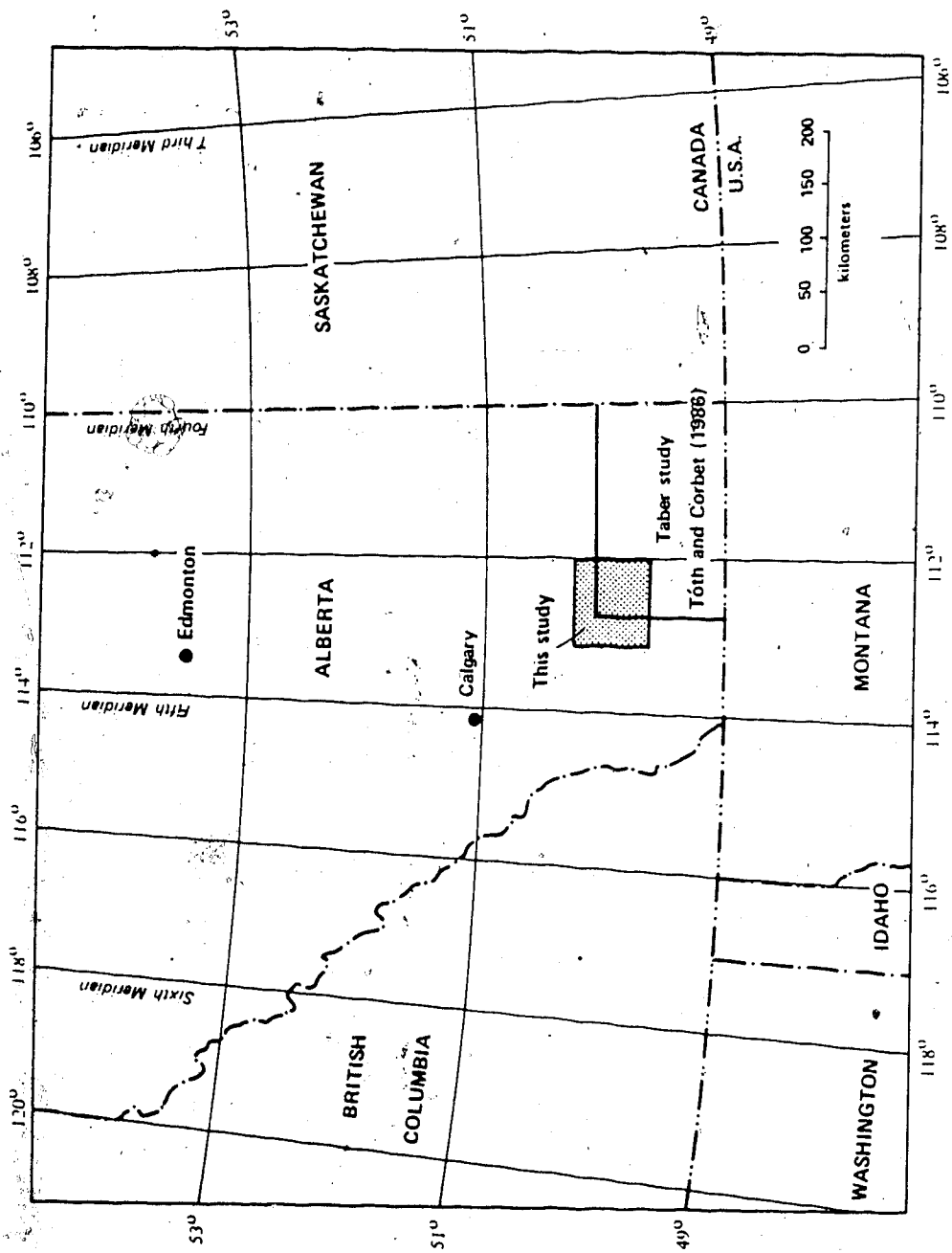


Figure 4.1 Study area in regional context.


	NORTHEAST WYOMING	SWEET GRASS ARCH MONTANA	LETHBRIDGE AREA ALBERTA	EAST CENTRAL ALBERTA	CENTRAL FOOTHILLS ALBERTA
UPPER CRETACEOUS	NIOBRARA	KEVIN MBR	U-COLORADO	First White Specks	WAPIABI FM
	CARLILE	FERDIG MBR			CARDIUM ss
	GREENHORN	CONE MBR	U-COLORADO SHALE	Second White Specks	OPABIN MBR
	BELLE FOURCHE	FLOWEREE MBR			HAVEN MBR
		? 			VIMY MBR
LOWER CRETACEOUS	MOWRY	BOOTLEGGER MBR	BLACKLEAF MBR OF COLORADO SHALE	Fish Scale	BLACKSTONE FM
	SHELL CREEK	VAUGHN MBR			
	NEWCASTLE	TAFT HILL MBR		Red Specks	
	SKULL CREEK			BOW ISLAND SANDS	
	FALL RIVER	FLOOD MBR		JOLI FOU EQUIV.	
				BASAL ss	
					SUNKAY MBR
UNDERLYING BEDS	CLOVERLY reference std.	KOOTENAI (Cobban et al 1976)	BLAIRMORE Spratt (1931) em	MANNVILLE std.	BLAIRMORE (Stott, 1963)

Figure 4.2 Table of formations, showing correlative stratigraphy. Adapted from Stelck, 1981.

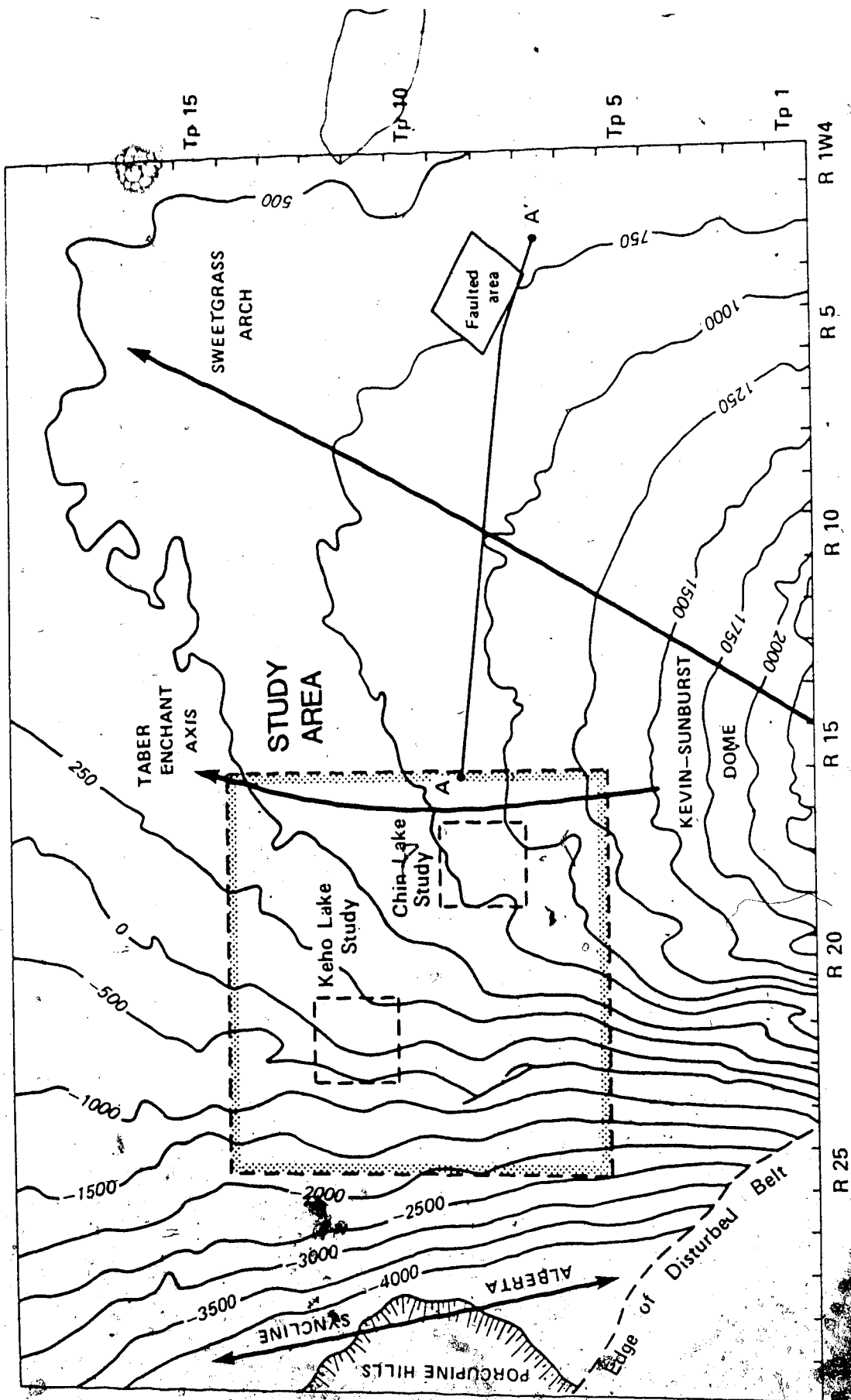


Figure 4.3 Regional structural elements given on top of the Base of Fish Scales Marker.

structural contours modified from the E.R.C.B. Area No.1, 1978 and Area No.2, 1969 maps.

This figure has been omitted due to copyright restrictions on the material.

Source :

Tóth, J., and T. Corbet, 1986, Post-Paleocene evolution of regional groundwater flow-systems and their relation to petroleum occurrences, Taber area, southern Alberta, Canada :  
Bulletin of Canadian Petroleum Geology, vol.34, no.3, pp. 339-363.

Figure Number : 24

Page Number : 357

This figure has been omitted due to copyright restrictions on the material.

Source :

Tóth, J., and T. Corbet, 1986, Post-Paleocene evolution of regional groundwater flow-systems and their relation to petroleum occurrences, Taber area, southern Alberta, Canada :  
Bulletin of Canadian Petroleum Geology, vol.34, no.3, pp. 339-363.

Figure Number : 22

Page Number : 356

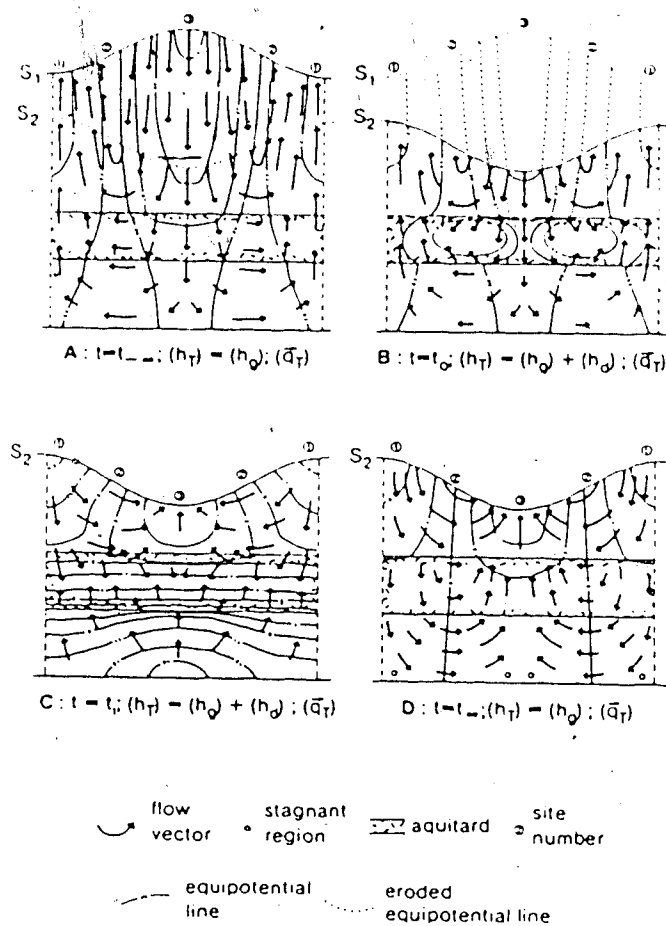


Figure 4.5 Conceptual evolution of hydraulic head distribution in simple basin at times : a)  $t_{-∞}$ , b)  $t_0$ , c)  $t_i$  and d)  $t_{+∞}$ , adapted from Tóth and Corbet, 1986.

#### 4.4 POTENTIOMETRIC SURFACE MAPPING

The regional potentiometric surface map was constructed using all available drill stem tests (up to 1983) conducted within the Bow Island Formation in the study area. The processed data were obtained from the Canadian Institute of Formation Evaluation (Calgary, Alberta) who provided extrapolated shut-in pressures (see section 2.2.2), type of fluid(s) recovered, DST quality, pressure-recorder and Kelly Bushing elevations. These data were then standardized using the following procedure :

1. Only A,B, and C quality tests (see Appendix 4b.1 for quality criterion) were used which reduced the data set from 759 to 376 tests.
2. To reduce the effect of any vertical hydraulic gradient, only those DST's at or near the top of the Bow Island Formation were used, reducing the data set from 376 to 237 tests.
3. For multiple tests in the same horizon, hydraulic head values were averaged.
4. Equation 2.10 was used to calculate hydraulic head values using a constant fresh water salinity of 10,000 ppm which corresponds to a density gradient of 0.437 lb/ft . The permanent datum used is sea level.

##### 4.4.1 Potentiometric Surfaces - First Bow Island S.S. and Second White Specks S.S.

The contoured potentiometric surface map of the Bow Island Formation is given in Figure 4.6. The potentiometric surface (hydraulic gradient) slopes mainly towards the south south-west, with a relatively flat area ( $\partial h / \partial x \approx 0.005-0.01$ ) in the northeast and a steep flexure ( $\partial h / \partial x \approx 0.02$ ) through the central portion of the map trending south-east to north-west. South-west of the flexure the hydraulic gradient flattens somewhat ( $\partial h / \partial x \approx 0.01-0.015$ ) and the equipotentials begin to attain a north-south orientation.

As a check to determine the reproducibility of the Bow Island Formation potentiometric surface and the vertical component of the hydraulic gradient, a potentiometric surface map was constructed for the Second White Specks horizon. This interval is not frequently tested and only 66 usable DST's were available for the calculation of hydraulic head. The borehole locations are posted and the hydraulic head values contoured in Figure



4.7. The map indicates generally lower hydraulic potential within the Second White Specks than for the Bow Island Formation throughout the study area, suggesting that the potential minima shown in Figure 4.4 occurs in the vicinity of the Second White Specks interval or higher. The characteristics of the Bow Island and Second White Specks potentiometric surfaces probably reflect several factors:

1. Hydraulic conductivity is better in the north-east sector than to the south-west, which explains the relatively low hydraulic gradient in the north-east. The enhanced conductivity may be associated to fracture systems from the Taber-Enchant axis and/or the presence of a more permeable facies in the north-east. The area has also undergone considerable production induced drawdown (PID), which can create depressions in the potentiometric surface.
2. Interpretation of the rank and moisture content of Mannville coals (Deroo et al, 1977) suggest that approximately 2200m of overburden was required at the east flank of the Alberta syncline (Figure 4.3), in the area of the present day location of Porcupine Hills. The removal of progressively thicker amounts of overburden westward is expected to enhance the erosional rebound effect, resulting in progressively decreasing hydraulic head.
3. The total overburden and upper Cretaceous section thickness increase westward as the Alberta syncline is approached. This means that the time required for the Colorado Group to adjust to the modern land surface induced flow system increases to the west. The potentiometric surface in the eastern portion of the study area are closer to being adjusted to the present day land surface than in the west.

#### 4.4.2 Method Of Selection And Study Of Potentiometric Anomalies

The theoretical analyses conducted in the previous chapter showed that the magnitude of potentiometric anomalies generated due to flow through relatively permeable bodies, are directly proportional to the hydraulic gradient. Since an anomaly of a large magnitude (a major distortion of the potentiometric surface) is more "visible" than a smaller one, the anomalies investigated in this thesis were sought in areas with steep hydraulic gradients. The

north-west south-east trending flexure in the potentiometric surface of the Bow Island Formation (Figure 4.6), has a hydraulic gradient of  $\approx 0.02$ , similar to that used in the theoretical modelling of the previous chapter. Therefore, the magnitude, pattern and areal extent of the simulated anomalies provide a guide, which upon familiarization, should aid in the selection of potentiometric anomalies for study.

The criteria used for selecting anomalies (or prospecting for lenticular reservoirs) is fairly simple; assuming the area under investigation has a linear hydraulic gradient, any divergence of equipotentials should be due to the presence of relatively more permeable rock bodies. Note that equipotential anomalies will also occur if the potentiometric surface has been affected by externally induced stress, such as fluid production from, or injection into reservoirs. With these considerations in mind, the initial field study will determine if randomly selected anomalies of the regional potentiometric surface are indeed caused by the presence of relatively permeable, lenticular rock bodies.

The steps taken to document the lens associated potentiometric anomaly in the field are listed below :

1. Analyse all the available cores taken in the Bow Island Formation within the study area and correlate lithology to geophysical log response. This aids in the construction of geological cross-sections and permits estimation of lithology where cores are not available.
2. Obtain and map the permeability distribution within the upper Bow Island Formation throughout the detailed study area. Most of the permeability data are calculated from drill stem tests (as described in Chapter 2), but these are supplemented by core-derived permeabilities where available. In instances where neither were available, a qualitative estimate of lithology was made (as described above), to which a permeability range was assigned. The range is based on permeability analysis of full diameter core for a suite of representative lithologies from the Bow Island Formation, courtesy of Core Laboratories Inc. (Calgary, Alberta). The technique used by Core Laboratories Inc. for permeability measurement has a lower detection limit of 0.01 md, all unfractured shales and most

silty-shales had permeabilities below the detection limit. Since most conventional DST's conducted in similar strata either do not recover enough fluid or have a shut-in curve that is too unstable for permeability calculations, the lower permeability detection limit is in effect set at 0.01 md. A survey of literature (Freeze and Cherry 1979, Brace 1980 and Tóth and Corbet 1986), indicates the range of shale permeability to be  $\approx 0.1$  md - 0.01  $\mu$ d. Thus, the lower detection limit of this study represents the upper limit of the shale permeability spectrum. Consequently, to boreholes that encountered shale or silty-shale at the top of the Bow Island Formation and for which quantitative permeability measurements do not exist, a value of  $< 0.1$  md was assigned.

3. Determine if any production has taken place and its effects on the observed potentiometric surface.
4. Determine fluid saturations (hydrocarbon content) and fluid contact relationships, if possible.
5. Verify the observed potentiometric surface distribution by the steady-state numerical simulation of groundwater flow using the mapped permeability distribution and regional boundary conditions.

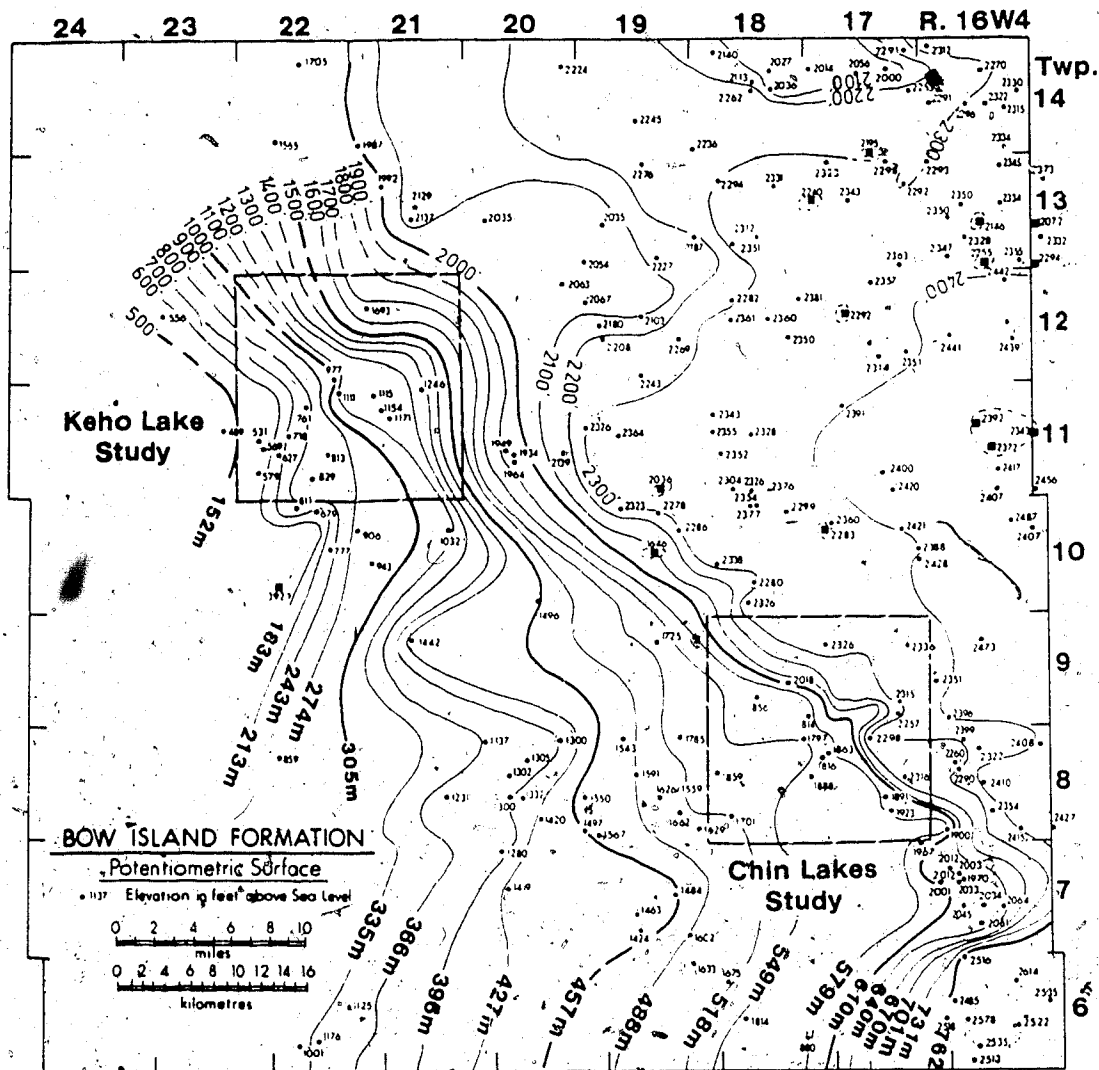


Figure 4.6 Potentiometric surface of the Bow Island Formation. Circular points are hydraulic head values calculated near the top of the Bow Island, the square points are values influenced by production induced drawdown.

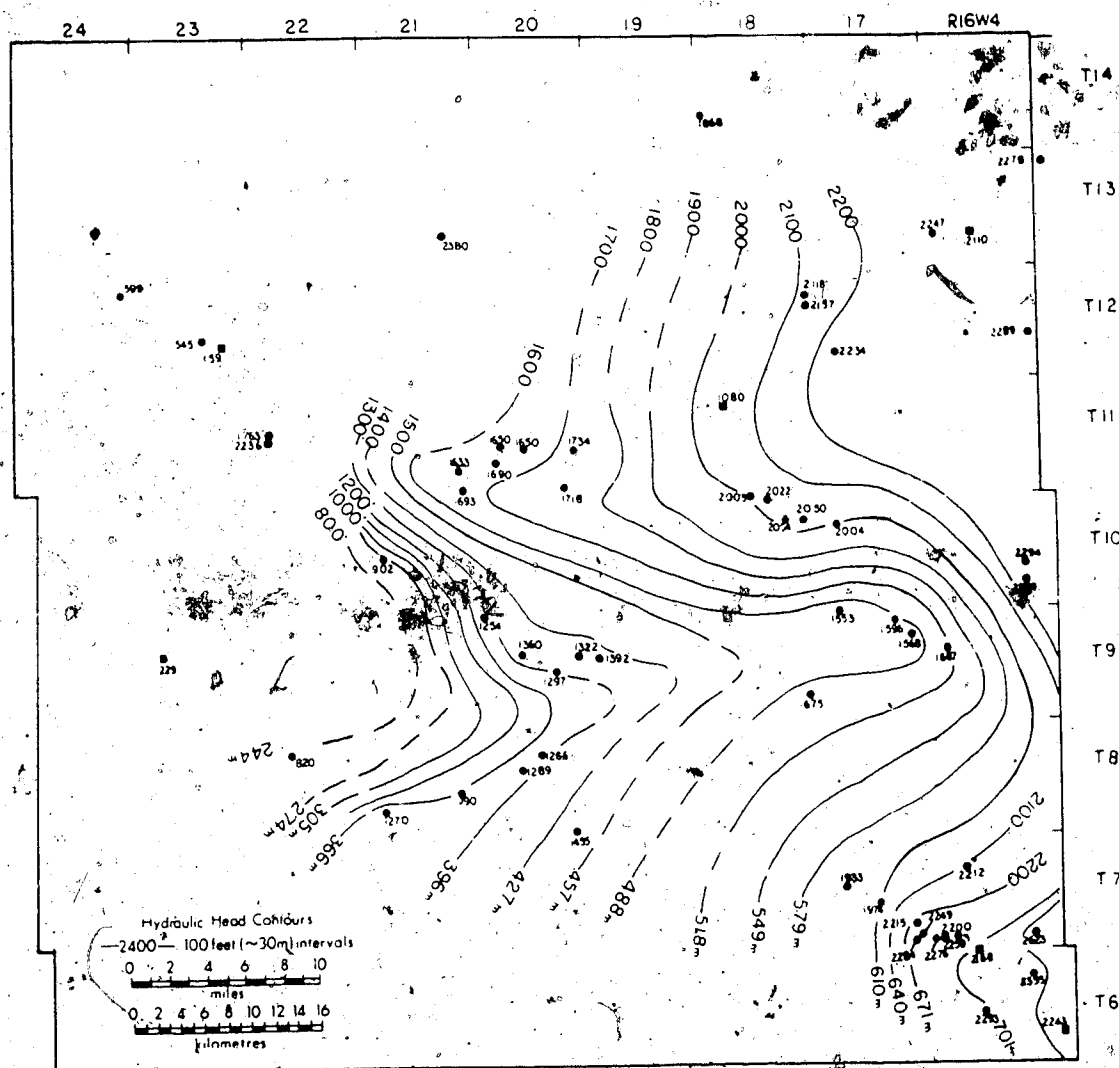


Figure 4.7 Potentiometric surface of the Second White Specks zone. The square data points appear to be influenced by production induced drawdown, and the hexagonal points are anomalously super-hydrostatic. These were not used in the contouring.

#### 4.5 KEHO LAKE STUDY AREA

The Keho Lake study area was chosen on the basis of a large anomalous feature of the regional potentiometric surface, Figure 4.6, located between Townships 11-12 and Ranges 21-22W4M. A considerable amount of data used in the detailed study was obtained after the regional study had been completed as a result of post 1983 drilling activity to the northeast of the main anomaly in T12, R21W4M. The geology of the area is based on an examination of 44 geophysical logs, 8 cores and chip samples from several wells, Figure 4.8. All the available cores were limited to a section between the Base of Fish Scales Marker and the upper portion of the Bow Island Formation. For the purpose of showing log response to lithologic variation and the criterion used for selecting correlation markers, a composite strip log from the Base of Fish Scales zone to the top of the Mannville Formation is presented in Figure 4.9. Core descriptions have been superimposed on the log where available, however most of the log is based on chip samples from the well Onyx et al Keho 16-11-12-21W4M. The ranges given in Figure 4.9 are based on a combination of core and DST derived permeabilities where available (generally only for coarse grained sediments) and on literature values for fine grained sediments. The log is given as an interpretive guide only - since any of the sands may pinch or swell laterally due to their lenticular nature. Detailed core logs for the Keho Lake area are given in Appendix 4A.1, a list of the location and logged intervals is given in Table 4.2.

##### 4.5.1 Keho Lake Study - Geology

Based on the core and geophysical log study several geological cross-sections were constructed through the area. Figures 4.10 and 4.11 are strike and dip sections B-B' and C-C' respectively, the correlation lines used are for the Base of Fish Scales Marker, top of the Bow Island Formation and a bentonitic shale bed occurring between the first and second Bow Island sands (BIS 1 and BIS 2). Structural contours on top of the Bow Island Formation, Figure 4.12, indicate a north-westerly dip of approximately 10m/km ( $\approx$  50ft/mile). The main structural features are the south-east to north-west trending (sub-vertical ?) faults which displace Mississippian strata on reflection seismic profiles through the area (pers. comm.).

Onyx Petroleum Ltd., Calgary, Alta.). The southwest fault has up to 60m displacement, whereas the north-east fault has approximately 25m maximum displacement, which appears to lessen towards the south-east in a scissors-like manner. The undulations of the structural contours are due in part to paleotopography created by stacked sand ridges in the upper Bow Island Formation as indicated on the cross-sections, Figures 4.10-4.11 and may also be due in part to the effects of folding possibly associated to the faulting activity.

#### 4.5.2 Potentiometric Surface and Interval Permeability Distribution

The detailed potentiometric surface of the Keho Lake study area is based on 34 DST derived hydraulic head values. Examination of production data from the Energy Resources Conservation Board of Alberta and sample calculations do not indicate any significant production induced drawdown (PID). The exception may occur at the site of the well Onyx et al Keho 16-3-12-21W4M, where 4 wells had already been on production in an apparently contiguous reservoir prior to the DST date. Therefore, less weight was given to the 16-3 well during the contouring of Figure 4.13.

Six distinct anomalies, designated A<sub>1</sub> to A<sub>6</sub>, of the Bow Island Formations potentiometric surface have been outlined in Figure 4.13. Anomaly A<sub>1</sub> was the original target of the regional prospecting and A<sub>2</sub> was defined due to recent drilling. Anomalies A<sub>3</sub> to A<sub>6</sub> are subsidiary to the main study since the control in their vicinity is poor, these will be discussed in more detail in the following sections.

To identify the cause of the anomalies at A<sub>1</sub> and A<sub>2</sub>, it was necessary to determine the permeability distribution through the zone(s) in which the DST's used to calculate hydraulic head were conducted. The calculated permeability distribution in the area is given as an interval permeability map, ( $k \cdot b = md \cdot m$ ). There are three distinct clusters (lenses ?) defined in Figure 4.14, which have been designated as L<sub>1</sub>, L<sub>2</sub>, L<sub>3</sub>. However, due to the lack of permeability data between L<sub>1</sub> and L<sub>2</sub>, their geometry is not immediately tenable, therefore, the contouring represents a preliminary interpretation. A method of better defining the lens geometries will follow in the next section.

The permeable bodies of Figure 4.14 represent the distribution of conglomerate beds, the occurrence of which was discussed in Chapter 4.2. Descriptions of the conglomerate are given in Appendix 4A.1 wells 16-9-12-21W4M, 14-10-12-21W4M and 6-1-12-22W4M. In general the conglomerate is poorly cemented, it has an average porosity of 12-15% and a permeability range of 100-5500 md; porosity and permeability reduction is mainly due to calcite cementation. Laterally, the conglomerate beds may grade into a silty-shale with a corresponding reduction in permeability to  $< 0.1$  md, which probably represents the upper range of permeability for this rock type (see previous section on method of study). Recalling the theoretical analysis of Chapter 3, when flow occurs normal to the long axis of a permeable body (as in this case) the threshold permeability contrast  $\epsilon_t$  required (between lens and matrix) to approach the maximum anomaly is less than 30. The indicated permeability contrast in the area of 3 to 4.5 orders of magnitude (between  $L_{1,2}$  and their surrounding matrix) is well above that required to produce the maximum anomaly possible for the hydraulic gradient present. Furthermore, the strong correlation between the location of anomaly  $A_{1,2}$  (Figure 4.13) and  $L_{1,2}$  (Figure 4.14) suggests that the potentiometric anomaly selected during the initial prospecting is indeed due to the presence of a highly permeable geologic body.

#### 4.5.3 Verification of Observed Anomaly By Numerical Simulation

To verify the observed potentiometric surface with that which would be theoretically expected, numerical simulation of groundwater flow using the USGS Modular Groundwater Flow Model (MGFM), McDonald and Harbaugh, 1983, was conducted. The discretized model of the study area shown in Figure 4.15, uses the mapped interval permeability distribution from Figure 4.14 and boundary conditions derived from the regional potentiometric surface map (Figure 4.6). Discontinuities due to faulting that may be present in the area were not included due to the difficulty of determining the effects of faulting on the permeability distribution, so the modelled area was kept within the main faults outlined in Figure 4.12.



The calculated potentiometric surface, Figure 4.15 is similar in pattern to that observed in the field (Figure 4.13), supporting the initial interval permeability interpretation (Figure 4.14). However, the areal extent of the distortion produced is considerably larger in the calculated case. The areal extent of potentiometric surface distortions is sensitive to two factors which are investigated in the following section :

1. Permeability contrast between the lens and matrix ( $\epsilon$ ) below the threshold value ( $\epsilon_t$ ) required to approach the maximum anomaly magnitude.
2. Geometry of the lens.

#### 4.5.4 Predictive Modelling-Inferred Permeability Distribution

The use of unrealistically high permeability values for the simulation was the first factor considered as a likely cause of the discrepancy between the observed and calculated potentiometric surfaces. This situation may arise from the use of effective permeability ( $k_e$ ), for construction of the interval permeability map. Effective permeability is the permeability of the drill stem tested interval to the fluid type (gas, water or oil) produced from that interval. However, the relative permeability ( $k_r$ ) of one of these fluids is reduced as the volume of the pore space taken up by a different fluid increases, Figure 4.16. To correct for this, fluid saturations for the modelled lenses ( $L_{1,2,3}$ ) were calculated and the relationship from Figure 4.16 used to determine  $k_r$ . Actual reservoir oil and gas saturations in the study area average 60%, resulting in a relative permeability of the reservoir rock to fresh water flow ( $k_r$ ) of  $\approx 0.1 \cdot k_e$  in the presence of oil and  $\approx 0.02 \cdot k_e$  in the presence of gas. In shales (the surrounding matrix), it is difficult to calculate the percent hydrocarbon saturation using borehole resistivity measurements as above. A rough approximation may be made by using a total organic carbon content of 1-2% by weight, for the Colorado shales (Deroo et al, 1977) and a hydrocarbon generation efficiency of 10% - a relatively generous figure (Hunt, 1979), which would yield 0.1-0.2%  $C_{1,2}$  hydrocarbons by weight, with expulsion from the source rock reducing this figure further. In comparison a reservoir with 15% porosity and 60% oil saturation has greater than 3% hydrocarbons by weight. These figures suggest that

hydrocarbon saturation in the reservoirs is a minimum of an order of magnitude greater than in the surrounding matrix, and that relative permeability adjustments for the matrix may be ignored for all intents and purposes. Despite the above considerations, however, and using  $k_r$ , the permeability contrast ( $\epsilon$ ) between the lens and matrix is still greater than 2 orders of magnitude. The resulting numerical simulation produces an identical potentiometric surface to that shown in Figure 4.15, suggesting that the cause of the discrepancy between the observed and simulated potentiometric surfaces is most probably in the interpretation of lens geometry.

By iterating between the field derived and modelled interval permeability distribution, it should be possible to produce a best fit lens geometry for which the calculated and observed potentiometric surfaces are in agreement. A more sophisticated approach to this task may be attempted by the automatic solution of the "inverse problem" (using the known hydraulic head distribution to solve for permeability). Various methods to this end have been proposed in the literature, i.e. Emsellen and Marsily, 1971, Frind and Pinder 1973, and Neuman, 1973. Methods of assessing the reliability of the inverse solution statistically have been forwarded by Cooley 1977, and Neuman and Yakowitz, 1979 and applied to real data by Cooley, 1979 and Neuman et al, 1981.

Figure 4.17 is the calculated potentiometric surface after three iterations adjusting the permeability distribution, using the trial and error method of inverse modelling. The potentiometric surface distribution of the adjusted model, although not an exact replica is very similar to the observed potentiometric surface (Figure 4.13), including the reproduction of the postulated anomaly at A<sub>1</sub>, for which a permeable block was added to the model. It is suspected from the regional hydrological work that the present day flow systems are in a transient state and would not be reproducible by steady-state modelling. The final interpretation of the interval permeability distribution within the study area is given in Figure 4.18.

#### 4.5.5 Fluid Distribution

The fluid distribution of the BIS I unit given in Figure 4.25 is based on reported DST recoveries and the E.R.C.B. Oil and Gas Pool Maps (1981). The observed fluid distribution pattern is highly complex and gas/oil/water contact relationships are not readily discernible using the standard interpretation techniques of buoyancy induced segregation and/or tilted contacts due to hydrodynamic flow. The contacts given in Figure 4.19 are the "observed" relationships based on the type of fluids recovered from DST's or production data, no attempt is made to determine the actual gas/oil/water contacts.

Examination of fluid distribution with respect to the location of potentiometric anomalies (Figure 4.19) indicates that most of the permeable lenses in the area are hydrocarbon bearing. The main anomaly A<sub>1</sub> is a shut-in gas field, the small lens to its immediate south-west was a marginal oil producer that was abandoned due to excess water production. Anomaly A<sub>2</sub> is an oil field, lens L<sub>3</sub> (on Figure 4.14) which is not identified as an anomaly (on Figure 4.13) due to the lack of data, is a small gas field. Anomalies A<sub>3</sub> and A<sub>4</sub> are both producing gas fields and anomalies A<sub>5</sub> and A<sub>6</sub> are postulated locations of permeable lenses. It should be noted that after the initial construction of Figure 4.14 two new wells were drilled in the area, the 6-30-11-21W4M well drilled outside of A<sub>1</sub> was dry and abandoned, the 16-3-12-21W4M well drilled at the south-east fringe of the subsidiary A<sub>1</sub> anomaly is a marginal oil well, both of which were incorporated into the data set.

Table 4.2 Intervals and locations of cores logged in the Keho Lake study area.

LOCATION CORE LOGS	INTERVAL (m)
16-9-12-21W4	966-971
6-10-12-21W4	942-953
14-10-12-21W4	956-969
16-10-12-21W4	962-980
16-11-12-21W4	942-960
16-15-12-21W4	972-990
6-1-12-22W4	1054-1064
6-13-12-22W4	1071-1087

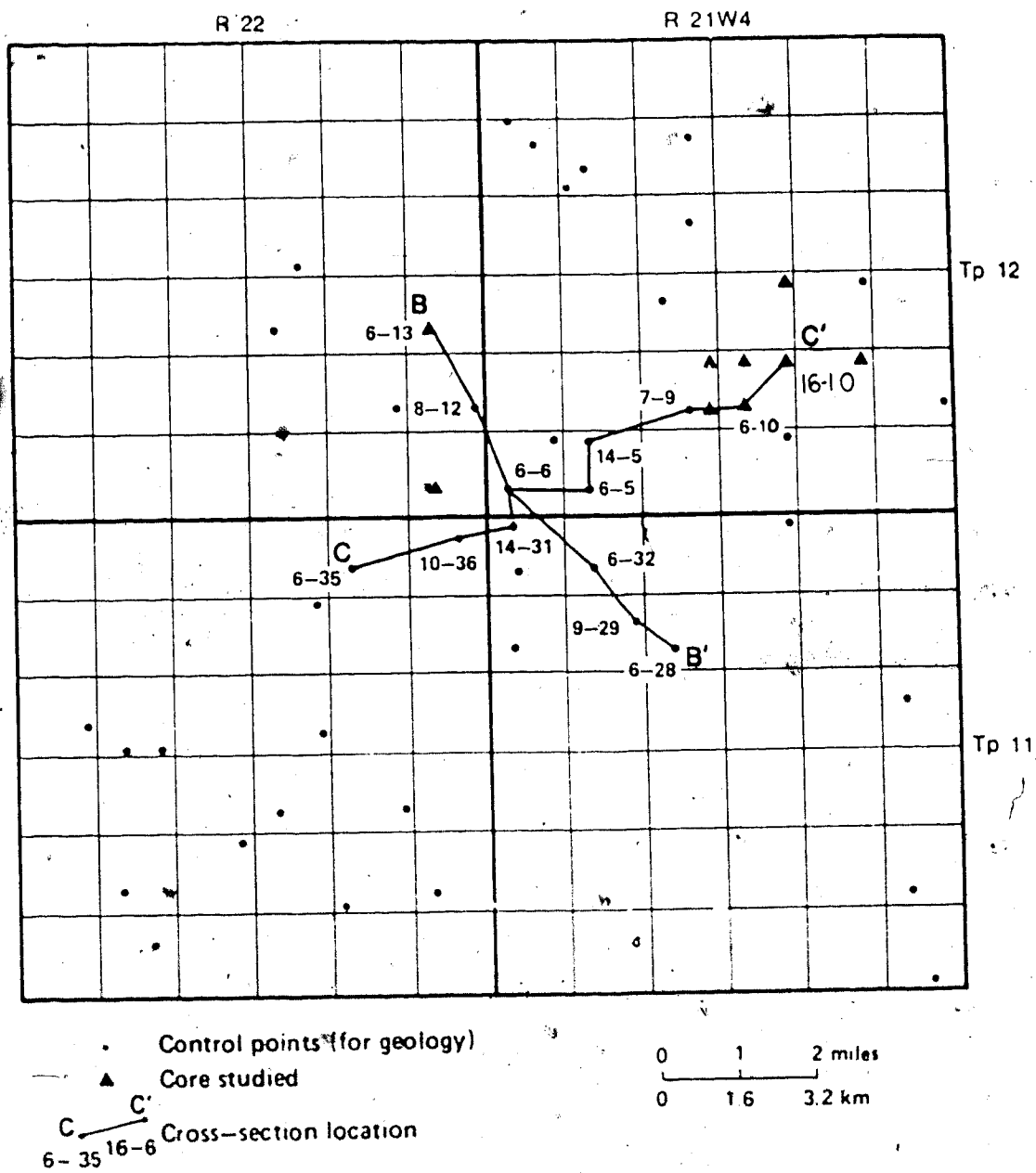


Figure 4.8 Keho Lake study area location map

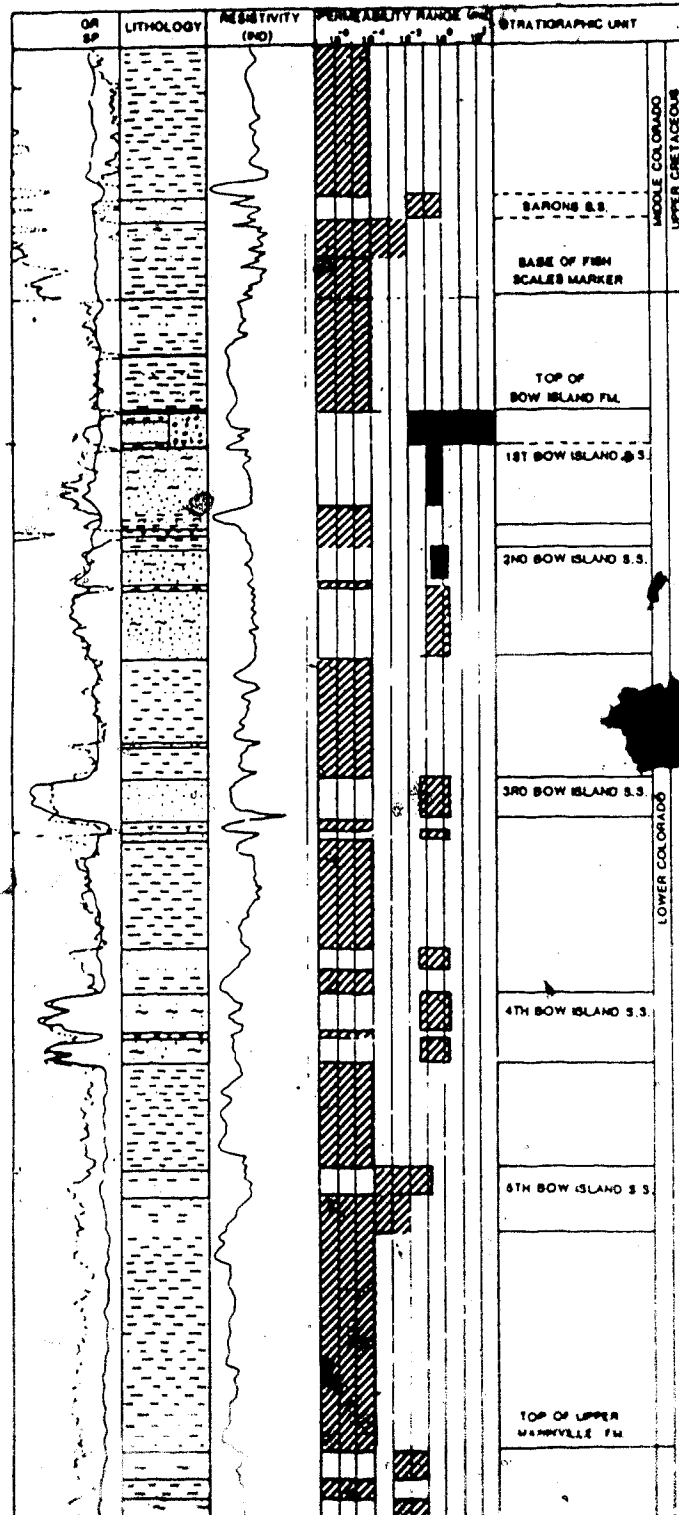


Figure 4.9 Composite strip log through Keho Lake area. of average permeability range, typical geology with corresponding gamma-ray, spontaneous potential and resistivity log responses. The cross-hatched and solid areas are estimated and observed permeability ranges, respectively.

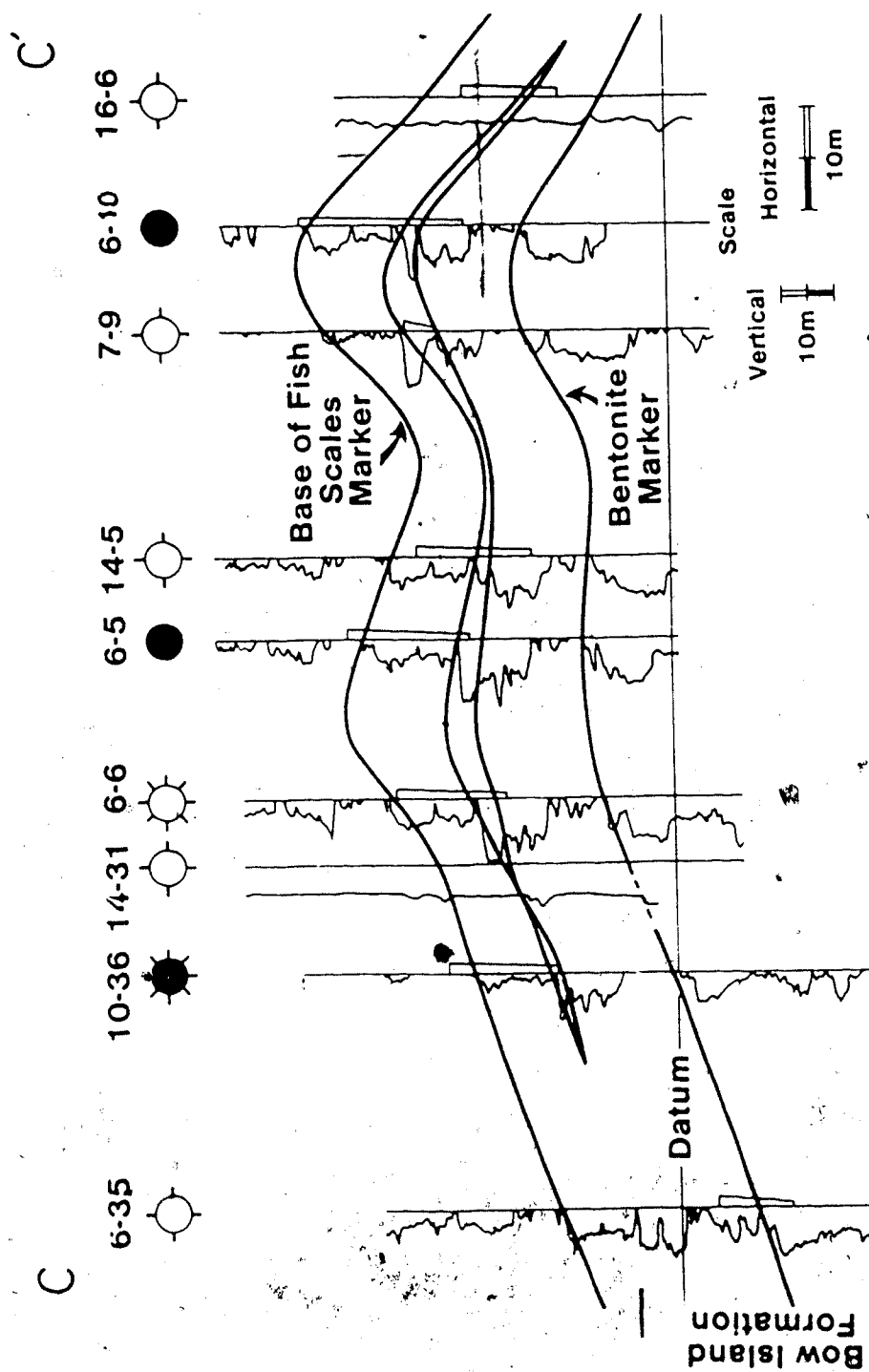


Figure 4.11 Structural cross-section C-C', the correlations are based on gamma-ray logs, see

Figure 4.8 for location.

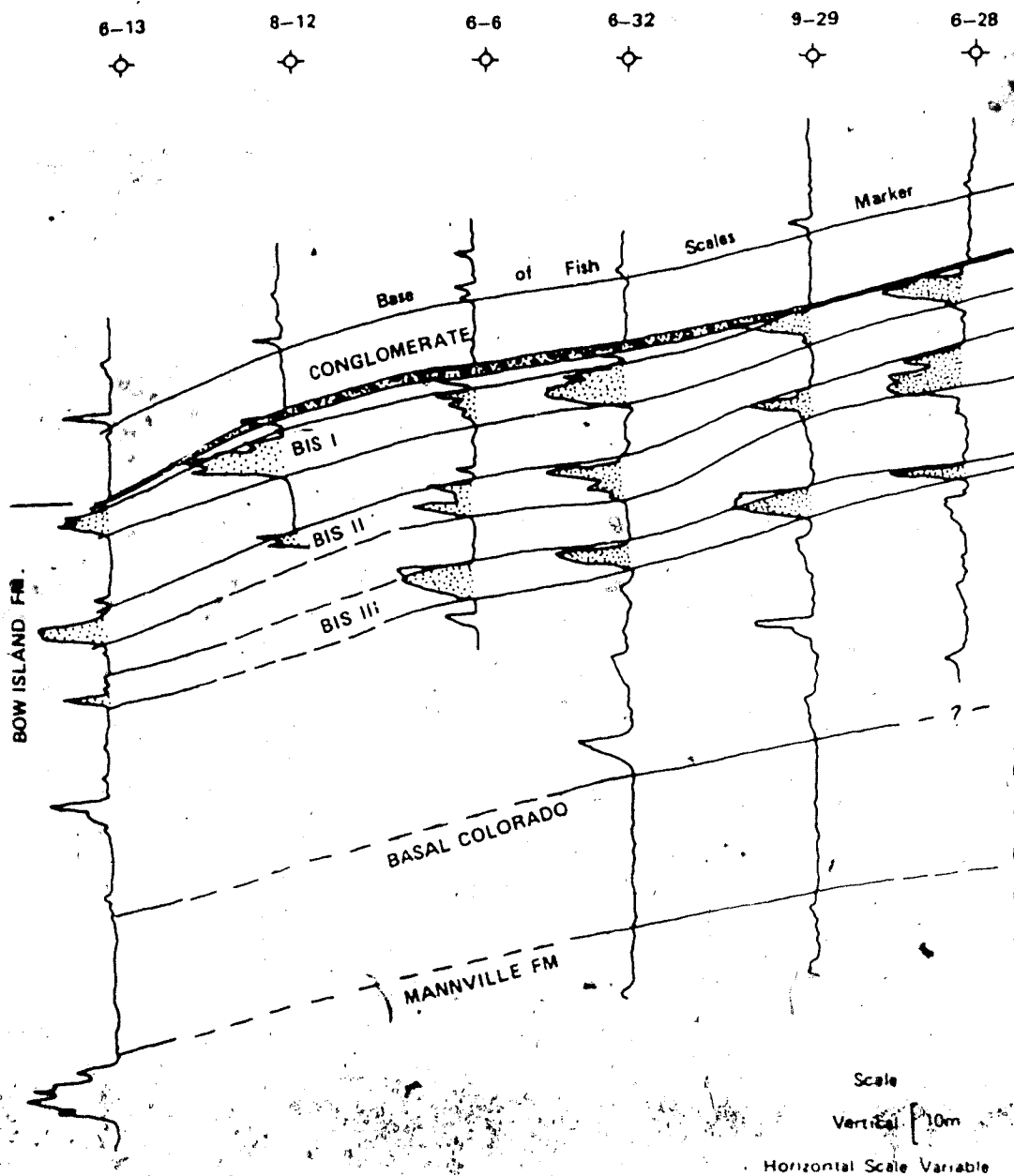


Figure 4.10 Structural cross-section B-B', the correlations are based on gamma-ray logs, see Figure 4.8 for location.



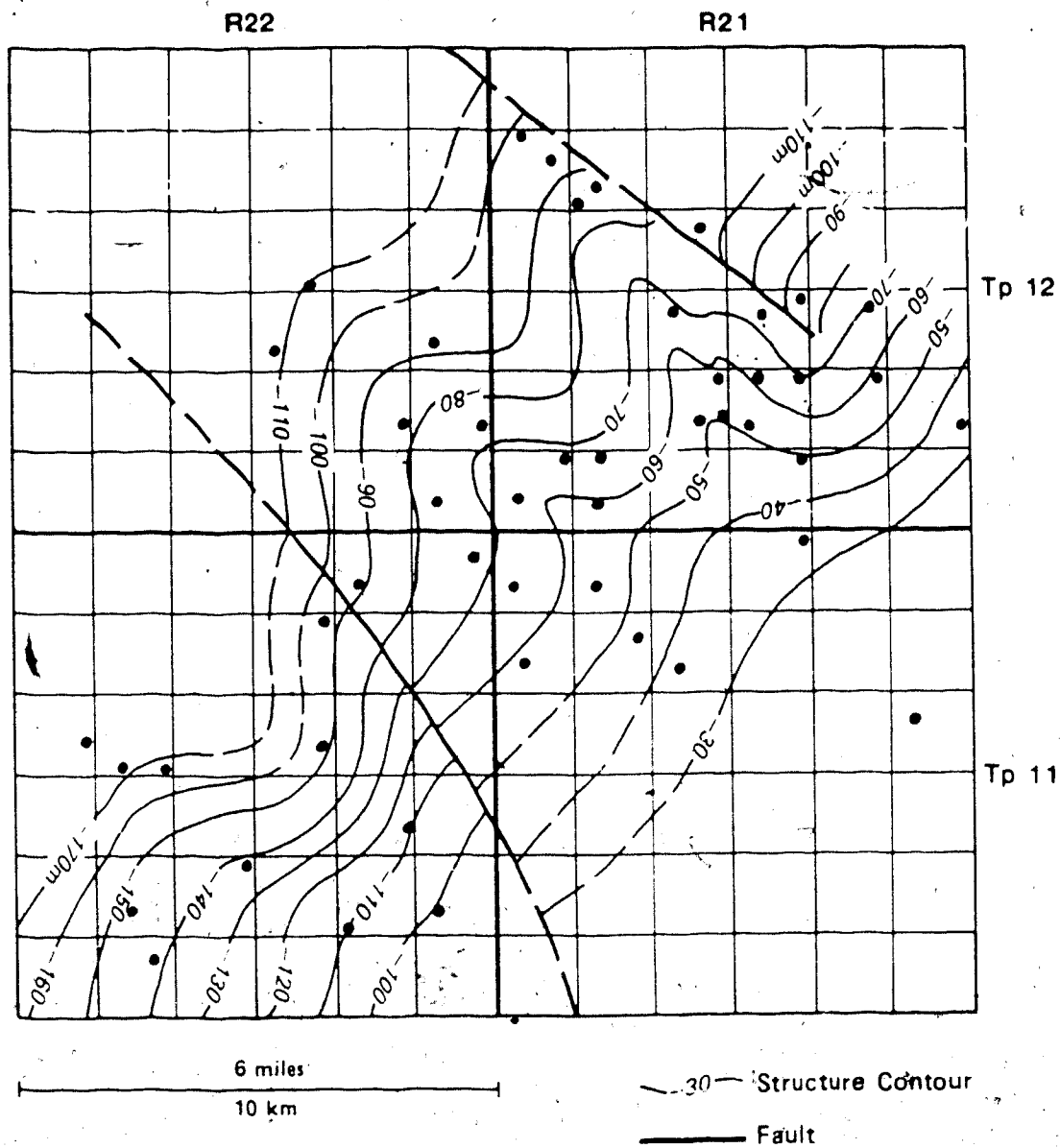


Figure 4.12 Structural contours relative to sea-level on top of the Bow Island Formation, elevations obtained from borehole logs.

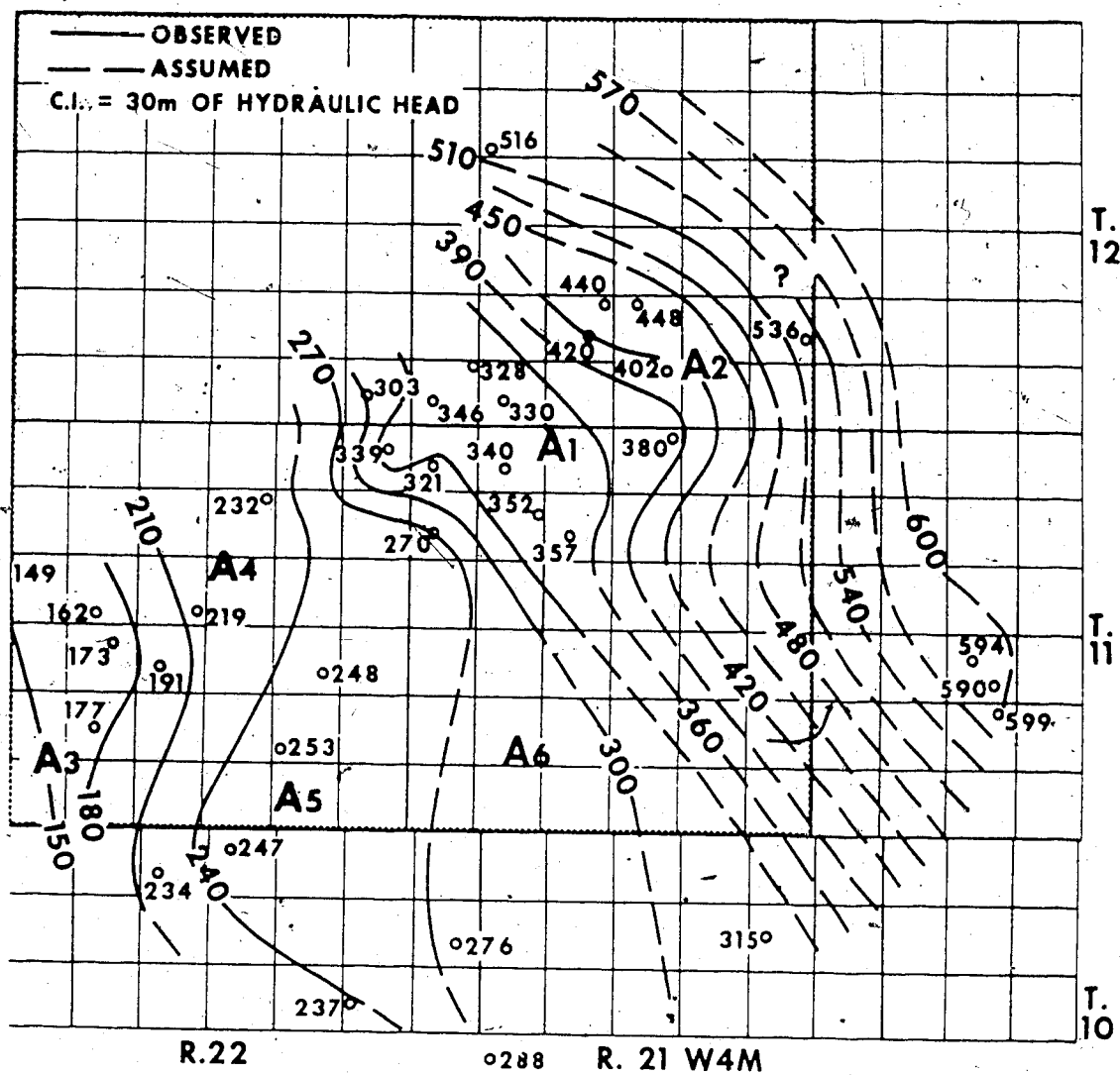


Figure 4.13 Observed potentiometric surface, top of the BIS 1 sandstone, squares represent values influenced by production induced drawdown.

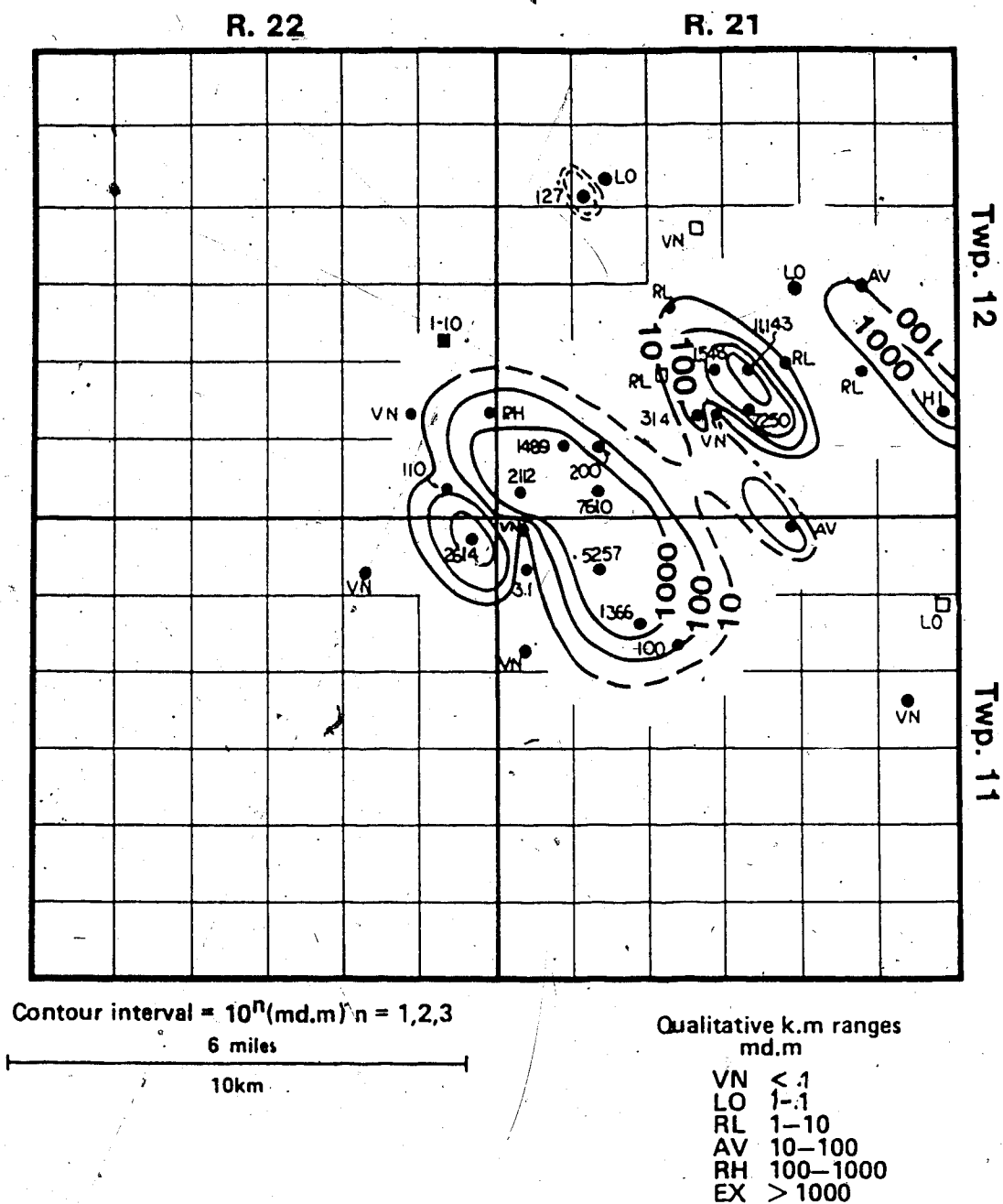


Figure 4.14 Interval permeability distribution for the BIS 1 sandstone and conglomerate. Solid data points are permeabilities calculated and estimated from DST's, solid squares and squares are core derived and estimated permeabilities from lithology as correlated to borehole logs.

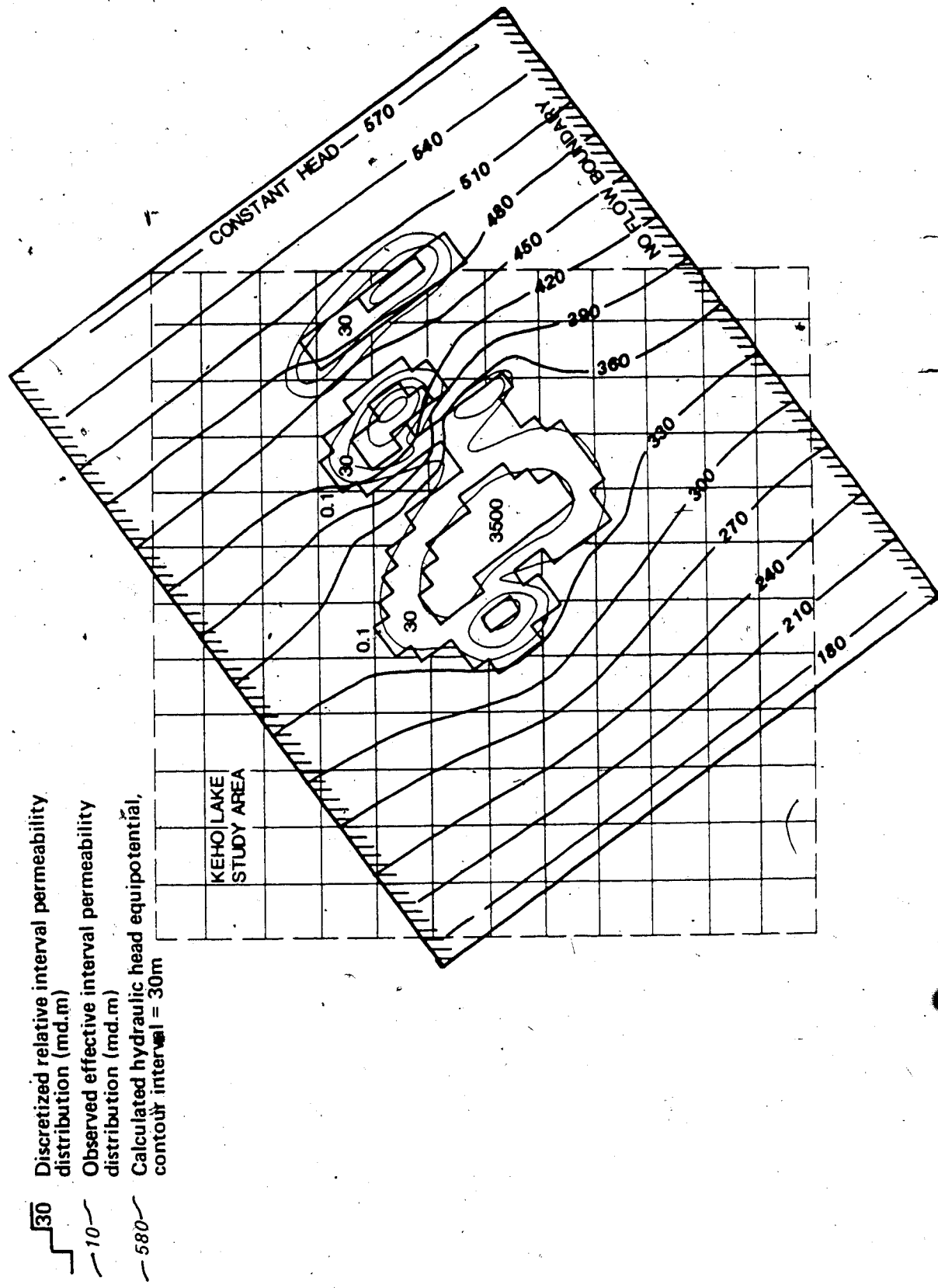


Figure 4.15 Discretized model of the Keho Lake study area (using the interval permeability distribution of Figure 4.14) and the calculated potentiometric surface.

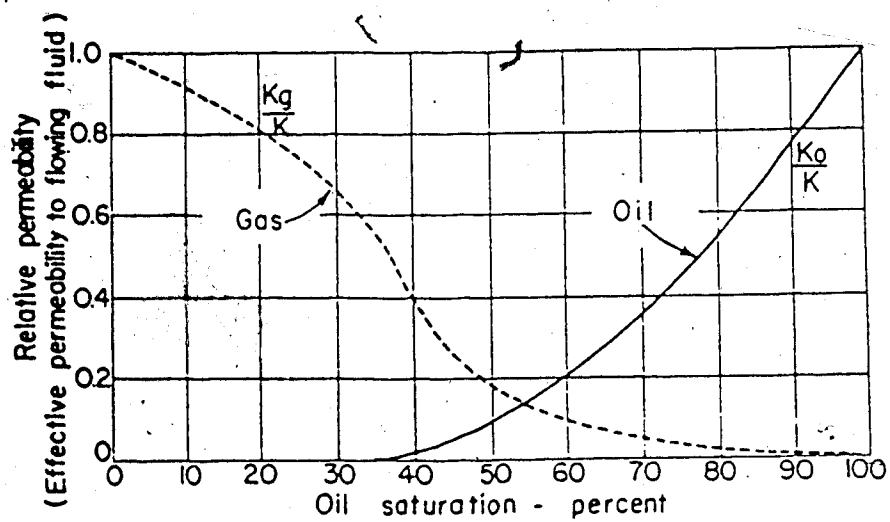
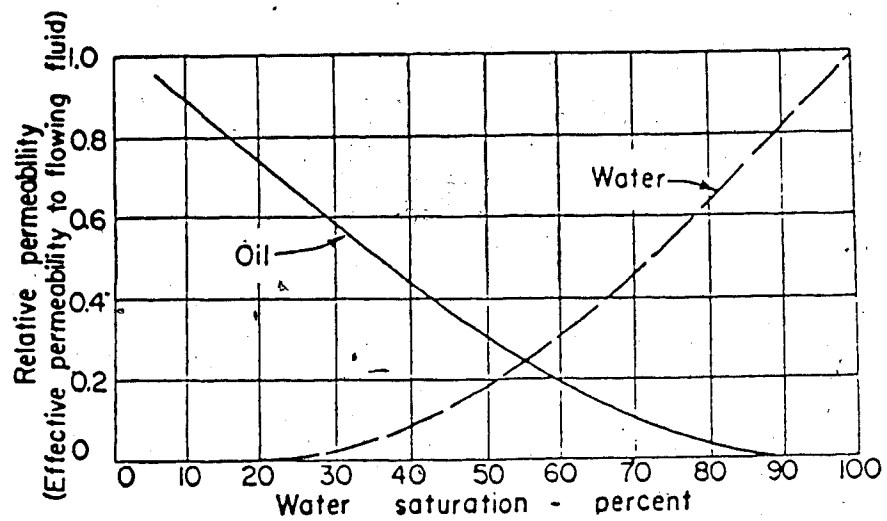


Figure 4.16 Relative permeability relations of fluids to varying saturations, adapted from Golubev, 1959.

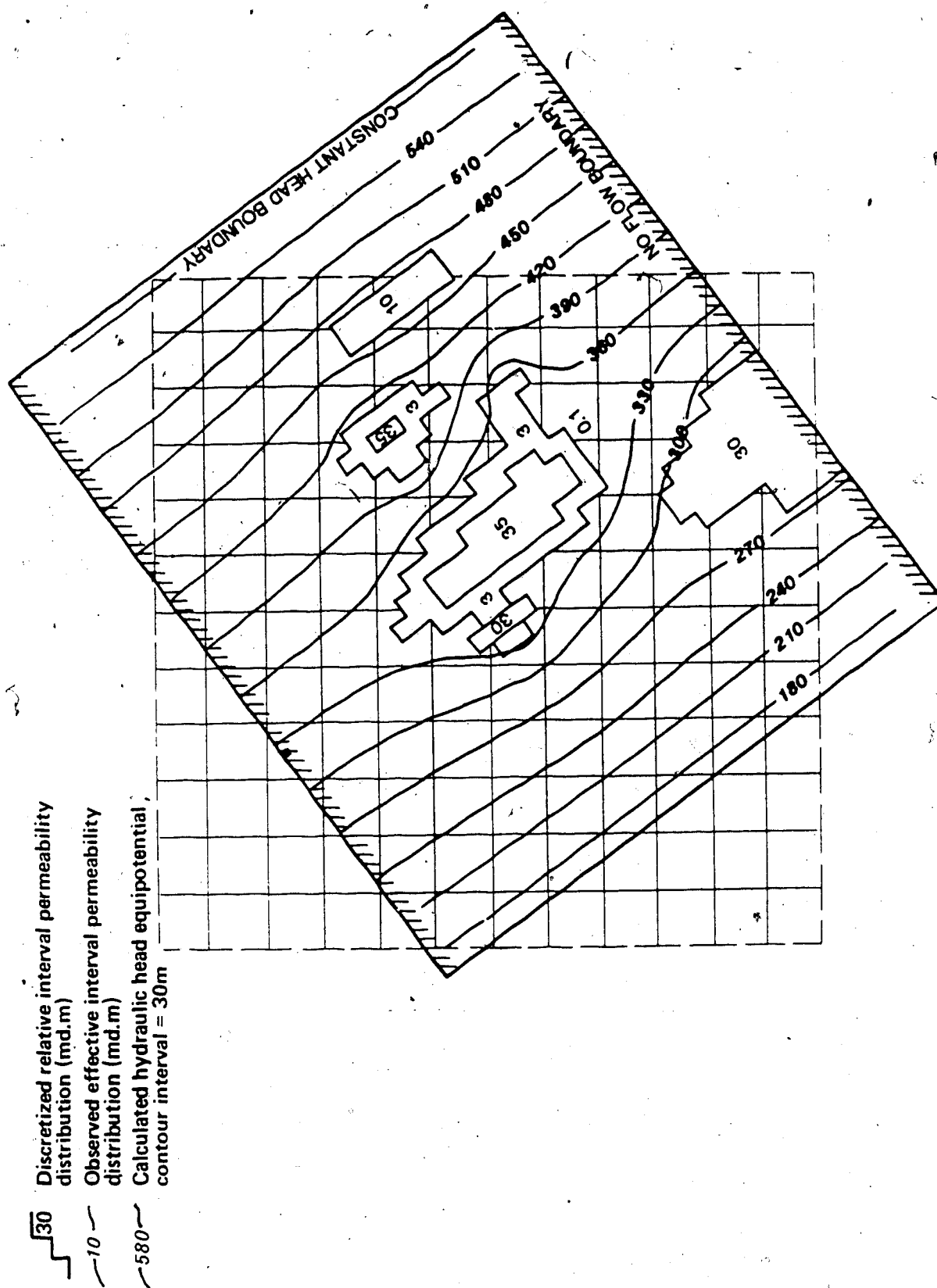


Figure 4.17 Calculated potentiometric surface based on the inferred permeability distribution.

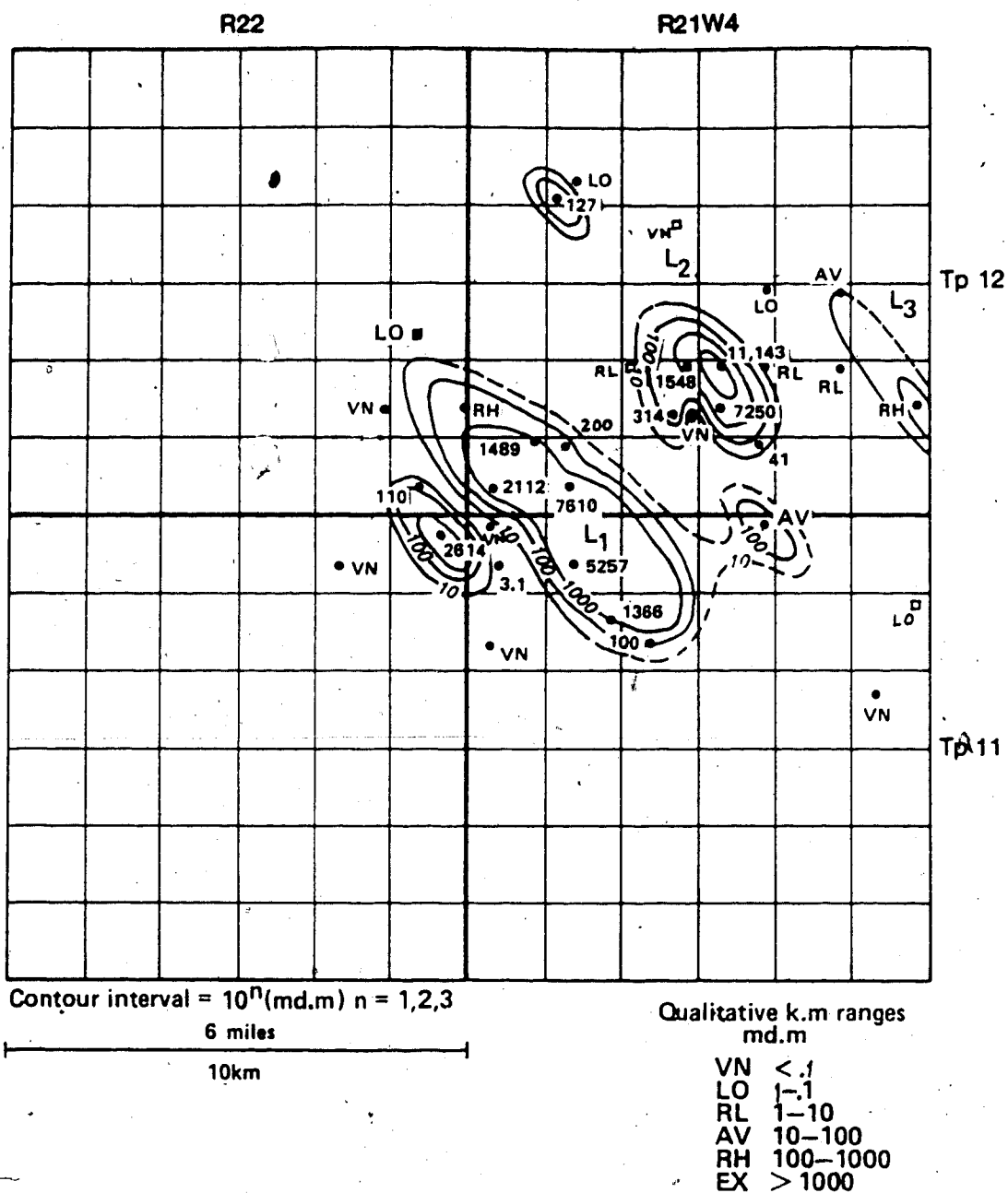


Figure 4.18 Inferred permeability distribution after three iterations adjusting the interpretation of the observed permeability distribution... the trial and error method of "inverse modelling."

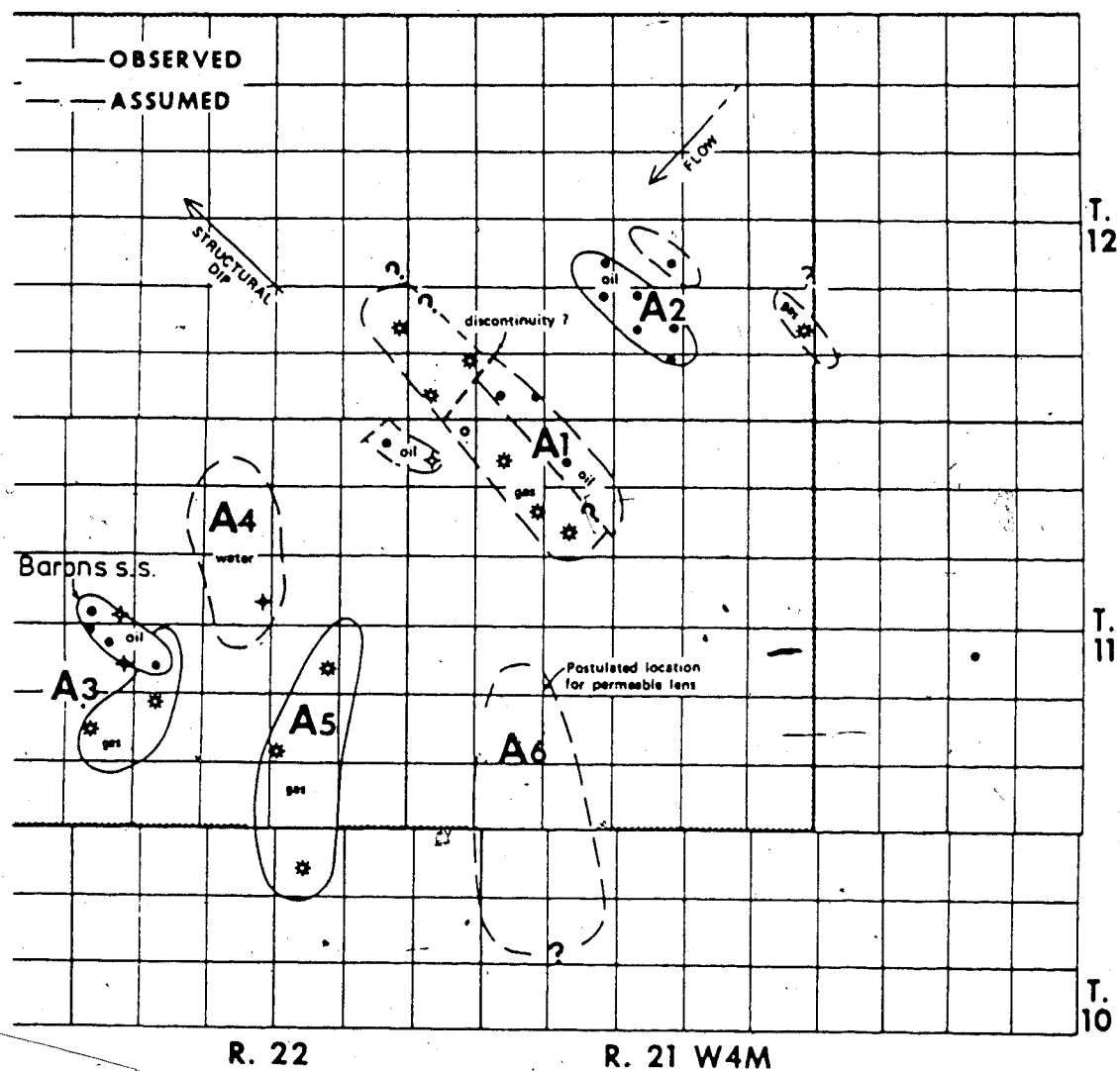


Figure 4.19 Fluid distribution and apparent contact relationships within the study area. Pool outlines at A<sub>1,2,3</sub> were obtained from the E.R.C.B. Oil and Gas Pools Map, 1981, and only represent the locations of established hydrocarbon reserves, not the actual reservoir boundaries. Locations A<sub>4,5,6</sub> are based on hydrocarbon distribution defined during the present study.



#### 4.6 CHIN LAKES STUDY AREA

The Chin Lakes study area was selected on the basis of several anomalous features of the Bow Island Formations potentiometric surface, (Figure 4.6), most of which are associated with the steep flexure in the hydraulic gradient discussed in section 4.4. The study area is located within Townships 8-9 and Ranges 17-18W4M.

##### 4.6.1 Geology

To determine the cause(s) of the observed potentiometric surface anomalies, 61 geophysical logs and 4 cores were examined, Figure 4.20. The geological study produced several cross-sections through the area, two of which, sections D-D' and E-E' are presented in Figures 4.21 and 4.22 respectively. The sections are constructed with gamma-ray logs using the Base of Fish Scales, top of the Bow Island Formation, and the bottom of the second Bow Island sandstone as correlation markers.

The cross-sections demonstrate that the 1st Bow Island sands (BIS 1), which are interbedded with shales on the flanks of the major sand accumulations are subject to rapid lateral changes in thickness. Undulations of the correlation lines may indicate either the paleo-relief of the depositional surface or subsequent folding. Structural contours on the top of the Bow Island Formation (Figure 4.23), indicate a dominantly south-east to north-west dip and the occurrence of a structural high (ridge ?) with a maximum of 25m ( $\approx 85'$ ) of relief. The structural high is underlain by fine to medium grained, clean quartzose (occasionally glauconitic) sandstone, which is topped by a thin chert pebble conglomerate bed on its south-west flank. A composite strip log from the top of the Base of Fish Scales to the top of the Mannville Formation, of lithology, gamma-ray log response and permeability range is given in Figure 4.24. A list of the cores logged in the area is given in Table 4.3, the logs are contained in Appendix 4B.2.

#### 4.6.2 Detailed Potentiometric Surface

The regional potentiometric surface map (Figure 4.6) used in the selection of the Chin Lakes site originally did not discriminate between hydraulic head values obtained from the BIS 1 and BIS 2 sandstones. The 28 hydraulic head values used in the construction of the detailed potentiometric surface (Figure 4.25) are based only on DST's conducted over the BIS 1 unit. To determine the effects of production induced drawdown, cumulative production data to 1984 were obtained from the E.R.C.B. Figure 4.26 shows the production history of the area and includes the DST date, cumulative production and date that the well went on line. Production from the BIS 1 reservoir in Township 8, Range 17W4 began in 1976 with initial hydraulic heads of 565m (1850ft.) to 587m (1923ft.). Much of the DST data used predates this production, or was obtained very soon after production began, or else the tested intervals were out of the permeable zone ( $< 10\text{md.m}$ ) and apparently not affected by drawdown. The two suspect points are at 5-30-8-17W4, and 16-31-8-17W4 which were drilled in 1980 and 1983 respectively. Both the boreholes have yielded anomalously low hydraulic heads 553m (1816ft.) and 505m (1656 ft.) respectively, and are not weighted heavily in the contouring.

The detailed potentiometric surface (Figure 4.25) shows a much reduced hydraulic gradient downstream of a south-east to north-west trending flexure of the equipotentials. The sites of anomalously reduced hydraulic gradient have been designated A<sub>1</sub>, A<sub>2</sub>, A<sub>3</sub>, A<sub>4</sub>. The anomaly A<sub>1</sub> is poorly defined due to the lack of control in its vicinity and only postulated. One of the unknown factors in this study is the effect of the underlying BIS 2 sands on the BIS 1 potentiometric surface. A working assumption is that the BIS 2 sand would have little influence, since it is generally one order of magnitude less permeable, considerably smaller in areal extent and is separated from the BIS 1 by approximately 5 metres of shale of very low vertical conductivity that would tend to retard any interference effects.

#### 4.6.3 Permeability Distribution

The interval permeability distribution of the 1st Bow Island sandstone unit (Figure 4.27), is based on effective permeability-determinations from drill stem tests, where these

were unavailable, core determined permeability and lithology estimation from log response was used to assign a permeability range. The measured permeability range is from 3823 md to 1.9 md for the conglomerates and sandstones, whereas the surrounding silt-shale matrix (as determined from core or geophysical logs) have been assigned a permeability of  $< 1$  md.

The interval permeability distribution map (Figure 4.27) outlines a narrow, elongate north-west to south-east trending body, designated as ( $L_1$ ), with a north-easterly spur ( $L_2$ ) in its approximate center. To the north-east of the study area is a lenticular sand body ( $L_3$ ), which is poorly defined due to a lack of control. The north-westerly extension of  $L_1$  has been designated as  $L_4$  and a small north-west south-east trending lens in the south-west of the study area is designated  $L_5$ . To the south-west of the main permeable trend is a sheet like body ( $S_1$ ) of relatively low permeability.

Underlying the BIS 1 unit are thin ( $\approx 5$ m) discontinuous sandstone beds (see cross sections D-D' and E-E', Figures 4.21 and 4.22) with maximum attained permeabilities of  $\approx 234$ md (range 0.5-234, average  $\approx 50$ ). The BIS 2 sands are separated by approximately 5 to 10m of shale whose horizontal and vertical permeabilities are estimated to be  $< 0.1$ md and  $< 0.05$ md respectively. Due to a lack of control it was not possible to construct a detailed permeability distribution map for the BIS 2 sandstone, however, the approximate permeability of this unit is indicated on the cross-sections in Figures 4.21 and 4.22.

Inspection of Figures 4.25 and 4.27 shows that a general correlation clearly exists between the areas of poor permeability and steep hydraulic gradients and the anomalous areas of high permeability and low hydraulic gradients.

#### 4.6.4 Verification of Anomaly by Numerical Simulation

To verify the observed potentiometric surface (Figure 4.25) a numerical model was constructed for the Chin Lake study by discretizing the observed permeability distribution and regional boundary conditions (Figure 4.28). The observed effective permeability ( $k_e$ ) at  $L_1$  (Figure 4.27) was adjusted for an average gas saturation of 55%, yielding a  $k_r \approx 0.1 \cdot k_e$ , using the relationship given in Figure 4.16. Inverse modelling was not necessary in the Chin

Lakes area, since the relatively good data distribution allowed a satisfactory interpretation of the permeability distribution.

Comparison of the calculated and observed potentiometric surfaces (Figures 4.25 and 4.28) shows a drop in hydraulic head of 90m versus 60m at the upstream end, and 120m versus 30m at the downstream end, respectively of the main permeable trend ( $L_{1,2,3}$  of Figure 4.26). This asymmetry indicates that the actual flow system through the modelled area is probably not at steady-state. The effect is most likely related to the dilational rebound of the Colorado Group due to the erosional modification of the topography (Tóth and Corbet, 1986), the simulation of which requires the use of a transient flow model, and a detailed knowledge of the changing boundary conditions. Overall, however, the observed anomalies of the potentiometric surface (Figure 4.25) are reproduced by the model (Figure 4.28), verifying the original interpretation.

#### 4.6.5 Fluid Distribution

The fluid distribution within the upper Bow Island formation of the Chin Lake study area is given in Figure 4.29. The only major hydrocarbon accumulation occurs at  $A_1$  ( $L_1$  on Figure 4.27) which produces gas from the top of the 1st Bow Island sandstone. The gas appears to be trapped by an updip stratigraphic-pinchout of the reservoir bed (in the south-east) and in part by structural closure further to the north-west.

Locations  $A_1$ ,  $A_2$  and  $A_4$  are all water bearing sandstones. Several scattered and minor accumulations of gas occur in underlying BIS 2 and BIS 3 zones, and a small gas accumulation (in the south-west) occurs at  $A_3$ . The fluid contact relationship observed at  $L_1$  suggests that the gas/water contact is influenced by hydrodynamic flow conditions (indicated by a possible downflow shift of the gas/water contact) at its north-east boundary, as well as structural control. However, as in the Kehoe Lake study tilted hydrocarbon/water contacts are not discernible due to the thin reservoir beds and predominant effect of structural dip.

Table 4.3 Intervals and locations of cores logged in the Chin Lakes study area.

LOCATION	INTERVAL (m)	FORMATION
11-30-8-17W4	708.5-730.5	BFSC-BIS
11-7-8-18W4	782-791.7	BIS
10-19-8-18W4	800.3-811.3	BIS
7-10-9-18W4	696.6-701.5	BFSC-BIS
	733.2-743.0	BIS

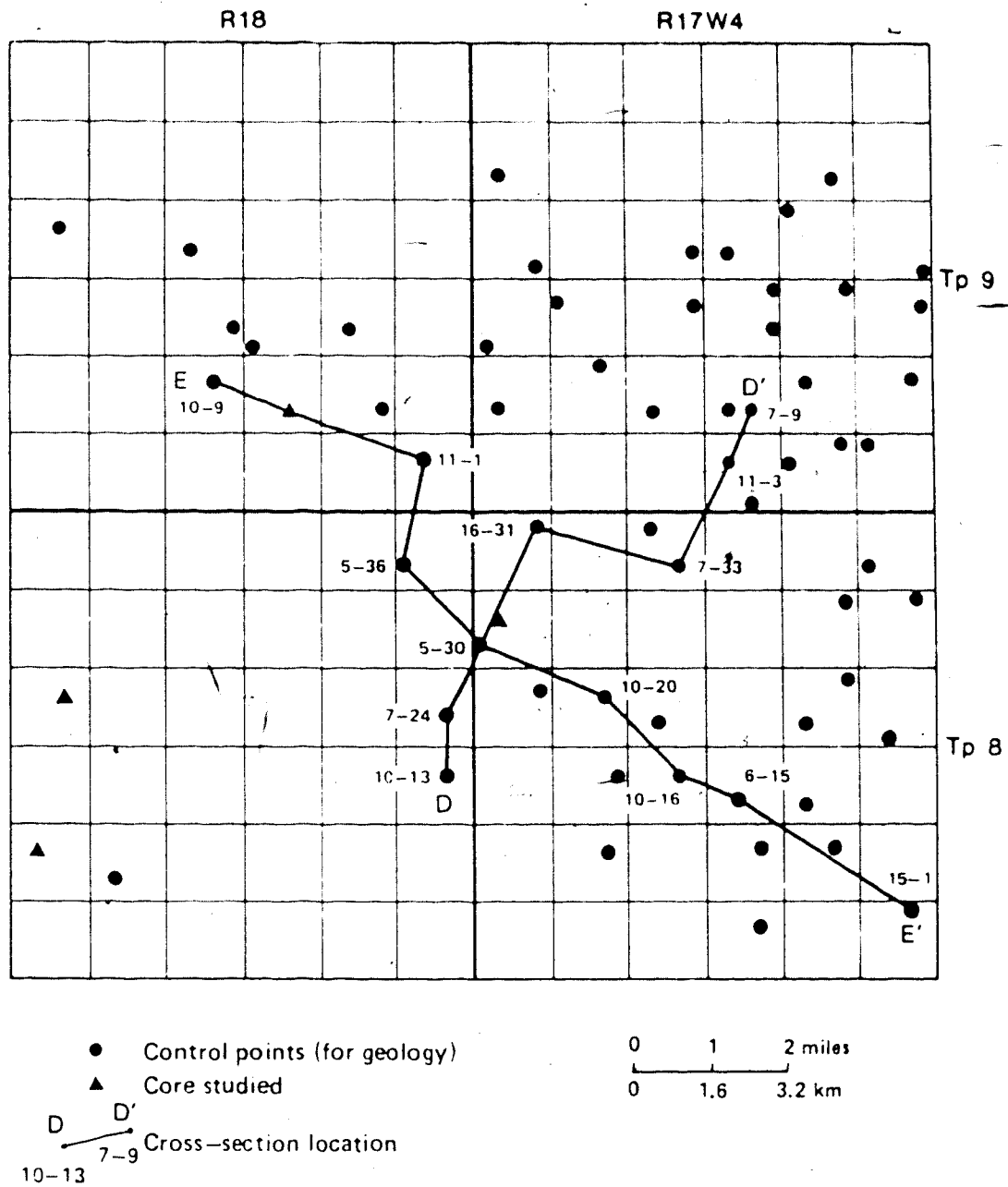


Figure 4.20 Location map of Chin Lakes study area.

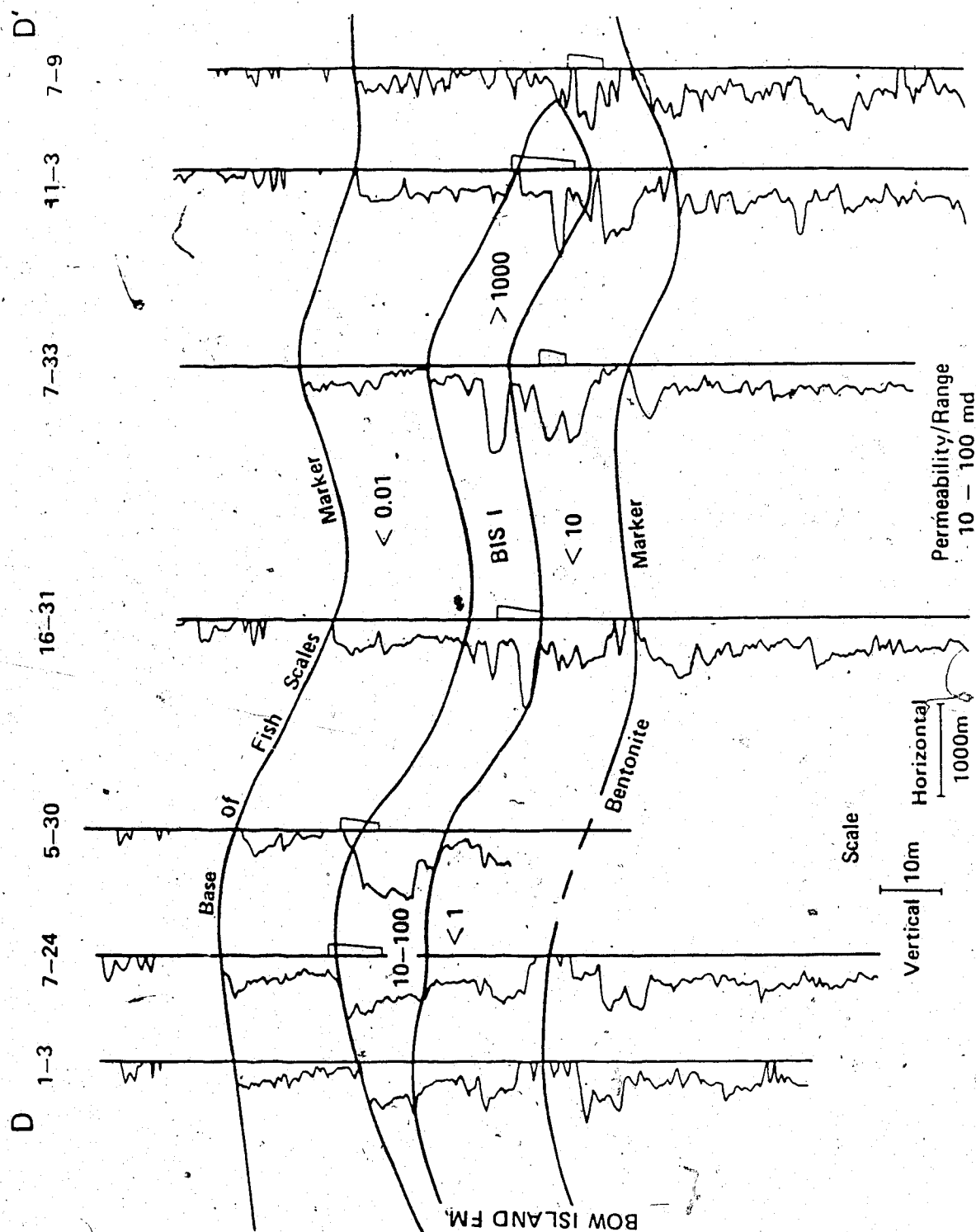


Figure 4.21 Structural Cross-Section D-D' (see Figure 4.20 for location), correlations are based on gamma-ray log response.

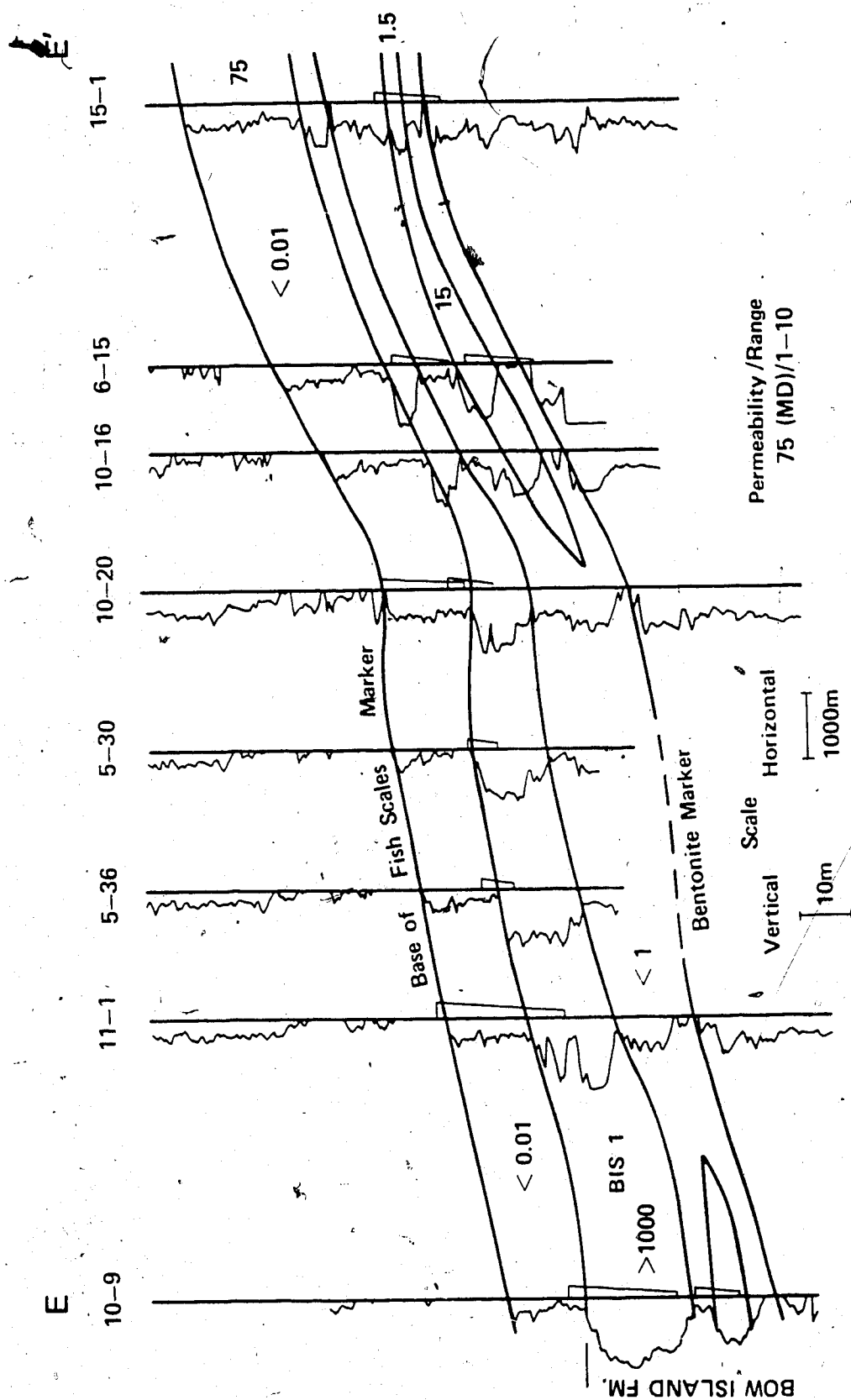


Figure 4.22 Structural Cross-Section E-E' (see Figure 4.20 for location). correlations are based on gamma-ray log response.



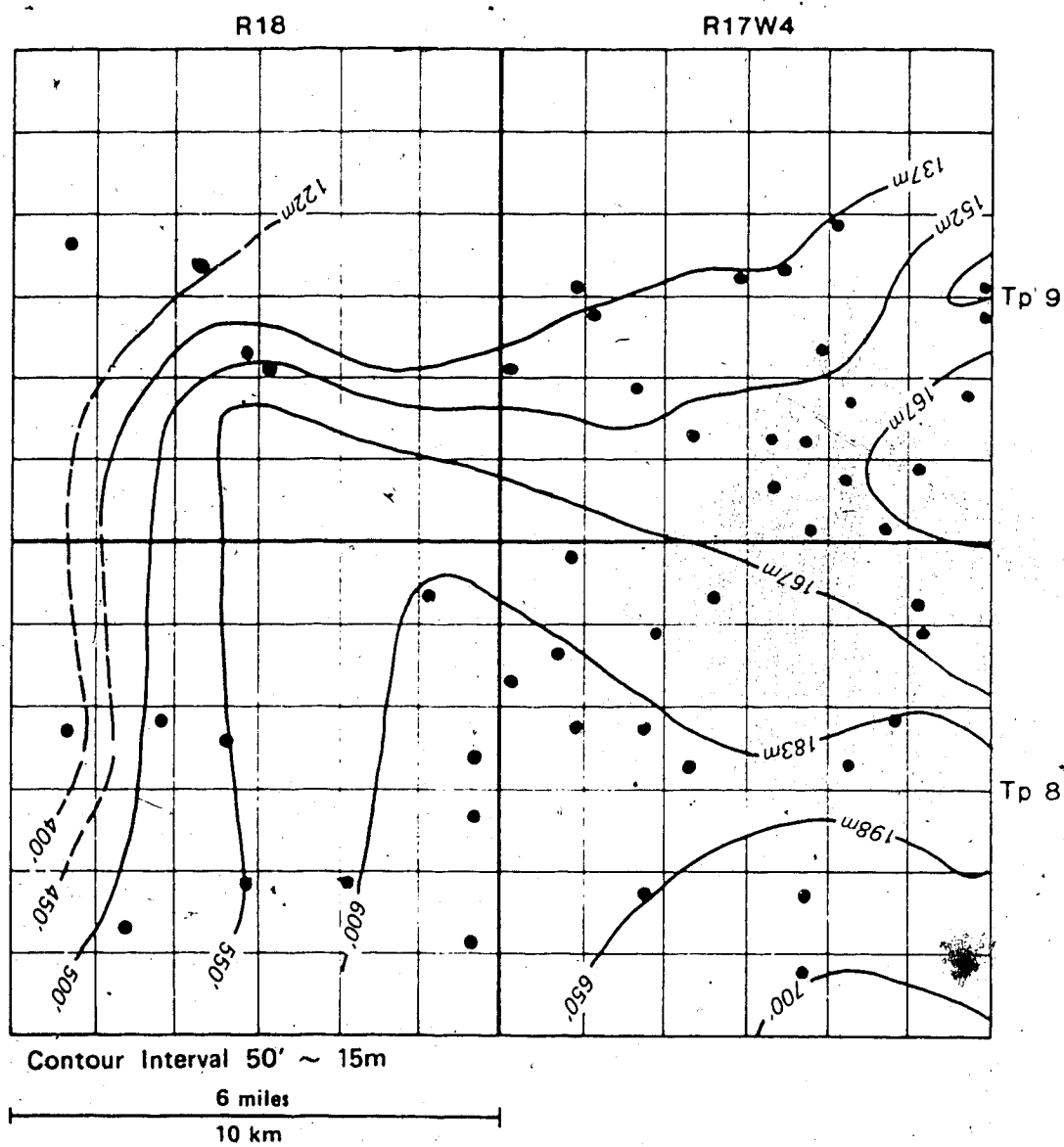


Figure 4.23 Structural contours relative to sea level on top of the Bow Island Formation, elevations were determined from borehole logs.

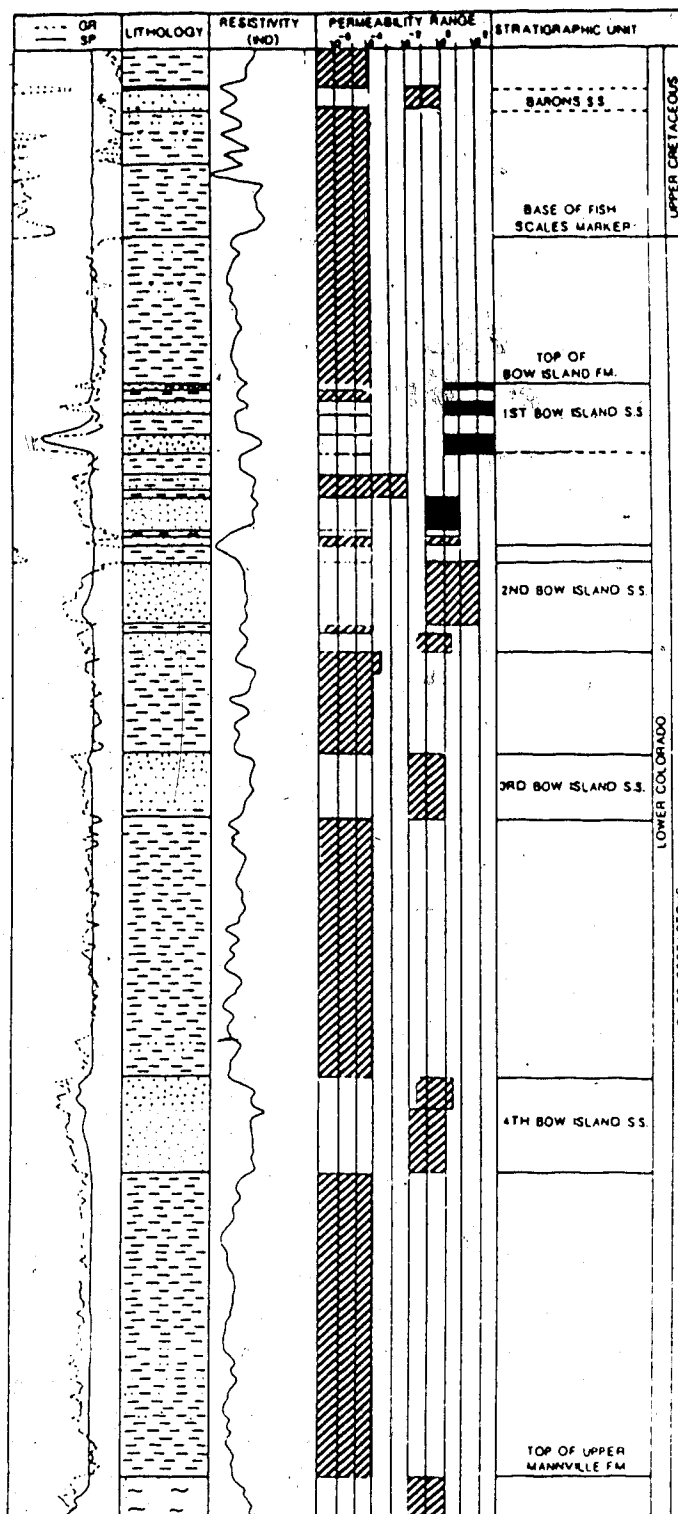


Figure 4.24 Composite strip log of the Chin Lakes study area indicating typical permeability range and lithology with corresponding gamma-ray, spontaneous-potential and resistivity log responses. The cross-hachured and solid areas represent estimated and observed permeability ranges, respectively.

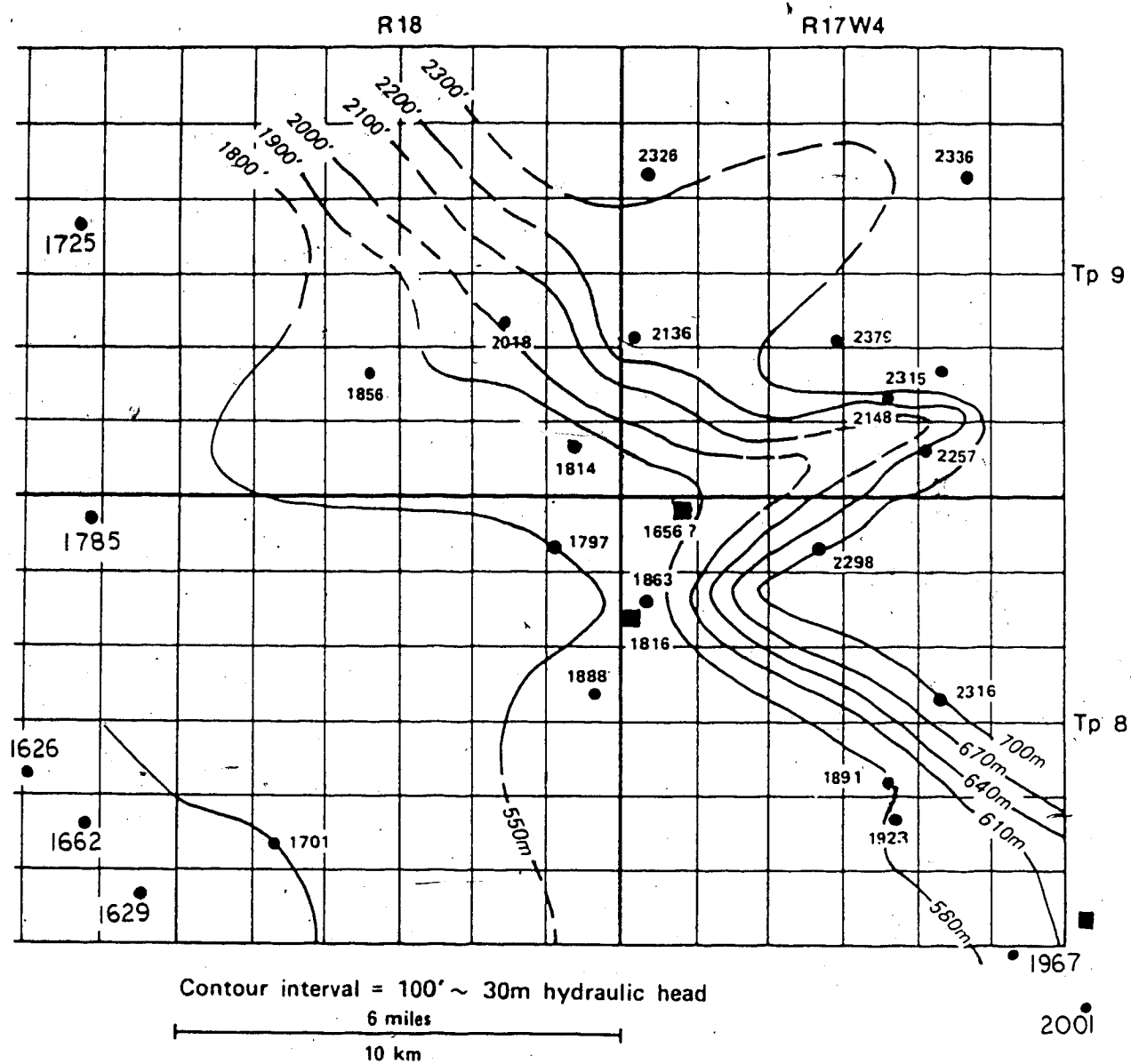


Figure 4.25 Detailed potentiometric surface distribution for the upper BIS 1 sandstone, squares designate values influenced by production induced drawdown.

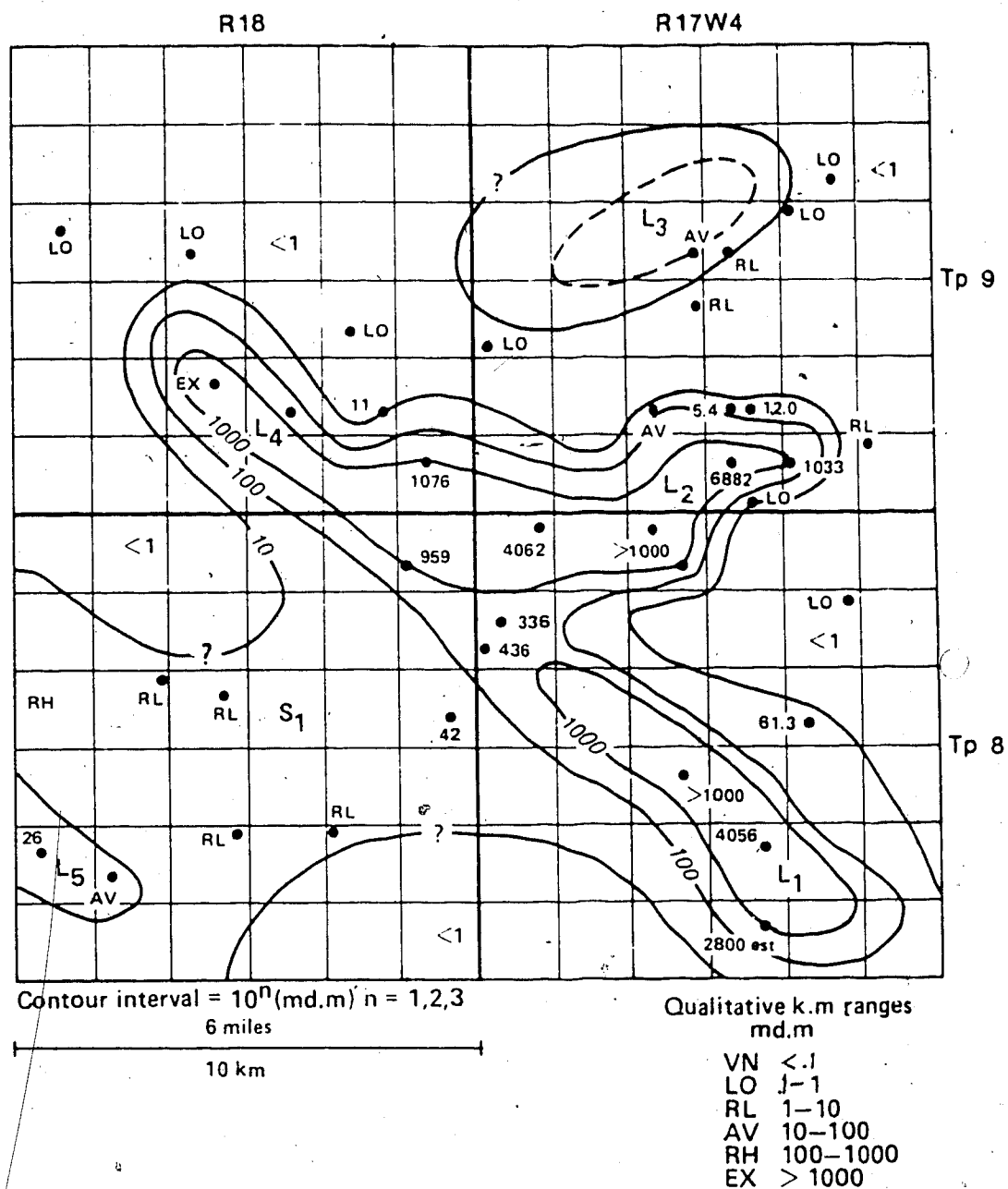


Figure 4.26 Interval permeability distribution for the BIS 1 sandstone and conglomerate. Solid data points are permeabilities calculated (numbers) and estimated (qualitative range). The designations  $L_1, L_2, L_3, \dots$  and  $S_1$  are for the main permeable trends defined in the area.

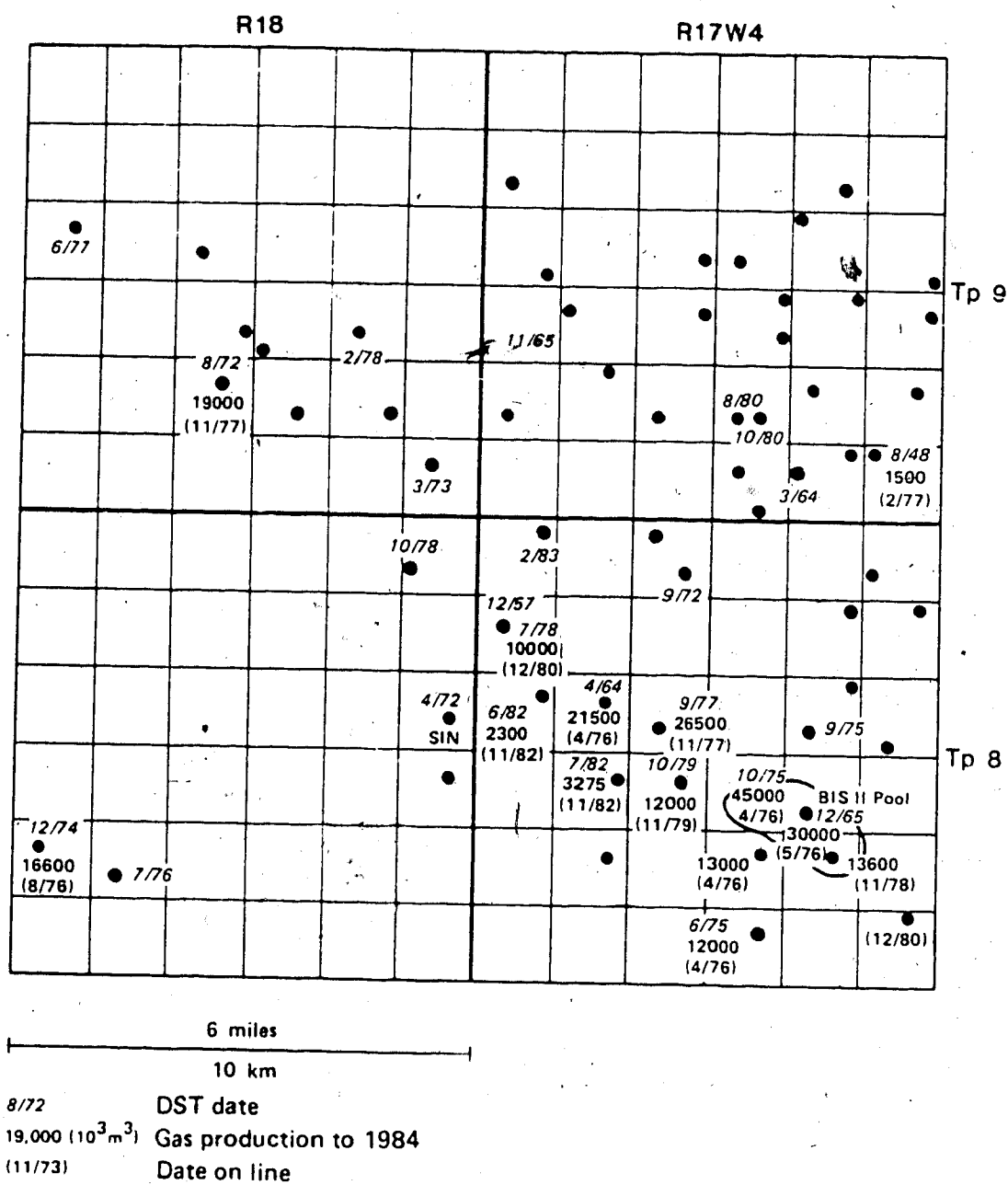


Figure 4.27 Production history (from the E.R.C.B. of Alberta), indicating the DST date, cumulative production if any, and date production started.

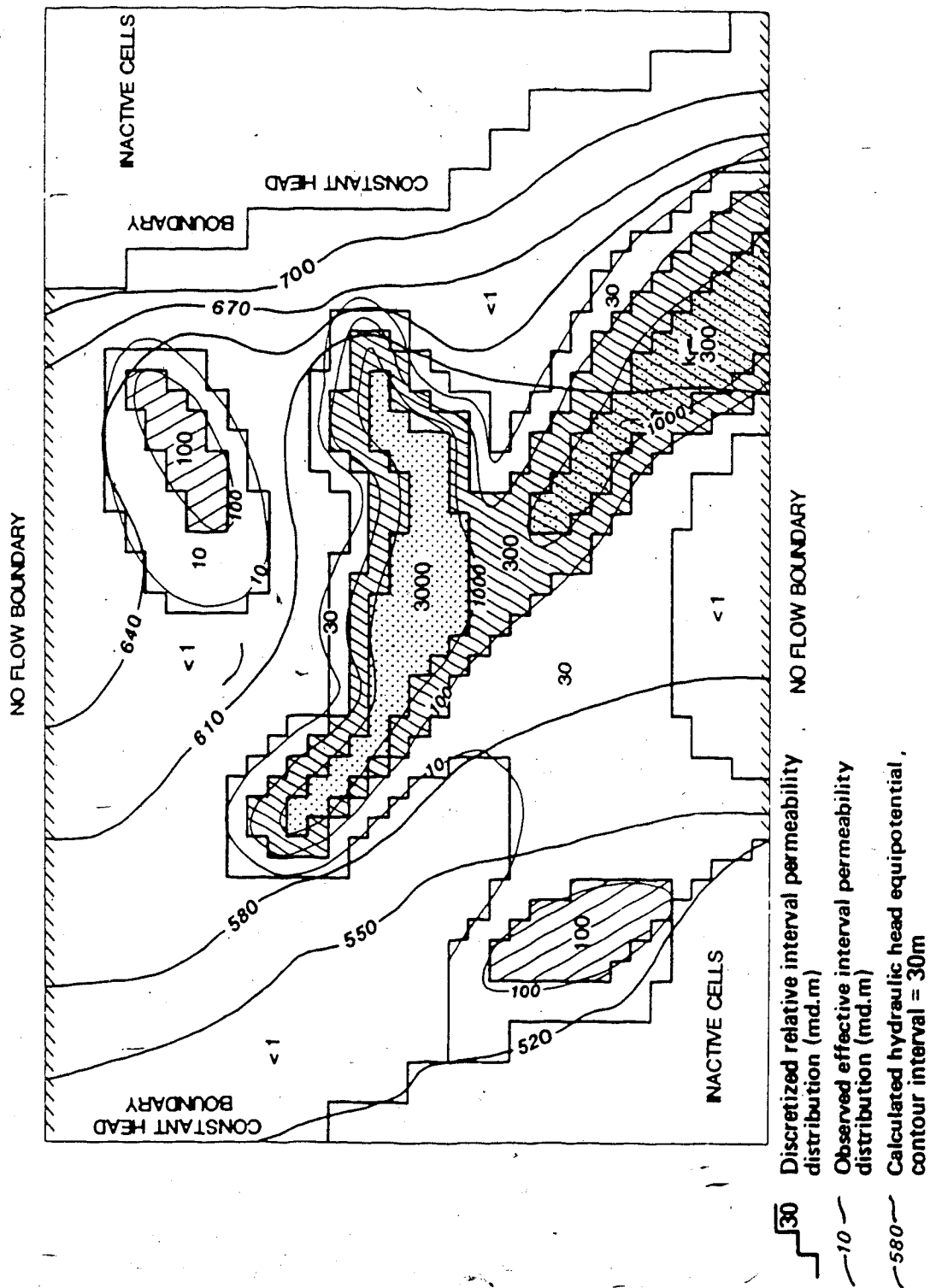


Figure 4.28 Discretized model of Chin Lakes study area using relative permeability to water flow and the calculated potentiometric surface distribution.

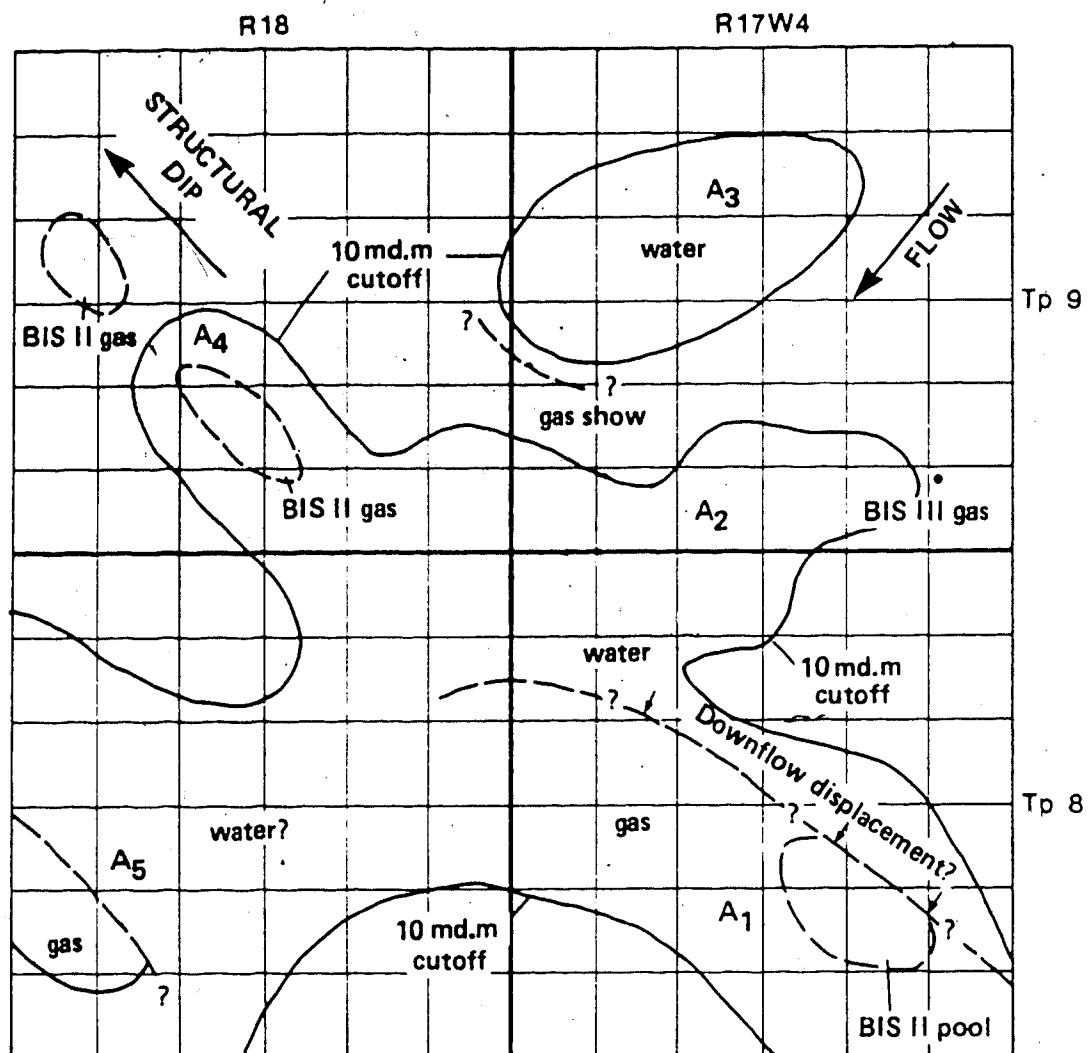


Figure 4.29 Fluid distribution and apparent contact relationships observed in the Chin Lakes study area. Designations A<sub>1</sub>, A<sub>2</sub>, A<sub>3</sub>, A<sub>4</sub>, A<sub>5</sub> refer to areas that have corresponding potentiometric surface anomalies. Reservoir outlines shown are based on E.R.C.B. Oil and Gas Pool Maps (1981).

## CONCLUSIONS AND DISCUSSION

Fluid-flow through highly permeable rock bodies (lenses), encased in a relatively less permeable matrix can be described by the groundwater-flow equation. Theoretically, the presence of a relatively permeable body within a fluid-potential field, causes a negative anomaly to develop at its upstream extremity, with little change in potential across the body and a positive anomaly at its downstream end. The magnitude and areal extent of an anomaly are controlled by :

1. the regional fluid-potential (or hydraulic-head) gradient, which is directly proportional to the magnitude of the anomaly;
2. the permeability contrast between the lens and surrounding matrix, up to a threshold ( $\epsilon_t$ ), above which the magnitude of the anomaly remains constant;
3. the geometry of the permeable body, circular shapes creating the largest anomalies, which decrease with the elongation of the body parallel to flow.

The vertical extent of an anomaly is reduced when flow occurs through an anisotropic medium ( $k_h > k_v$ ). This effect may disallow the use of potentiometric surface maps constructed for a specific stratigraphic horizon to detect deeper permeable bodies, since any anomaly due to the underlying body will be suppressed in vertical extent. Further work (theoretical, by 3-D modelling and field study) is required to evaluate this hypothesis conclusively.

The field study shows that randomly selected potentiometric anomalies within the Bow Island Formation are associated with the presence of reservoir quality, permeable rock bodies. Potentiometric anomalies created by these reservoirs appear to be relatively limited in vertical extent and well defined laterally along the stratigraphic unit containing them. This suggests that potentiometric surface maps should be constructed for the thinnest defineable horizon for best results, especially in formations containing vertically stacked sand bodies, or areas with a significant vertical hydraulic gradient.

The present potentiometric surface of the Bow Island Formation probably reflects post Eocene erosional modification of the land surface and is currently in a transient,



sub-hydrostatic state. This underpressuring may be partly or completely responsible for the observed hydraulic gradient within the Bow Island Formation. The abundance of hydrocarbon accumulations (especially the lighter fractions) in most of the available pore-space in the upper Bow Island and middle Colorado sandstones is probably a result of this potential minimum, which favours hydrocarbon exsolution from transporting fluids. Consequently, the Bow Island Formation and its stratigraphic equivalents represent a very promising interval for the application of the lens associated potentiometric anomaly theory.

The application of the method to the exploration for reservoirs is by an 'inverse' approach. Anomalies which correspond to known fields should be used as models, which are then extrapolated to select and define anomalies that represent potential exploration targets. The method does not replace conventional mapping techniques, but rather supplements them, the advantage gained being the ability to define prospects (such as the Kehoe Lake study, A. anomaly), which have not yet been drilled. The paucity of data in this field study did not allow a rigorous statistical treatment of the observed anomalies and their correlation to theoretical expectation. One of the problems in selecting areas of good data distribution (such as large, well established field areas) is that of production induced drawdown, which may cause false anomalies or depressions of the potentiometric surface. Consequently, further field work is required, preferably in other areas and stratigraphic units to firmly establish the method.

Entrapment of hydrocarbons by isolated lenticular bodies is partially due to mechanical filtration and capillary pressure differentials at the downstream end of the lens. As a result, hydrocarbons will tend to start accumulating at the downstream extremity of a permeable lens with structural dip (which introduces buoyancy potentials) causing a modification of the effect. Therefore, exploratory wells should be located by taking flow direction as well as structural dip into account.

Finally, using the 'inverse method' (by trial and error or automated techniques) to delineate reservoir boundaries and reservoir geometry should improve interpretation of permeability distribution, and hence assist in locating development wells.

## REFERENCES

- Alberta Energy Resources Conservation Board, 1969, Structure contour map of the Base of Fish Scales Marker, Map Area 1, Scale 1:250,000.
- Alberta Energy Resources Conservation Board, 1976, Structure contour map of the Base of Fish Scales Marker, Map Area 2, Scale 1:250,000.
- Amajor, L.C., and J.F. Lerbekmo, 1980, Subsurface correlation of bentonite beds in the lower Cretaceous Viking Formation of south-central Alberta: Bulletin of Canadian Petroleum Geology, vol. 28, no. 2, pp. 149-172.
- Beach, F.K., 1962, Viking-deposition, discussion: Journal of the Alberta Association of Petroleum Geologists, vol. 10, no. 4, pp. 210-212.
- Berry, F.A.F., 1960, Geologic field evidence suggesting membrane properties of shales: American Association of Petroleum Geologists Bulletin, vol. 44, no. 6, pp. 953-954.
- Berry, F.A.F., and B.B. Hanshaw, 1960, Geologic field evidence suggesting membrane properties of shales: Volume of Abstracts, Twenty-First International Geological Congress, Copenhagen, p. 209.
- Boethling, F.C., Jr., 1977a, Viking Sandstone - Alberta (Part I): Oil and Gas Journal, March 21, 1977, pp. 196-200.
- Boethling, F.C., Jr., 1977b, Viking Sandstone - Alberta (Part II): Oil and Gas Journal, March 28, 1977, pp. 173-176.

Brace, W.F., 1980, Permeability of crystalline and argillaceous rocks: International Journal of Rock Mechanics, Mineral Science and Geochemistry, vol. 17, pp. 241-151.

Bradley, J.S., 1975, Abnormal formation pressures: American Association of Petroleum Geologists Bulletin, vol. 59, no. 6, pp. 957-973.

Carslaw, H.S., and J.C. Jaeger, 1959, Conduction of heat in solids: Clarendon Press, Oxford, 510 p.

Cooley, R.L., 1977, A method of estimating parameters and assessing reliability for models of steady-state groundwater flow, 1, Theory and numerical properties: Water Resources Research, vol.13, no.2, pp. 318-324.

Cooley, R.L., 1979, A method of estimating parameters and assessing reliability for models of steady-state groundwater flow, 1, Application of statistical analysis: Water Resources Research, vol.15, no.3, pp. 603-617.

Deroo, G., T.G. Powell, B. Tissot, R.G. McCrossan with contributions by P.A. Hacquebard, 1977, The origin and migration of petroleum in the western Canadian sedimentary basin, Alberta: A geochemical and thermal maturation study: Geological Survey of Canada, Bulletin 262, 136 p.

DeWiel, J.E.F., 1956, Viking and Cardium not turbidity current deposits: Journal of the Alberta Society of Petroleum Geologists, vol. 3, no. 5, pp. 63-69.

Dickey, P.A., and W.C. Cox, 1977, Oil and gas reservoirs with subnormal pressures: American Association of Petroleum Geologists Bulletin, vol. 61, no. 12, pp. 2134-2142.

- Emsellem, Y. and G. De Marsily, 1973, An automatic solution for the inverse problem: Water Resources Research, vol. 7, no. 5, pp. 1264-1283.
- Evans, W.E., 1970, Imbricate linear sandstone bodies of Viking Fm. in Dodsland - Hoosier area of S.W. Sask.: American Association of Petroleum Geologists Bulletin, vol. 54, no. 3, pp. 469-486.
- Fatt, J., 1958, Compressibility of sandstones at low to moderate pressures: American Association of Petroleum Geologists Bulletin, vol. 42, pp. 1924-1957.
- Freeze, R.A., 1969a, Regional groundwater flow - Old Wives Lake Drainage Basin, Saskatchewan: Canadian Inland Waters Branch, Science Series no. 5, 245 p.
- Freeze, R.A., and P.A. Witherspoon, 1967, Theoretical analysis of regional groundwater flow: 2. Effect of water-table configuration and subsurface permeability variation: Water Resources Research, vol. 3, no. 2, pp. 623-634.
- Freeze, R.A., and J.A. Cherry, 1979, Groundwater: Prentice-Hall Inc., Englewood Cliffs, N.J., 604 p.
- Frind, E.O., and G.F. Pinder, 1973, Galerkin solution of the inverse problem for aquifer transmissivity: Water Resources Research, vol. 9, no. 5, pp. 1397-1410.
- Gammel, H.G., 1955, The Viking member in central Alberta: Journal of the Alberta Society of Petroleum Geologist, vol. 3, no. 5, pp. 63-69.
- Glaister, R.P., 1959, Lower Cretaceous of southern Alberta and adjoining areas: Bulletin of

the American Association of Petroleum Geologists, vol. 43, no. 3, pp. 590-640.

Gelubev, I.F., 1959, Viscosity of gases and gas mixtures: National Technical Information Services, United States Department of Commerce, Springfield, Va., 238 p.

Harris, W.E., B.J. Shortreed, J.R. Pow, and G.W. Govier, 1956, Viking Formation waters of Alberta: Journal of the Alberta Society of Petroleum Geologist, vol. 3, no. 4, pp. 151-159.

Hayes, B.J.R., 1982, Upper Jurassic and lower Cretaceous stratigraphy of southern Alberta and north-central Montana: Ph.D. thesis, University of Alberta, 234 p.

Herbaly, E.L., 1974, Petroleum geology of Sweetgrass arch, Alberta: American Association of Petroleum Geologists Bulletin, vol. 58, no. 11, pp. 2227-2244.

Hill, G.A., W.A. Colburn, and J.W. Knight, 1961, Reducing oil finding costs by use of hydrodynamic evaluations: in Economics of Petroleum Exploration, Development and Property Evaluation, Proceedings of 1961 Institute of the International Oil and Gas Education Center, Prentice-Hall Inc., Englewood Cliffs, N.J., pp. 38-69.

Hitchon, B., 1969b, Fluid flow in the western Canada sedimentary basin: 2, Effect of Geology: Water Resources Research, vol. 5, no. 2, pp. 460-463.

Hitchon, B., and I. Friedman, 1969c, Geochemistry and origin of formation waters in the western Canada sedimentary basin: 1, stable isotopes of hydrogen and oxygen; Geochimica et Cosmochimica Acta, vol. 33, pp. 1321-1349.

Horner, D.R., 1951, Pressure build up in wells: Proc. Third World Petroleum Congress, E.J.

Brill, Leiden II, 503 p.

Hubbert, M.K., 1940, The theory of groundwater motion: Journal of Geology, vol. 48, no. 8, pp. 785-944.

Hubbert, M.K., 1953, Entrapment of petroleum under hydrodynamic conditions: Bulletin of the American Association of Petroleum Geologists, vol. 37, no. 8, p. 1954-2026.

Johnston, 1964, Review of basic formation evaluation: Society of Petroleum Engineers, Paper 965, 29 p.

Jones, H.L., 1961, The Viking Formation of S.W. Saskatchewan, Department of Mineral Resources Saskatchewan, Report 65, 79 p.

Jones, H.L., 1962, Viking deposition, Discussion in: Journal of the Alberta Society of Petroleum Geologists, vol. 10, no. 4, p. 212.

Koldijk, W.S., 1976, Gilby Viking 'B': A storm deposit in: Lernard, M.M., ed., The Sedimentology of Selected Clastic Oil and Gas Reservoir in Alberta, Canadian Society of Petroleum Geologists, pp. 62-67.

Lynch, E.J., 1962, Formation evaluation: Harper and Row Publications (Reprinted in 1981), 422 p.

Marousa, L.F., 1973, Patterns of pressures in the Morrow sands of north-western Oklahoma: M.Sc. thesis, University of Tulsa, 95 p.

McDonald, G.M., and G.H. Harbaugh, 1983, A modular three-dimensional finite-difference

groundwater-flow model, Users Manual: United States Geological Survey

Neuman, S.P., 1973, Calibration of distributed parameter groundwater flow models viewed as a multiple- objective decision process under uncertainty: Water Resources Research, vol.9, no.4, pp. 1006-1021.

Neuman, S.P. and S. Yakowitz, 1979, A statistical approach to the inverse problem of aquifer hydrology, 1, Theory: Water Resources Research, vol.15, no. 4, pp. 845-866.

Neuman, S.P., Fogg, G.E. and E.A. Jacobson, 1980, A statistical approach to the inverse problem of aquifer hydrology, 2, Case study: Water Resources Research, vol. 16, no. 1, pp. 33-58.

Neuzil, C.E., and D.W. Pollock, 1983, Erosional unloading and fluid pressures in hydraulically "tight" rocks: Journal of Geology, vol. 91, no. 2, pp. 179-193.

North, F.K., 1985, Petroleum Geology: Allan and Unwin Inc., Winchester, Mass., 607p.

Off, T., 1963, Rythmic linear sand bodies caused by tidal currents; American Association of Petroleum Geologists Bulletin, vol. 27, no. 2, pp. 324-341.

Roberts, W.H. III, 1980, Design and function of oil and gas traps: in problems of petroleum migration (Roberts, W.H. and Cordell, R.J., ed.), American Association of Petroleum Geologists Studies in Geology, no. 10, pp. 217-240.

Roberts, W.H. III and R.J. Cordell (eds), 1980, Problems of petroleum migration: American Association of Petroleum Geologists Studies in Geology, no. 10, 240p.

- Roessing, H.K., 1959, Viking deposition in the southern Alberta plains: Journal of the Alberta Society of Petroleum Geologist, 9th Annual Conference, pp. 130-137.
- Russell, J., 1972, Pressure-depth relations in Appalachian region: American Association of Petroleum Geologists Bulletin, vol. 56, no. 3, pp. 528-536.
- Schwartz, F.W., K. Muhlenbachs, and D.W. Chorley, 1981, Flow-system controls of the chemical evolution of groundwater: Journal of Hydrology, vol. 54, pp. 225-243.
- Short, C., 1979, Underpressured wells in the Michigan basin: B.Sc. thesis, Queen's University, 21 p.
- Silver, C., 1973, Entrapment of petroleum in isolated porous bodies: American Association of Petroleum Geologists Bulletin, vol. 57, pp. 726-740.
- Simpson, F., 1975, Marine Lithofacies and Biofacies of Colorado Group (Middle Albian to Santonian) in Saskatchewan : Geological Association of Canada Special Paper 13, pp. 553-587.
- Stelck, C.R., and J. Armstrong, 1981, Neogastropolites from southern Alberta: Bulletin of Canadian Petroleum Geology, vol. 29 no. 3, pp. 399-407.
- Taylor, R.S., W.H. Mathews, and W.D. Kupsch, 1964, Tertiary: in Geological History of Western Canada (R.G. McCrossan and R.P. Glaister, eds.), Journal of the Alberta Society of Petroleum Geologist, Chapter 13, pp. 190-194.
- Telford, W.M., L.P. Geldhart, R.E. Sheriff and D.A. Keys, 1977, Applied Geophysics: Cambridge University Press, Cambridge, 860 p.



Thomas, M.B., 1977, Depth-porosity relations, Viking-Cardium, Alberta: M.Sc. thesis, University of Calgary, 147 p.

Tizzard, P.G., and Lerbekmo, J.F., 1975, Depositional history of Viking Fm. Suffield area, Alberta, Canada: Bulletin of Canadian Petroleum Geology, vol. 23, no. 4, pp. 715-752.

Tóth, J., 1962, A theory of groundwater motion in small drainage basins in central Alberta, Canada: Journal of Geophysical Research, vol. 67, no. 11, p. 4375-4387.

Tóth, J., 1966, Groundwater geology, movement, chemistry and resources near Olds, Alberta: Research Council of Alberta, Bulletin 17, 126 p.

Tóth, J., 1970, Relation between electric analogue patterns of groundwater flow and accumulations of hydrocarbons: Canadian Journal of Earth Sciences, vol. 7, no. 3, pp. 988-1007.

Tóth, J., 1980, Cross-formational gravity flow of groundwater: A mechanism of transport and accumulation of petroleum (The generalized hydraulic theory of petroleum migration): in Problems of Petroleum Migration (Roberts, W.H., and R.J. Cordell, eds.), American Association of Petroleum Geologists Bulletin, no. 10, pp. 121-168.

Tóth, J., and R.E. Millar, 1983, Possible effects of erosional changes of the topographic relief on pore pressures at depth: Water Resources Research, vol. 19, no. 6, pp. 1585-1597.

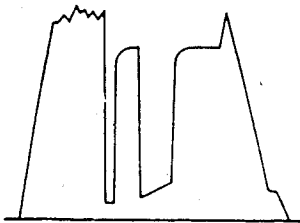
Tóth, J., and T. Corbet, 1986, Post-Paleocene evolution of regional groundwater flow-systems and their relation to petroleum occurrences, Taber area, southern Alberta, Canada: Bulletin of Canadian Petroleum Geology, vol. 34, no. 3, pp. 339-363.

Vacquier, V., N.C. Steenland, R.G. Henderson and I. Zeitz, 1951, Interpretation of aeromagnetic maps; Geological Society of America, Memoir 47, 147 p.

Wang, H.F., and M.P. Anderson, 1982, Introduction to groundwater modeling: The Finite Difference and Finite Element Methods: W.H. Freeman and Co., San Francisco, 237 p.

## **5. APPENDICES**

## Appendix 2A.1 - Schematic charts for determination of DST quality



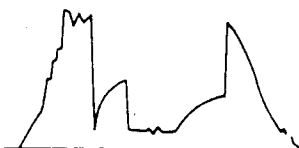
### A High

1. Test mechanically sound
3. Flow pressures verify recoveries and/or flow rates
5. Recorder depths given
6. Recorder within interval tested
7. ISI stabilized, or nearing stabilization with increments
8. Prewell time long enough to release hydrostatic head
10. Two good shut-ins required
11. PMAV Range of approximately 1 to 25 lbs. from read shut-in pressure. (7 to 172 kPa)



### B Requires Extrap.

12. Slight mechanical difficulties, but does not affect the test
13. Shut-ins not fully stabilized
14. Only one good shut-in
15. Recorder pressures disagree from 1 to 19 PSI (7 to 131 kPa) after recorder drag and depth difference
17. PMAV range of approximately 20 to 35 lbs. from read shut-in pressure (138 to 241 kPa)
48. Recoveries do not verify flow pressures



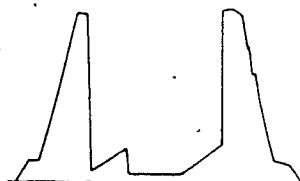
### C Caution (Plugging)

18. Some mechanical difficulties evident on chart, however do not appear to affect pressure data
19. Recorders run above the interval
21. Prewell not opened long enough, possibly slightly supercharged
22. Packer may have leaked slightly
24. Recorder pressures disagree from 20 to 29 PSI (138 to 200 kPa) after recorder drag and depth difference
25. Only one recorder. Must be within interval.
26. PMAV range of approximately 30 to 85 lbs. from read shut-in pressure (207 to 587 kPa)
27. Only one shut-in, but follows a flow period longer than shut-in time



### D Questionable

28. Not totally mechanically sound
29. Only one recorder, and run inside above the interval
30. No recorder depth or questionable
32. No ISI, FSI building too fast to obtain reasonable extrapolation
33. Questionable interval depths
34. Supercharged ISI, FSI follows long valve-open period
35. No chart from below bottom packer
36. Recorder pressures disagree from 30 PSI (206.8 kPa) and over after recorder drag and depth difference
37. PMAV range of approximately 80 to 150 lbs. from read shut-in pressure (552 to 1034.2 kPa)



### E Low Perm, Low Pressure

38. Covers all requirements of Code A, however, very low permeability and low pressure, unable to extrapolate
39. Very low permeability, low pressure, but problems encountered thru-out test
46. Low perm, rel. high pressure for Code E



### F Low, Perm, High Pressure

40. Covers all requirements of Code A, however low permeability and high pressure. (CAUTION: Watch for Cushion)
41. Low permeability, high pressure, but problems encountered thru-out test
47. Low perm, rel. low pressure for Code F



### G Misrun

63. Unable to obtain initial packer seat
64. Lost seat after tool opened
68. Both elements ruptured
69. Plugged tool
70. Unable to reach test depth
71. Tool failure
99. Flows incremented

### Note:

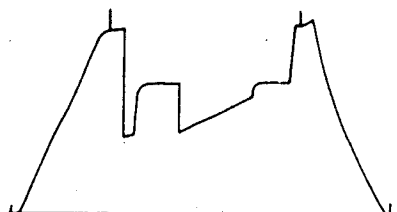
Quality Code information is programmed into the data base, as listed, by both letter and number, e.g. B13, G64. This is done to enhance the credibility of the data base. Should a user wish to investigate any specific coding instance, classification details are immediately retrievable.

## Appendix 2A.2 • Schematic charts for qualitative DST permeability determination



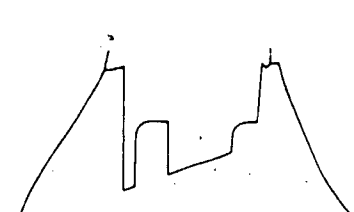
### (EX) Excellent

The final flow pressure has stabilized with final shut-in. The quicker the stabilization, the better the permeability.



### (HI) High

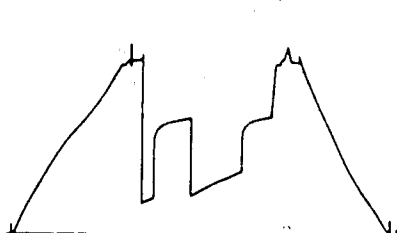
Good flowing pressure and shut-ins nearing stabilization.



### (RH) Relatively High

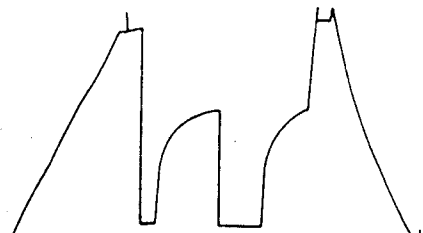
Good flowing pressure and shut-ins are still building slightly, or ...

Depth: 2050' - 2062' Recovery: 370'  
heavy crude oil, 15' mud cut oil



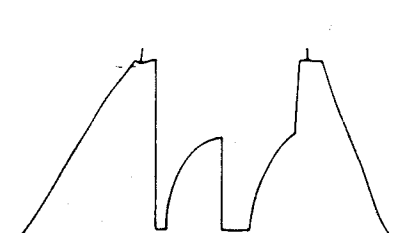
### (AV) Average

Average flowing pressures and shut-ins still building fairly rapidly.



### (RL) Relatively Low

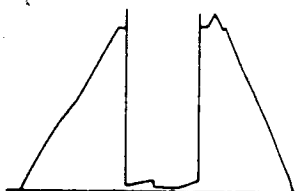
Flowing pressures low and shut-ins still building fairly rapidly.



### (LO) Low

Poor flowing pressures and shut-ins are building very rapidly, or ...

Poor flowing pressures and shut-ins and building too rapidly to extrapolate with any accuracy.



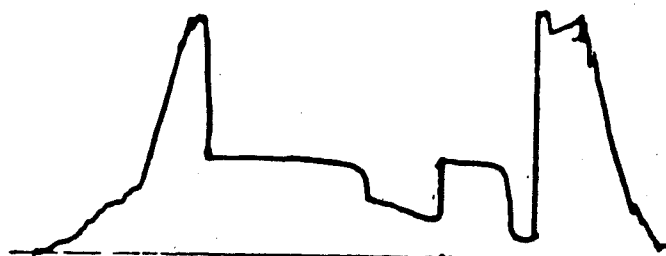
### (VN) Virtually None

Flow pressures are nearly nil and shut-ins are building too rapidly to extrapolate with any accuracy.

Appendix 2B.1 - DST description for the WESTCOAST TABERS 15-36-8-18W4M well

Westcoast Taber S 5-36-8-18-W4 T.# A1273-2 DST.# 2

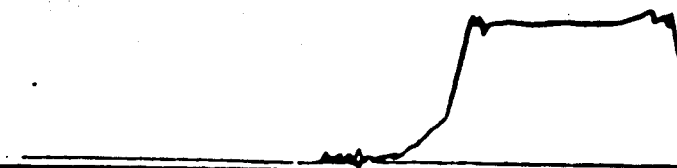
Rec.# 5041



Rec.# 3690



Rec.# 3853



100/ 05-36-00M-1N-W-4 /00  
WESTCOAST TAPER S.

DST# 002  
Rec# 003690

Interval: 729.0 to 735.0 m  
Rec depth: 732.0 m OUTSIDE  
Capacity: 39645.0 kPa

FM: 1-OPS 1-BSID

Kelly cushion: 916.3  
Rec. cushion: 184.3  
Total depth: 762.6

	TIMES (min.)	PRESS kPa	EXTRAP(L) kPa	QUALITY CODE
Preflow	20.0	729.0		G-
Init. S.I.	60.0	3557.0	3733.6	G
		1469.0		
2nd. flow.	60.0	2098.0		G
Final S.I.	120.0	3557.0	3567.7	G
Init. hydrostatic		8288.0		
Final hydrostatic		8278.0		

Test type: DCSBY4P  
Test qual: B  
-nv: 17

Hole cond: G  
Cushion type:  
Fluid amount:  
Gas amount:  
Inhibitor:

Permeability: RM  
Damage: NO  
Hydro factor:  
Viroin press: 3733.  
Pot. surface:

Gas measurements:

First: 300.0  
Last: 300.0  
Max: 300.0

Recovery description (From multiple tests: NO)

10.0 m DRILLING MUD.  
190.0 m WATER.  
GAS RATE TAKEN FROM PETROFICHE.

Blow description

STRONG AIR BLOW ON PREFLOW. NO GAS TO SURFACE. STRONG AIR BLOW ON FINAL FLOW, DECREASING SLIGHTLY THROUGHOUT. GAS TO SURFACE LAST 15 MINUTES OF FINAL FLOW, TOO SMALL TO MEASURE.

GENERAL COMMENTS

RELATIVELY HIGH PERMEABILITY. INITIAL SHUT-IN STILL.  
FINAL SHUT-IN NEARLY STABILIZED. PRESSURES COMPARE.

Well Name: WESTCOAST TABER S.  
 Well Location: 10U/ 05-36-00R-1H-W-4 /00 DST# 002  
 Recorder Number: 003690  
 M.B. elevation: 3006.2 ft  
 Interval Tested: 2391.7 ft to 2411.4 ft  
 Recorder Depth: 2401.6 ft  
 Total Flow Time: 20.0 min

## Initial-Shutin Pressures (Liquid)

Time (min) Phi	Delta-P (psi)	(T+Phi) /Phi	Pressure (psi)
.0	.0		105.7
.5	103.3	38.8497	209.1
.9	170.3	22.5735	276.1
1.7	214.4	12.4659	320.1
3.0	253.6	7.7202	359.3
4.8	286.1	5.2010	391.9
8.2	312.0	3.4388	417.8
11.5	337.9	2.7387	443.6
14.3	350.4	2.4029	456.1
16.9	362.8	2.1854	466.6
19.5	372.4	2.0262	474.2
24.0	384.9	1.8322	490.6
28.6	389.7	1.6998	495.5 *
30.0	393.6	1.6676	499.3 *
31.6	396.5	1.6327	502.2 *
34.0	398.4	1.5890	504.1 *
35.5	400.3	1.5639	506.1 *
38.1	402.3	1.5251	506.0 *
40.4	404.2	1.4947	510.0 *
41.9	405.2	1.4768	510.9 *
43.9	406.2	1.4558	511.9 *
46.1	407.1	1.4340	512.9 *
48.3	408.1	1.4142	513.9 *
50.2	410.1	1.3983	515.8 *
51.2	410.2	1.3908	515.9 *



## Initial-Shut-in Pressures (Liquid)

Time (min) Ph1	Delta-P (psi)	(T+Ph1) /Ph1	Pressure (psi)
54.5	410.2	1.3071	515.9 *
56.6	410.2	1.3536	515.9 *
59.6	410.2	1.3356	515.9 *
60.0	410.2	1.3333	515.9 *

\* Values used in Horner analysis

Extrapolated pressure: 541.5 psi

Horner slope: 186.9855 psi/cycle

Slope Log(dP) vs Log(Ph1): .0647

WESTCOAST TABER S.

RECORDER# 003690

TEST DATE 78 10 10

FROM: 2391.7F

TO: 2411.4FT

DEPTH: 2401.6FT

KB: 3006.2FT

FM: 1-BFS

1-BSLD

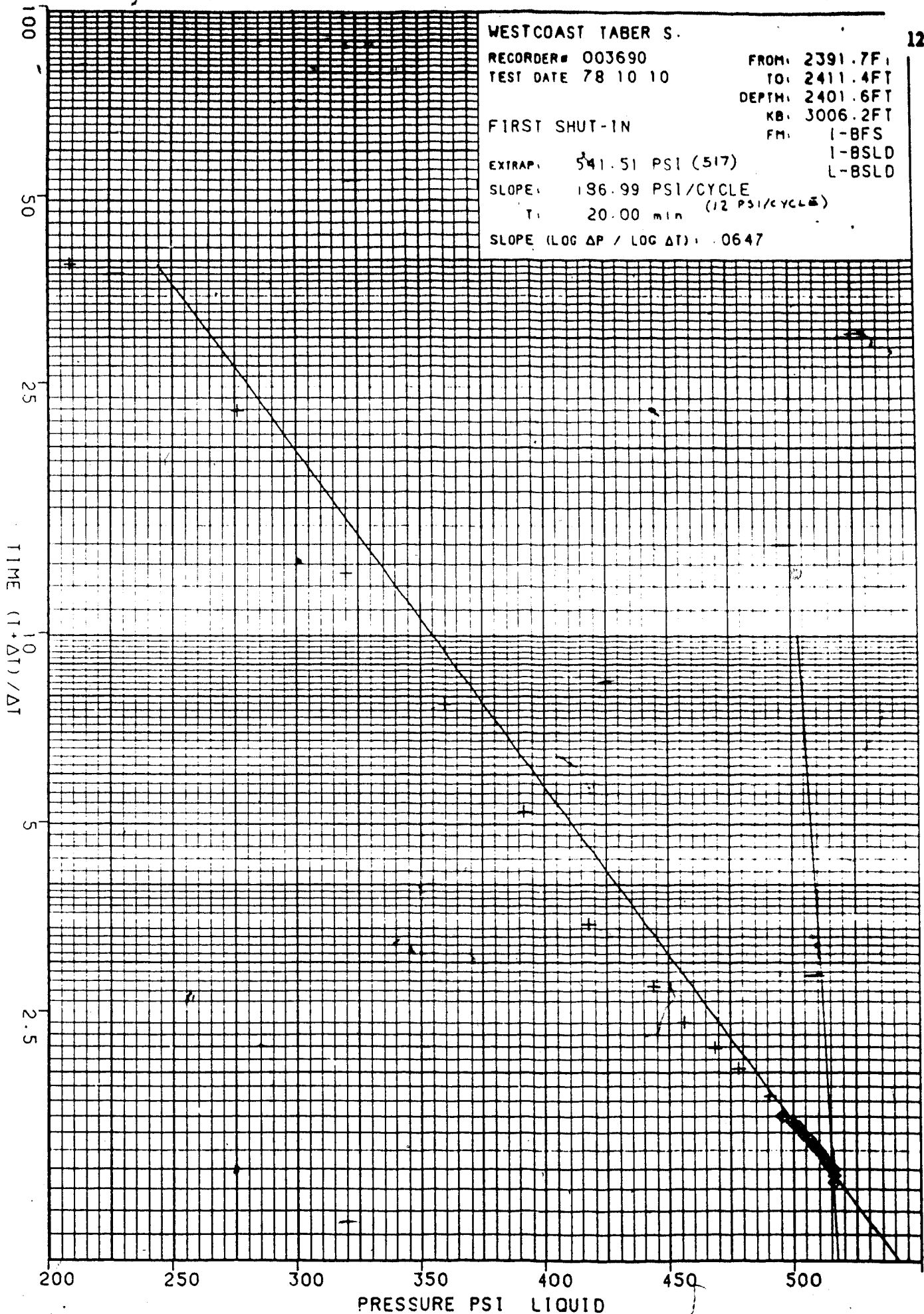
L-BSLD

FIRST SHUT-IN

EXTRAP: 541.51 PSI (517)

SLOPE: 186.99 PSI/CYCLE

T: 20.00 min (12 PSI/CYCLE)

SLOPE (LOG  $\Delta P$  / LOG  $\Delta T$ ): .0647

Well Name: WESTCOAST TAPER S.  
 Well Location: 100/ 05-36-008-18-W-4 /00 DST: 002  
 Recorder Number: 003690  
 M.B. elevation: 3006.2 ft  
 Interval Tested: 2391.7 ft to 2411.4 ft  
 Recorder Depth: 2401.6 ft  
 Total Flow Time: 80.0 min

Final-Shutin Pressures (Liquid )

Time (min)	Delta-P (psi)	(T+Phi) /Phi	Pressure (psi)
.0	.0		304.3
1.6	71.2	50.5254	375.5
3.5	118.2	24.0631	422.4
6.3	140.1	13.7064	444.4
8.8	158.5	10.1386	462.8
11.8	174.6	7.7655	478.9
14.8	181.2	6.4164	485.5
17.3	187.7	5.6117	492.0
20.2	194.3	4.9063	498.0
23.1	200.9	4.4610	505.2
26.2	206.7	4.0555	511.0 *
29.0	211.1	3.7582	515.4 *
31.9	211.6	3.5040	515.4 *
34.7	211.6	3.0676	515.9 *
43.4	211.6	2.8454	515.9 *
49.5	211.6	2.6166	515.9 *
55.0	211.6	2.4544	515.9 *
61.4	211.6	2.3033	515.9 *
66.8	211.6	2.1980	515.9 *
71.2	211.6	2.1237	515.9 *
75.9	211.6	2.0547	515.9 *
80.4	211.6	1.9952	515.9 *
85.8	211.6	1.9326	515.9 *
89.3	211.6	1.8954	515.9 *
93.8	211.6	1.8533	515.9 *

## Final-Shutin Pressures (Liquid )

Time (min)	Delta-P (psi)	(T+Phi) /Phi	Pressure (psi)
99.2	211.6	1.8068	515.9 *
107.7	211.6	1.7426	515.9 *
111.4	211.6	1.7180	515.9 *
120.0	211.6	1.6667	515.9 *

\* Values used in Horner analysis

Extrapolated pressure: 517.4 psi

Horner slope: 5.0285 psi/cycle

Slope Log(dP) vs Log(Phi): .0057 °

WESTCOAST TABER S.

RECORDER# 003690

TEST DATE 78 10 10

FROM: 2391.7FT

TO: 2411.4FT

DEPTH: 2401.6FT

KB: 3006.2FT

FM: I-BFS

I-BSLD

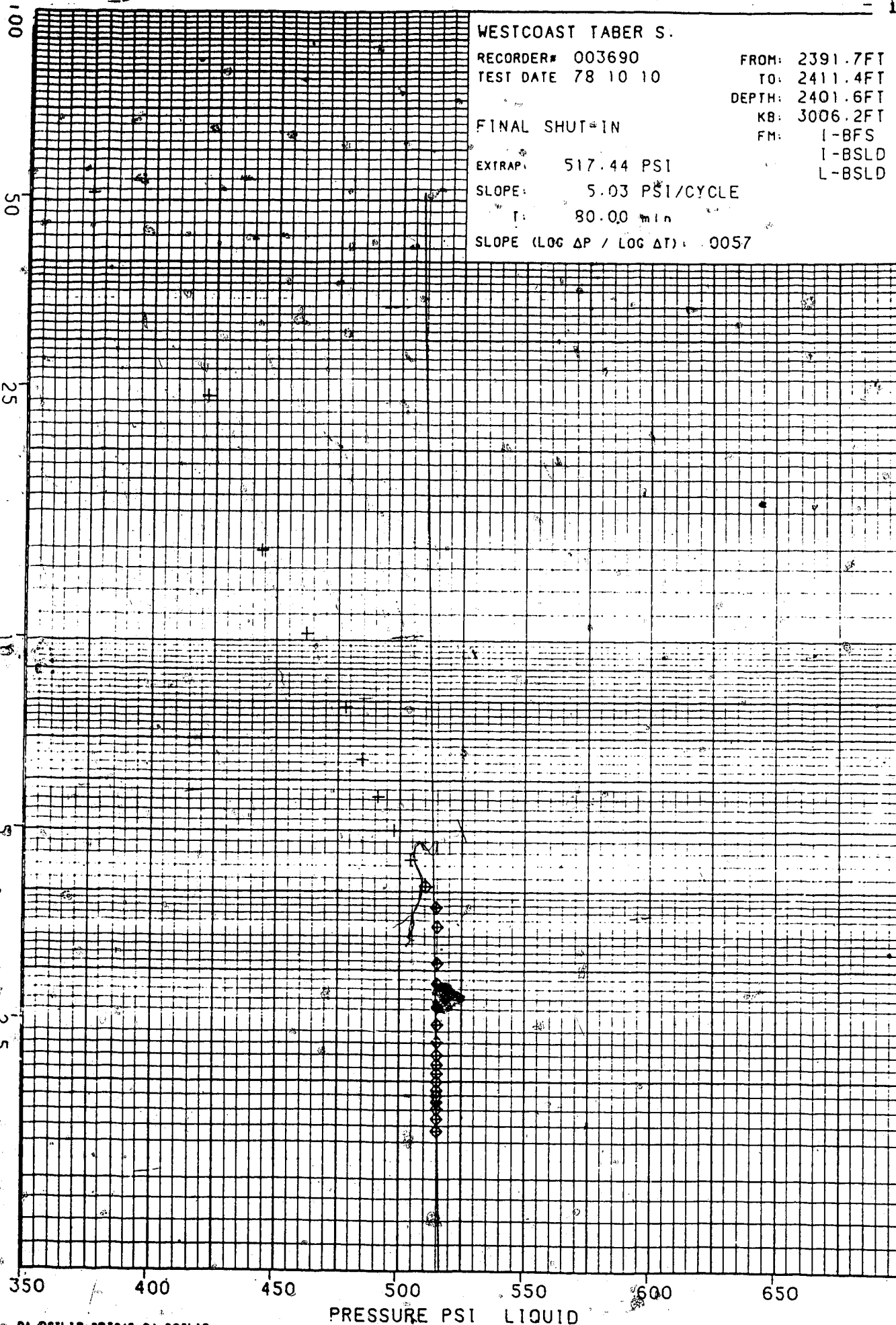
L-BSLD

FINAL SHUT-IN

EXTRAP: 517.44 PSI

SLOPE: 5.03 PSI/CYCLE

T: 80.00 min

SLOPE (LOG  $\Delta P$  / LOG  $\Delta T$ ): .0057TIME (T +  $\Delta T$ ) /  $\Delta T$ 

# Reservoir Calculations \*\*\*\*\*

Well Name: WESTCOAST TABER S.  
Location: 100/ 05-36-008-18-W-4 /00  
Dst Number: 002

Test Date: 78 10  
License No: 72032  
Ticket No: 0

## Reservoir Parameters:

Interval From: 729.00 m  
To: 735.00 m

DC Length: 139.28 m

DC Id. 73.03 mm

DP Size: 102.00 mm

DP Length:

Hole Size: 200.00 mm

Porosity: 20.00

Liquid Cush:

Inhibitor Amt:

Res. Temp: 24.00 C

Net Pay: 1.90 m

Total Rcv: 190.00 m

## Liquid:

Api Gravity:

Viscosity:

.800 mPa.s

Spec Gravity:

1.010

## Liquid Calculations:

Horner: Slope (kPa)

Initial

Final

Extrap. (kPa)

1289.219

34.671

3733.6

3567.7

Slope Log(dP) vs Log(dT):

.0647

.0057

Ave. Prod. Rate (m3/d)

15.68

15.68

Transmissibility(mD.m/mPa.s)

25.79

959.12

In-Situ Capacity(mD.m)

20.63

767.31

Effective Perm. (mD)

10.86

403.85

Radius Of Inves.(m)

4.49

47.45

Damage Ratio

.56

6.85

Productivity Idx(m3/kPa.D)

.005

.011

-Damage Removed (m3/kPa.D)

.005

.073

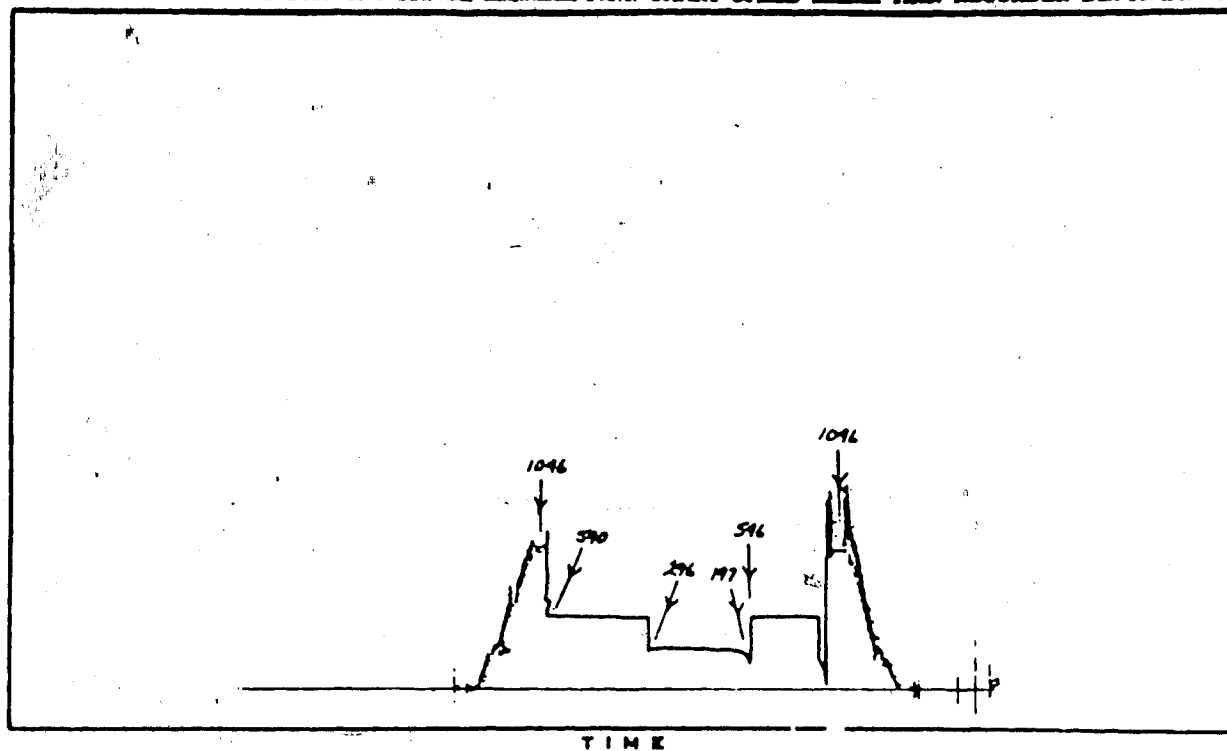
Draw Down

4.445

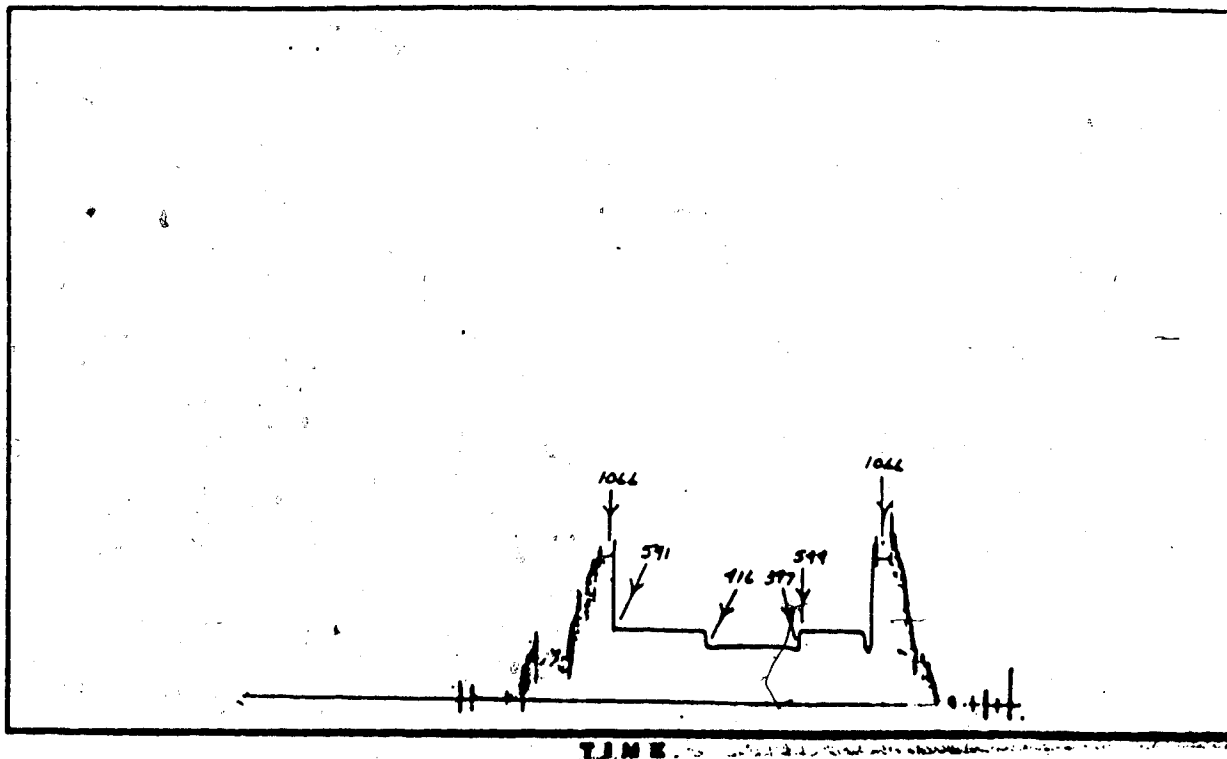
Appendix 2B.2 - DST description for THE GNOC CIGOL TABERS 6-15-8-17W4M well

WELL NAME GNOL CIGOL TABERS 6-15

RECORDER No. 3807 ELEMENT RANGE 4500 P.S.I. CHART SPEED 12 HRS. RECORDER DEPTH 2265



RECORDER No. 3808 ELEMENT RANGE 4550 P.S.I. CHART SPEED 12 HRS. RECORDER DEPTH 2310



100/ 06-15-00H-17-W-4 /00  
GNUM CIGUL TABERS

Test date: 75 10 07

DST# 002  
Rec# 003808

Interval: 695.6 to 705.9 m  
Rec depth: 704.1 m OUTSIDE  
Capacity: 31371.1 kPa

FM: 1-BFS 1-BSLD

Kelly bushing: 897.6  
Rec. subsea: 193.5  
Total depth: 733.7

	TIMES (min.)	PRESS kPa	EXTRAP(G) kPa	QUALITY CODE
Preflow	5.0	2757.9		G
Init. S.I.	60.0	3750.7	3756.9	G
		2737.2		
2nd. flow.	90.0	2868.2		G
Final S.I.	90.0	3730.1	3732.1	G
Init. hydrostatic		7349.8		
Final hydrostatic		7349.8		

Test type: DCSHY4P  
Test qual: A  
why:

Hole cong:  
Cushion type:  
Fluid amount:  
Gas amount:  
Inhibitor:

Permeability: RH  
Damage: NO  
Hydro factor: G  
Virgin press: 3757.0 kPa  
Pot. surface:

Gas measurements:  
First: 26525.8 m3/d  
Last: 31084.4 m3/d  
Max: 31084.4 m3/d

Recovery description (From multiple tests: NO)

27.4 m MUDDY WATER.

#### Blow description

GOOD BLOW THROUGHOUT PREFLOW. GAS TO SURFACE IN 1 MINUTE. STRONG STEADY GAS BLOW THROUGHOUT FINAL FLOW. WATER SPRAY AFTER 20 MINUTES.

#### GENERAL COMMENTS

RELATIVELY HIGH PERMEABILITY. BOTH SHUT-INS STABILIZED.



Well Name: GNOC CIGOL TABERS  
 Well Location: 100/ 06-15-008-17-W-4 /00 USTa 002  
 Recorder Number: 003808  
 K.B. elevation: 2945.0 ft  
 Interval Tested: 2282.0 ft to 2316.0 ft  
 Recorder Depth: 2310.0 ft  
 Total Flow Time: 5.0 min

## Initial-Shutin Pressures (Gas)

Time (min)	Delta-P (psi)	(I+Phi) /Phi	Pressure (psi)	Pressure (psi <sup>2</sup> )/10 <sup>-6</sup>
.0	.0		400.0	.16000
1.2	24.7	5.1723	424.7	.18037
1.8	102.0	3.8098	502.0	.25198
3.1	119.1	2.6103	519.1	.26944
5.5	131.2	1.9055	531.2	.28216
7.7	133.7	1.6477	533.7	.28479
8.6	137.7	1.5803	537.7	.28910
10.1	144.0	1.4967	544.0	.29594
12.9	144.0	1.3883	544.0	.29594
14.0	144.0	1.3579	544.0	.29594
14.6	144.0	1.3428	544.0	.29594
17.8	144.0	1.2807	544.0	.29594
21.1	144.0	1.2368	544.0	.29594
24.2	144.0	1.2066	544.0	.29594
27.4	144.0	1.1823	544.0	.29594
30.2	144.0	1.1653	544.0	.29594
34.8	144.0	1.1438	544.0	.29594
37.9	144.0	1.1321	544.0	.29594
39.2	144.0	1.1277	544.0	.29594
41.0	144.0	1.1219	544.0	.29594
42.7	144.0	1.1170	544.0	.29594
43.7	144.0	1.1145	544.0	.29594
45.5	144.0	1.1100	544.0	.29594
47.0	144.0	1.1063	544.0	.29594
48.1	144.0	1.1039	544.0	.29594

Continued on next page

## Initial-Shut-in Pressures (Gas)

Time (min) Phi	Delta-P (psi)	(T+Phi) /Phi	Pressure (psi)	Pressure (psi <sup>2</sup> )/10 <sup>-6</sup>
50.7	144.0	1.0985	544.0	.29594 *
52.3	144.0	1.0955	544.0	.29594 *
54.0	144.0	1.0926	544.0	.29594 *
57.9	144.0	1.0864	544.0	.29594 *
60.0	144.0	1.0833	544.0	.29594 *

\* Values used in Horner analysis

Extrapolated pressure: 544.9 psi

Horner slope: .0165 (psi<sup>2</sup>/10<sup>-6</sup>)/cycle

Slope Log(dP) vs Log(Phi): .0071

## GNOC CIGOL TABERS

RECORDER# 003808

TEST DATE 75 10 07

FROM: 2282.0FT

TO: 2316.0FT

DEPTH: 2310.0FT

KB: 2945.0FT

FM: 1-BFS

1-BSLD

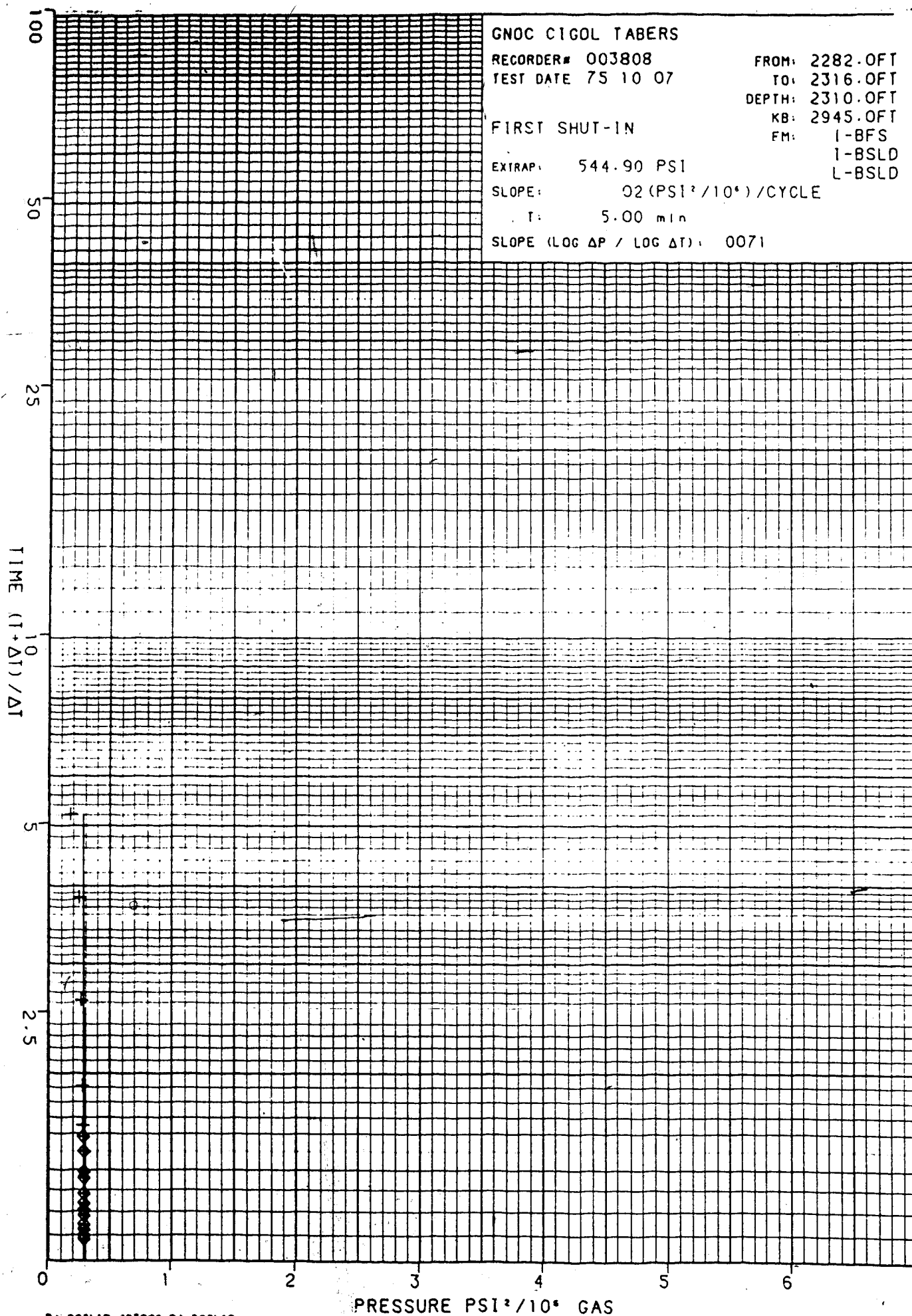
L-BSLD

FIRST SHUT-IN

EXTRAP: 544.90 PSI

SLOPE: 02 (PSI<sup>2</sup>/10<sup>6</sup>)/CYCLE

T: 5.00 min

SLOPE (LOG  $\Delta P$  / LOG  $\Delta T$ ): 0071

Well Name: GNOC CIGOL TABERS  
 Well Location: 100/ 06-15-00R-17-W-4 /00 DST# 002  
 Recorder Number: 003808  
 K.B. elevation: 2945.0 ft  
 Interval Tested: 2282.0 ft to 2316.0 ft  
 Recorder Depth: 2310.0 ft  
 Total Flow Time: 95.0 min

## Final-Shutin Pressures (Gas)

Time (min)	Delta-P Psi	(T+Phi) /Phi	Pressure (psi)	Pressure (psi <sup>2</sup> )/10 <sup>-6</sup>
.0	.0		416.0	.17306
.6	50.8	153.8850	466.8	.21792
1.6	80.3	60.8370	496.3	.24632
4.2	107.8	23.8798	523.8	.27441
7.7	120.5	13.3649	536.5	.28783
10.4	120.5	10.1775	536.5	.28763
13.8	121.0	7.8908	537.0	.28842
14.9	122.1	7.3945	538.1	.28954
16.4	123.7	6.7981	539.7	.29132
19.0	123.7	6.0058	539.7	.29132
22.9	123.7	5.1547	539.7	.29132
24.0	124.1	4.9561	540.1	.29174
26.6	125.0	4.5697	541.0	.29268
28.9	125.0	4.2872	541.0	.29268
31.7	125.0	3.9947	541.0	.29268
34.6	125.0	3.7441	541.0	.29268
37.7	125.0	3.5215	541.0	.29268
41.0	125.0	3.3152	541.0	.29268
47.6	125.0	2.9963	541.0	.29268
52.2	125.0	2.8182	541.0	.29268
54.8	125.0	2.7348	541.0	.29268
57.7	125.0	2.6454	541.0	.29268
63.2	125.0	2.5042	541.0	.29268
69.6	125.0	2.3658	541.0	.29268
75.7	125.0	2.2543	541.0	.29268

Continued on next page

## Final-Shut-in Pressures (Gas)

Time (min) Phi	Delta-P (psi)	(T+Phi) /Phi	Pressure (psi)	Pressure (psi <sup>2</sup> )/10 <sup>-6</sup>
79.3	125.0	2.1976	541.0	.29268 *
82.3	125.0	2.1543	541.0	.29268 *
87.1	125.0	2.0905	541.0	.29268 *
90.0	125.0	2.0556	541.0	.29268 *

\* Values used in Horner analysis

Extrapolated pressure: 541.3 psi

Horner slope: .0008 (psi<sup>2</sup>/10<sup>-6</sup>)/cycle

slope Log(dP) vs Log(Phi): .0016

## GNOC CIGOL TABERS:

RECORDER# 003808

TEST DATE 75 10 07

FROM: 2282.0FT

TO: 2316.0FT

DEPTH: 2310.0FT

KB: 2945.0FT

FM: 1-BFS

1-BSLD

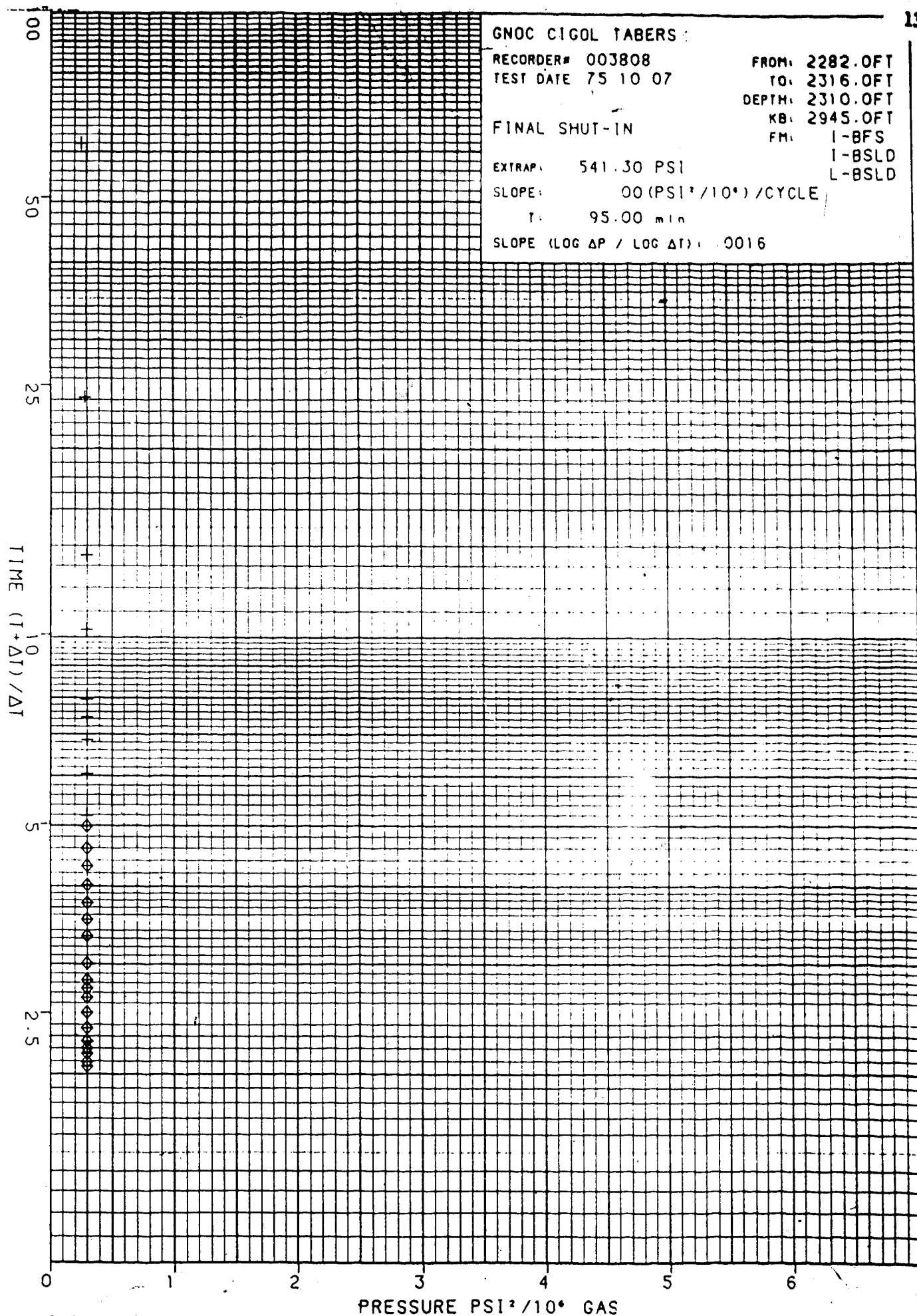
L-BSLD

FINAL SHUT-IN

EXTRAP: 541.30 PSI

SLOPE: 00 (PSI<sup>2</sup>/10<sup>6</sup>)/CYCLE

T: 95.00 min

SLOPE (LOG  $\Delta P$  / LOG  $\Delta T$ ): 0016

# Reservoir Calculations

Well Name: GWUC CIGOL TAHERS  
Location: 100/ 06-15-008-17-W-4 /00  
Dst Number: 002

Test Date: 75 10 07  
License No: 55176  
Ticket No: U

## Reservoir Parameters:

Interval From: 695.55 m  
To: 705.92 m

DC Length: 182.04 m DC Id. 60.32 mm

DP Size: 88.90 mm DP Length:

Hole Size: 158.75 mm Porosity: 18.50

Liquid Cush: Inhibitor Amt:

Res. Temp: 24.00 C Net Pay: 2.40 m

Total Rcv: 27.43 m

## Gas:

Z: .937 Spec Gravity: .630  
Viscosity: .012 mPa.s Dst Gas Rate: 31064.359 m3/d

Gas Calculations: Initial Final  
Horner: Slope (kPa<sup>2</sup>/10<sup>-6</sup>) .7863 .0382  
Extrap. (kPa) 3756.9 3732.1

Slope Log(dP) vs Log(dT): .0071 .0016

Transmissibility(mD.m/mPa.s)	16410.89	338065.88
In-Situ Capacity(mD.m)	196.93	4856.79
Effective Perm. (mD)	82.05	1690.33
Radius Of Inves.(m)	2.88	55.28
Actual Capacity (mD.m)	59.65	138.90
Damage Ratio	3.30	29.21
Est Damage Ratio	2.47	32.45
Maximum Aof. (m3/d)	67410.67	75930.94
-Damage Removed (m3/d)	222551.38	2217703.00
Minimum Aof. (m3/d)	45775.73	48582.55
-Damage Removed (m3/d)	151125.19	1418942.78
Draw Down		.660

## Appendix 3A - Glossary of Terms

### English

A	area
$A_0$	integral describing prolate spheroid
$A_\lambda$	integral describing prolate spheroid
a,b	major and minor axes of an ellipse
B	formation volume factor
$B_0$	integral describing prolate spheroid
$B_\lambda$	integral describing prolate spheroid
b	porous interval or formation thickness in a DST
$C_0$	integral describing prolate spheroid
$C_\lambda$	integral describing prolate spheroid
DELC	distance between nodes in column direction
DELR	distance between nodes in row direction
e	eccentricity of an ellipse
$e'$	eccentricity of a confocal ellipse through external points
g	acceleration due to gravity
HNEW	hydraulic head value at end of iteration (section 3.3)
HOLD	hydraulic head value at end of previous iteration (section 3.3)
h	hydraulic head
$\partial h / \partial x$	hydraulic gradient in x direction
K	hydraulic conductivity
$K'$	hydraulic conductivity inside conductive body
k	absolute permeability
$k_e$	effective permeability
$k_r$	relative permeability



$L$	length; length of lens
$l$	length; distance from endpoint of lens to point of measurement
$L:W$	length to width ratio of lens
$m$	mass
$M$	slope, linear section of pressure analysis (Horner) plot
$M_g$	slope, linear section of pressure analysis (Horner) plot for gas
$P_f$	formation pressure during build-up at well
$P_{max}$	maximum (extrapolated) formation pressure from Horner plot (virgin reservoir pressure)
$P_o$	pressure in the well at drainage radius
$p$	formation pressure
$Q$	flow rate $[L^3/T] = (m^3/day)$
$r$	radial distance
$TK$	temperature Kelvin
$t$	time
$t_c$	total time of production at rate $Q$
$\Delta t$	elapsed time from beginning of shut-in period
$v_{x,y,z}$	velocity in x, y or z direction $[L/T]$
$Z$	gas deviation factor
$z$	elevation of standard datum

### Greek

$\alpha$	compressibility of water
$\beta$	compressibility of rock framework
$\partial, \Delta$	partial differential, difference
$\epsilon$	hydraulic conductivity-permeability contrast ( $K'/K, k'/k$ )

$\epsilon_t$	threshold permeability contrast
$\mu$	dynamic viscosity
$\eta$	porosity
$\rho$	density
$\Phi$	fluid potential
$\Phi_i$	fluid potential inside lens
$\Phi_o$	fluid potential outside lens
$\Phi_d$	distorted fluid potential
$\Delta\Phi, \Delta\Phi_{\pm}$	fluid-potential anomaly, positive and negative anomaly $\Delta\Phi =  \Phi_d - \Phi_o $
$\Delta\Phi_r$	relative fluid-potential anomaly, $\Delta\Phi/\Delta\Phi\epsilon_t$
$\Delta\Phi_i$	anomaly shift due to interference effect
$\Delta\Phi\epsilon_t$	magnitude of fluid-potential anomaly at the threshold permeability contrast ( $\epsilon_t$ )
$\psi$	pressure head (datum pressure)

```

DATA INPUT FOR 'BASIC PACKAGE', (ELLIPSE L:W=2:1)
H/L = 0.01, HOMO - ISO (OCT 30.85)
      1      22      24      4
07 00 00 00 00 00 00 00 00 00 11 12
      0      1
      1      1 (2412)      -1

```

[illegible]

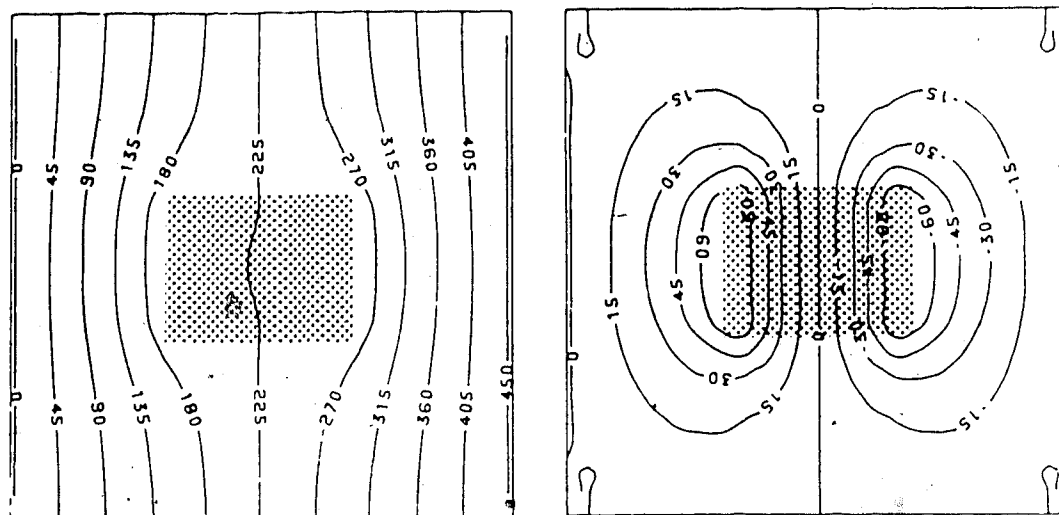


## \*\*\*\*\* USGS GROUNDWATER FLOW MODEL INPUT FOR BCF PACKAGE \*\*\*

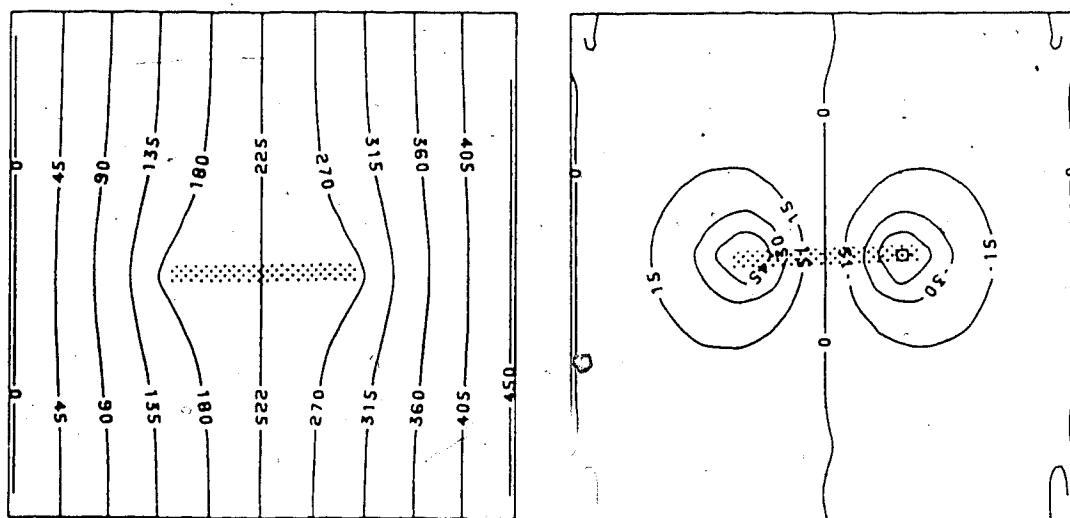
140

**Appendix 3C - Potentiometric surface and anomaly magnitude maps for various numerical  
simulations.**

2

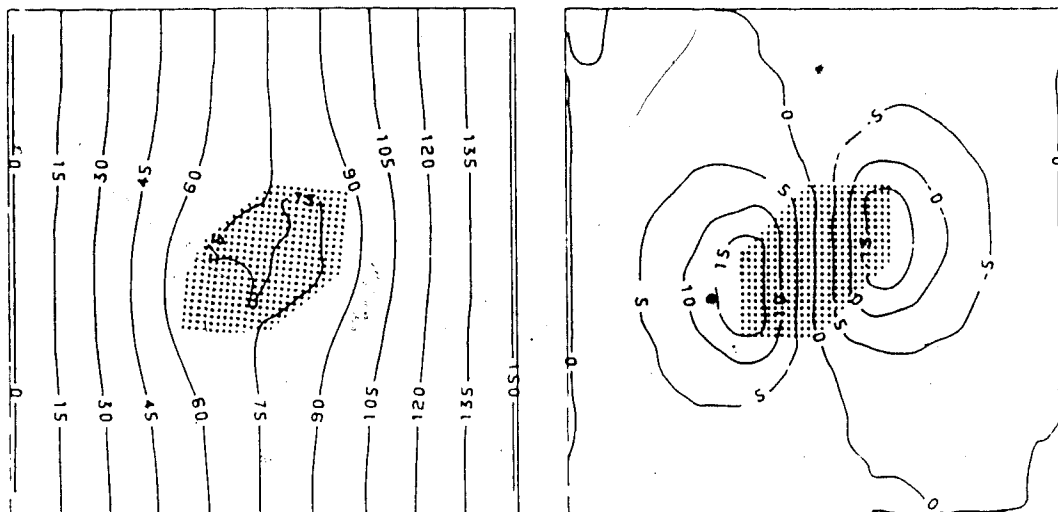


(a,b)

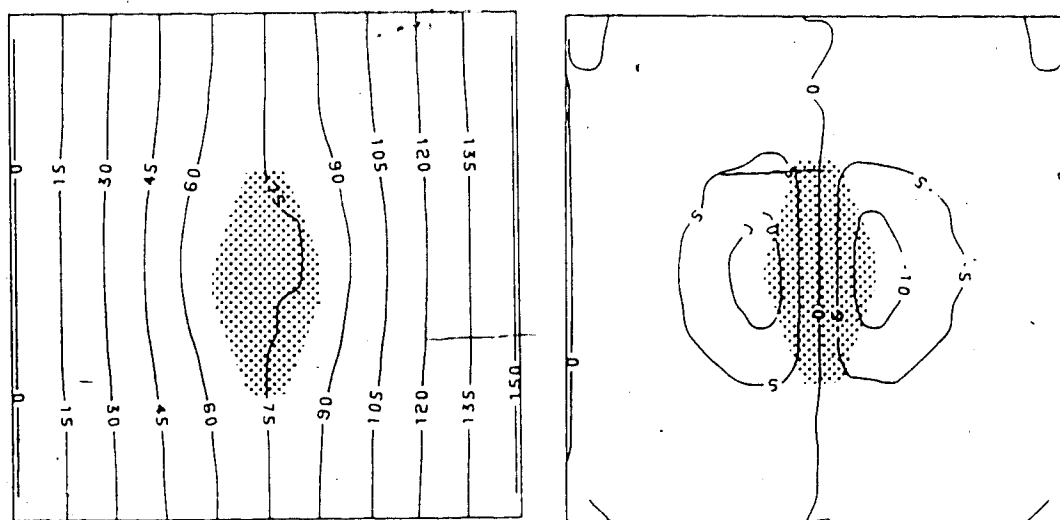


(c,d)

Figure 5.1 Potentiometric surface and anomaly maps for lenses of  $L:W=5:4$  and  $10:1$  and  $\epsilon=100$ , flow is from right to left.



a, b



c, d

Figure 5.2 Potentiometric surface and anomaly maps for a lens of  $L:W=2:1$  and flow at  $45^\circ$  a, b and  $90^\circ$  c, d.





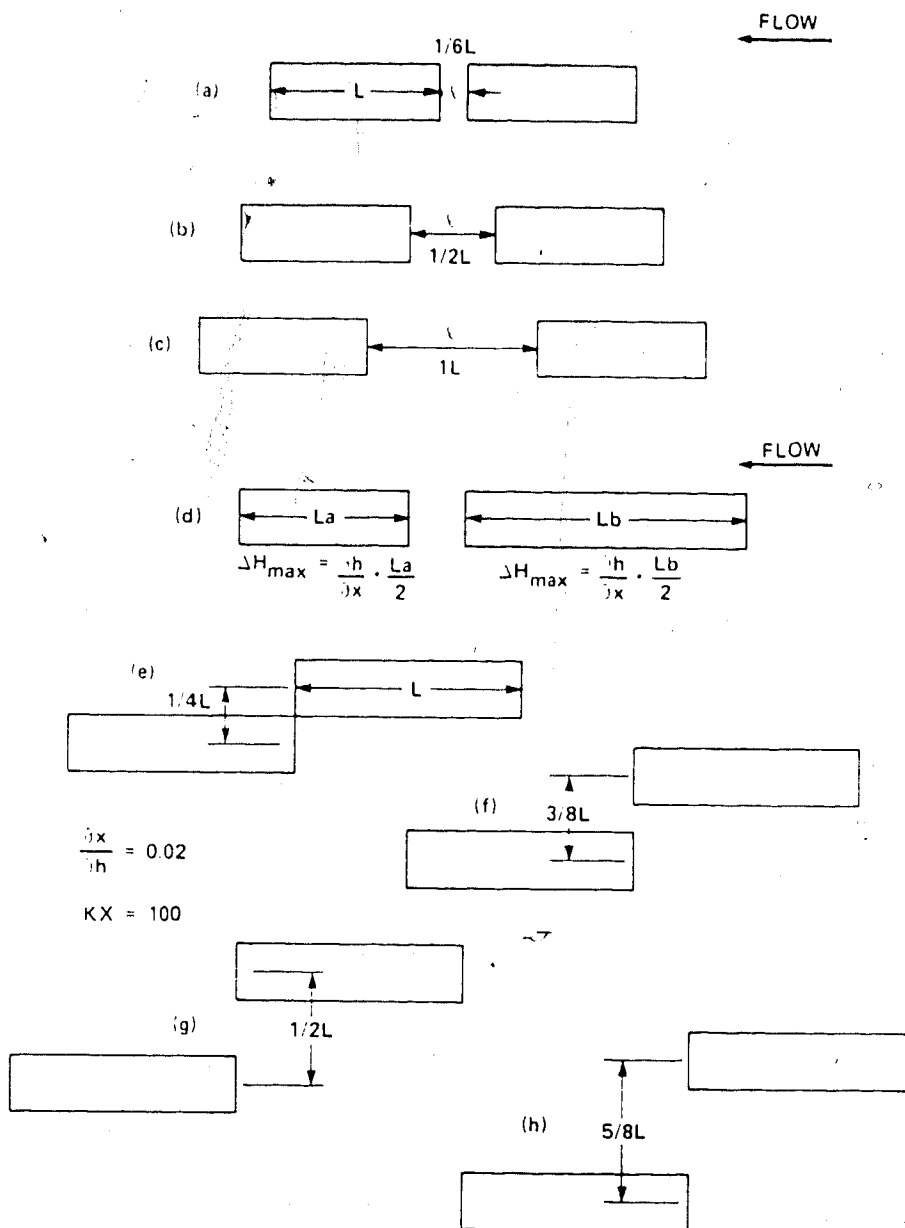


Figure 5.4 Multiple lens configurations used to determine interference effects (anomaly shift  $\Delta\Phi_i$ ) with, horizontal separation (a-d) and vertical separation (e-g) .

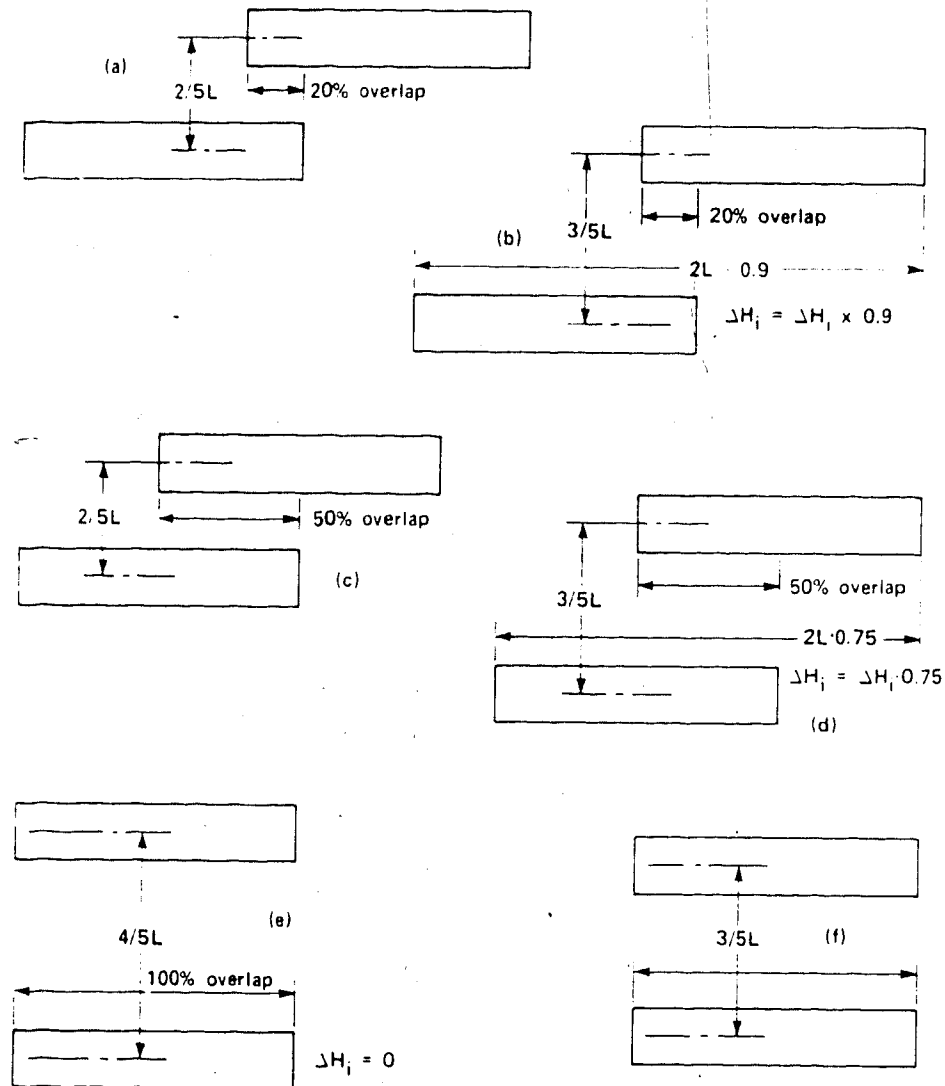


Figure 5.5 Multiple lens configurations used to determine reduction in anomaly shift ( $\Delta\Phi_1$ ) with progressive overlap of subjacent lenses.

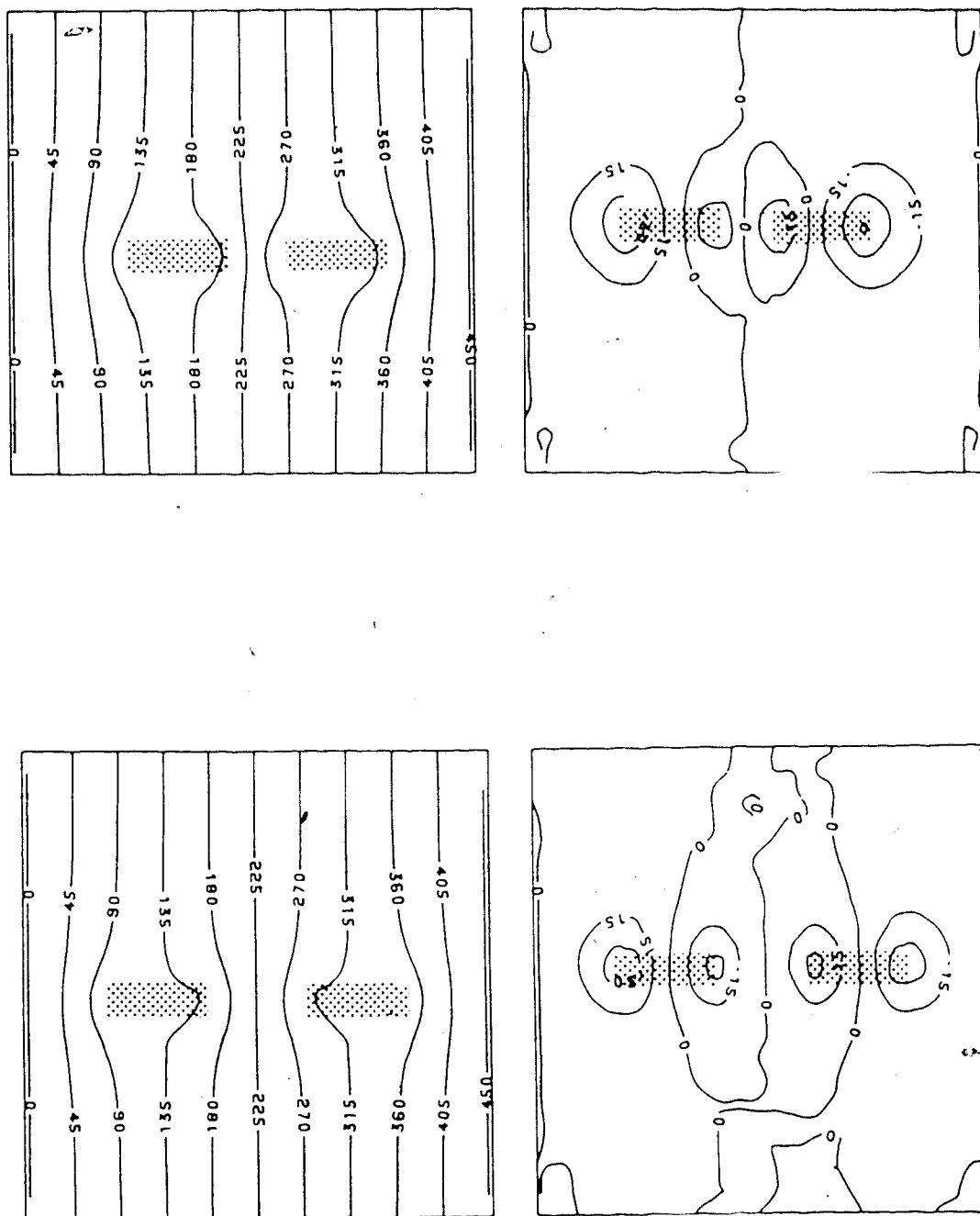


Figure 5.6 Potentiometric surface and anomaly maps due to interference effect of adjacent lenses, separation  $l/L = 1/6$  a, b and  $l/L = 1/2$  c, d.

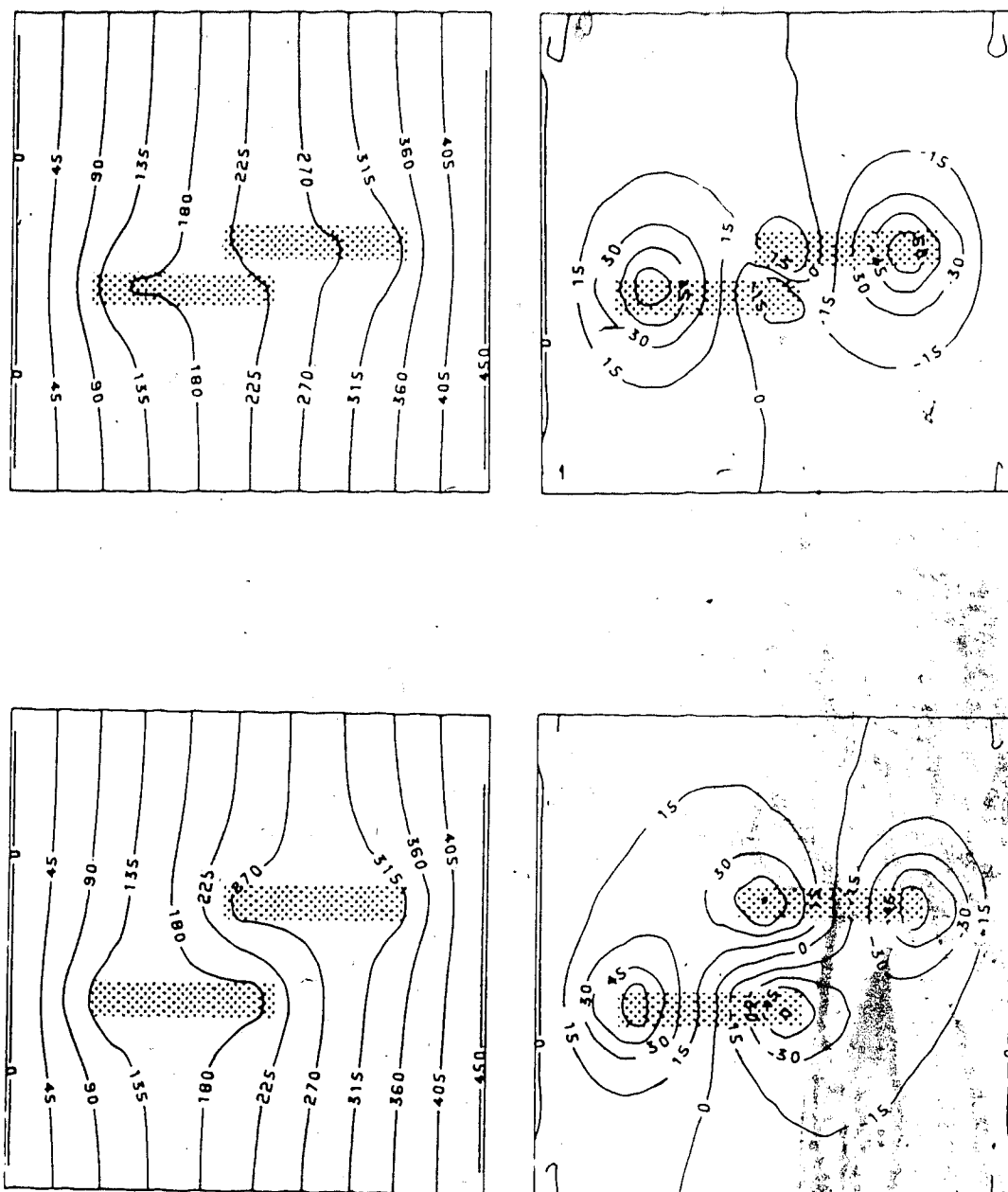


Figure 5.7 Potentiometric-surface and anomaly maps for subjacent lens with vertical separation of  $l/L = 1/4$  a, b and  $l/L = 3/5$  c, d.

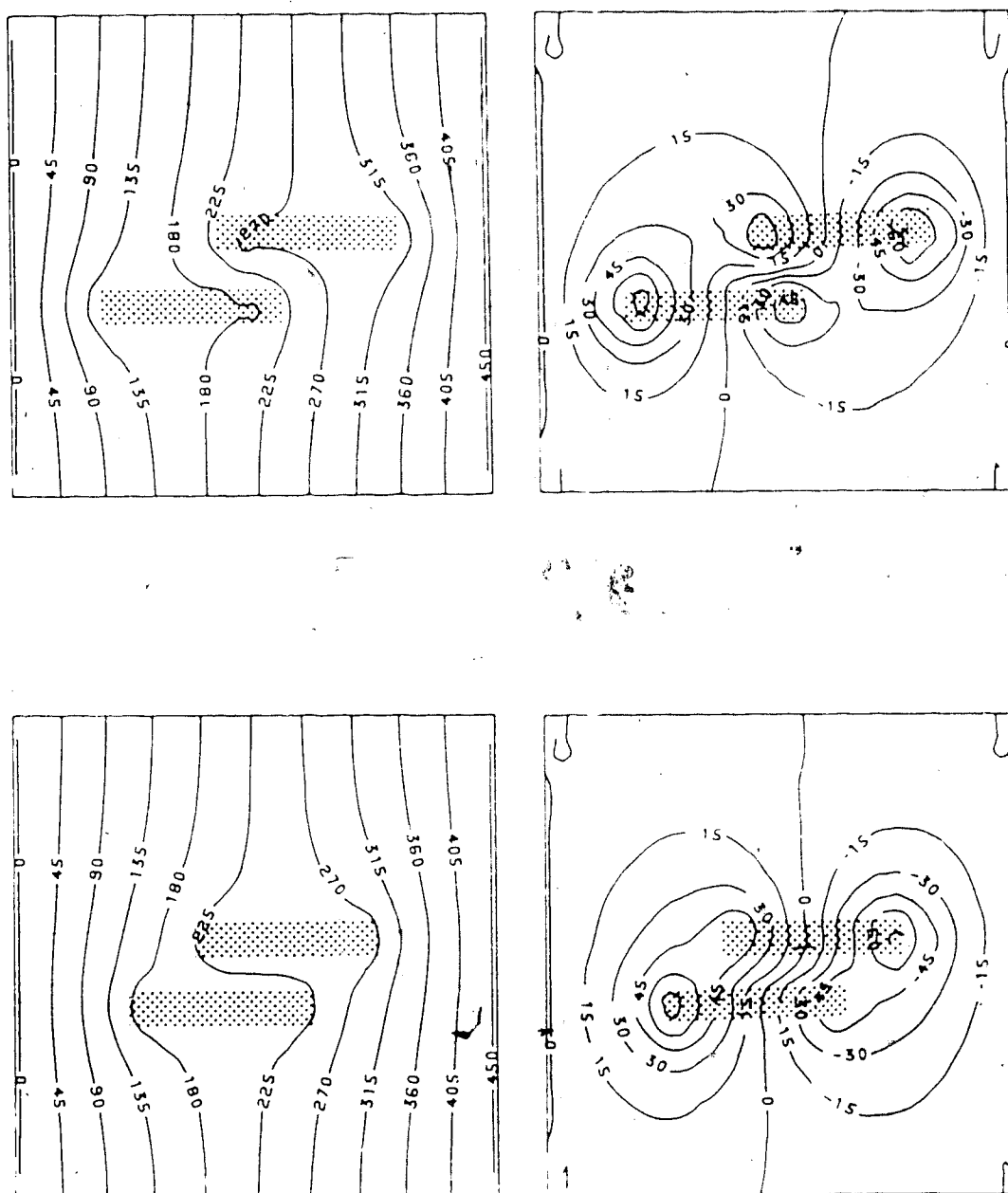


Figure 5.8 Potentiometric surface and anomaly maps for subadjacent lenses with a vertical separation of  $l/L=2/5$  and overlap of 20% a, b and 50% c, d.

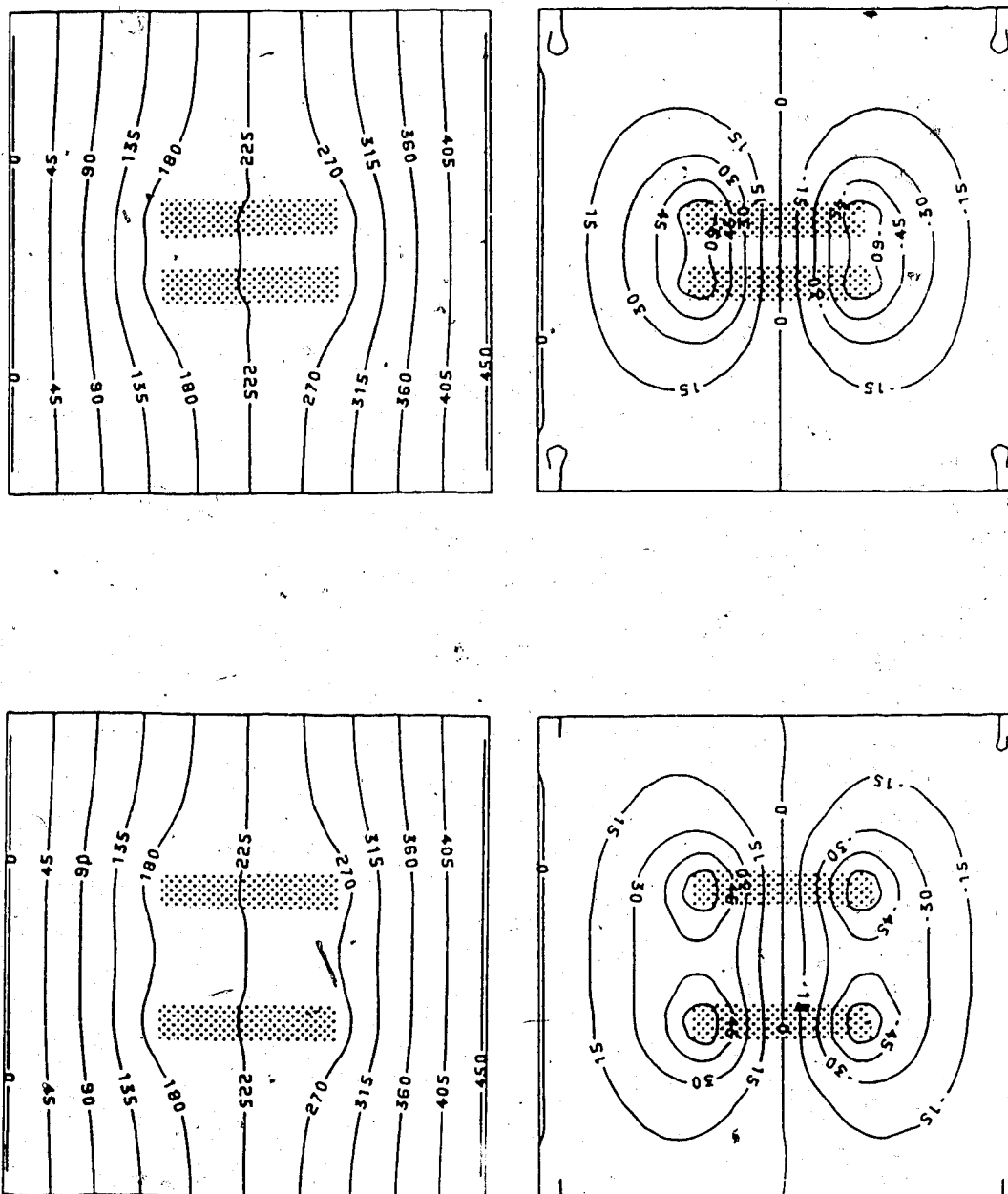


Figure 5.9 Potentiometric surface and anomaly maps for subadjacent lenses with 100% overlap and vertical separation of  $l/L = 3/5$  a, b and  $4/5$  c, d.

This figure has been omitted due to copyright restrictions on the material.

Source :

Tóth, J., and T. Corbet, 1986, Post-Paleocene evolution of regional groundwater flow-systems and their relation to petroleum occurrences, Taber area, southern Alberta, Canada :  
Bulletin of Canadian Petroleum Geology, vol.34, no.3, pp. 339-363.

Figure Number : 25

Page Number : 358



This figure has been omitted due to copyright restrictions on the material.

Source :

Tóth, J., and T. Corbet, 1986, Post-Paleocene evolution of regional groundwater flow systems and their relation to petroleum occurrences, Taber area, southern Alberta, Canada :  
Bulletin of Canadian Petroleum Geology, vol.34, no.3, pp. 339-363.

Figure Number : 26

Page Number : 359

This figure has been omitted due to copyright restrictions on the material.

Source :

Tóth, J., and T. Corbet, 1986, Post-Paleocene evolution of regional groundwater flow-systems and their relation to petroleum occurrences, Taber area, southern Alberta, Canada :  
Bulletin of Canadian Petroleum Geology, vol.34, no.3, pp. 339-363.

Figure Number : 27

Page Number : 360

Leaf 154 omitted in page numbering

# Appendix 4B.1 - Description of cores logged in the Keho Lake study area

Well name CS et al Keho 6-13

Location 6-13-12-22W4M (1071-1087m)

Status

1. Column Shows	2. Porosity Type	3.	4. Lithology	5. Grain or Crystal size	Description	
		Porosity %				
		>20 12-20 6-12 0-6		clay silt v. f. gr. ss. m. gr. ss. c. gr. ss. v. c. gr. ss.		
1070'					Shale, black, blocky, ~15-20% silt. strg. minor shell frag.	BF Sc. Shale
1071'					S.S. lam. ~1.5", med. gr. (calc. cem.)	
1075'			P		pyrite nodule in s.s.	Bow Island S.S.
Kc avg. range					S.S., v. coarse, min. pebbles - sh. strg., scoured lower contact with 3" bentonite	
1-10 md					Bentonite - gy, v. f. gr. S.S., med. gr., min. calc. cement	
10-40 md					S.S. f. gr., wispy sh. lam., porous, min. silt. cement ↓ poor porosity	Bow Island S.S.
8-5 md					— escape burrows, 1/2" x 4"	
<10 md					↓ increasing silt./sh. lam.	Bow Island S.S.
1085'					S.S. - siltst., v. f. gr., extensively bioturb. destroys por. and perm.	
1087'						Ist.

Well name CS et al Keho 6-1Location 6-1-12-22W4M (1054-1064m)Status           

1.	2.	3.	4.	5.	
Column	Porosity Type	Porosity %	Lithology	Grain or Crystal size	Description
Shows		$\frac{20}{12}$ $\frac{20}{12}$ $\frac{20}{12}$		clay silt v. f. g. s. f. g. s. m. g. s. c. g. s. v. c. g. s.	
1050m					
1054m					Shale, blk. - gy., blocky - fiss. ~ 10% siltst. strg.
					BFsc Shales
					S.S., med. gr., 5 cm. Congl., chert. pebbles, ~ 10 cm. S.S., v. f. - f. gr., gy - blk., ~ 25% discont. SA. strg.
					Bow Is. Fm.
					k(md) Horiz. (max.) average kc 0.4, max. 88 md @ Congl. k <sub>bst</sub> 100 md

$\uparrow$   
 kc  
 1064m  
 k<sub>bst</sub> 1063-1070  
 $\downarrow$

Status

1.	2.	3.	4.	5.
Column Shows	Porosity Type	Porosity % <small>&gt;20 12-20 6-12 ≤6</small>	Lithology	Grain or Crystal size <small>clay silt v.f.g. f.g. m.g. c.g. v.c.g.</small>
970m				
972m				
975m				
980m				
985m				
Kc, 988				
990m				

Description

Shale, blk.-gy., mass. - blkcy.  
minor fract.  
f.-med. s.s. strgs.-lens., ~10%.

Congl., cht. pebb., ~8" (20cm.), lite clay-calc. cem.  
sh.-sltst., gy-blk., interlam (50-50%)  
S.S., gy-blk., vf.-f.gr., abndt. sh.-sltst prtg., bioturb., ~10%, med. gr. s.s. lens.  
Congl., cht. pebb., ~6" (15cm.), calc. cem.  
S.S., as above  
Bentonite, gy, v.f.gr.  
S.S., f.gr-v.f.gr., ~15% sh.-sltst. prtg.

bioturbation reduced.

Kc(md.) Horiz. @90° Vert.  
Kc, 0.11 — 0.10 0.2? fract.

BFSC SHALE

1ST BOW ISLAND SS







Well name Onyx et al Keho 14-10Location 14-10-12-21W4M (956-969m)Status 

1.	2.	3.	4.	5.	
Column	Porosity Type	Porosity %	Lithology	Grain or Crystal size	Description
Shows		>20 12-20 6-12 <6		clay silt v. f. g. ss. mg. ss. c. g. ss. v. c. g. ss.	
956m					Shale, blk.-gy., blocky-fiss., ~10% siltst.-f. gr. s.s. strg., minor oil stn.
					Bentonite, gy-whit., soft, ~15cm.
					Siltst., gy-blk.,
					Shale, as above
					Siltst., gy-blk.,
					Shale, as above
					Congl., cnt. pebb., poorly cemented, oil stained (3m total thickness indicated on gamma-ray log)
969m					
					k(md) avg. Horz (max.)
					k <sub>c</sub> 5079 (Congl.)
					k <sub>ost</sub> 5571

BFSc Shales

Bow Is.



Well name Onyx et al Keho 16-9

Location 16-9-12-21W4M (966-971.4m) Status

[illegible]

452

100

## Status

163

Well name CH et al Horsefly 10-19Location 10-19-8-18W4M (800-811m)Status         

1.	2.	3.	4.	5.	Description			
Column Shows	Porosity Type	Porosity %	Lithology	Grain or Crystal size				
		<div> <div>&gt;20</div> <div>12-20</div> <div>6-12</div> <div>&lt;6</div> </div>		<div> <div>clay</div> <div>silt</div> <div>v. f. g. s.</div> <div>mg. s.</div> <div>co. s.</div> </div>				
800m					ss., vfg., gy-brwn, poss. light oil stain siltst. - shale, blk. - gy, lenticular Congl., cht. pebb. (avg 3mm, max 1cm), calc. cement ss., med. gr., gy, minor silt. lam., coarsening up Shale, blk. - gy, mass., ~20% silt. at top as discont. lam., strg. and nodular			
					siltst., ~30cm, w discont. sh. lam., bioturb. shale, blk., mass., soft, bedding plane fract. siltst., gy-blk w discont. sh. strg. ~30% ss., fine-med gr., gy, scoured lower cont. siltst., gy-blk., discont. sh. strg., minor ss.			
811m					ss., f. gr., gy-wht, mass., minor wispy sh.			
KOST (809-822m)								
					k(md)    Horz.    @90°    Vert.			
					kc <sub>1</sub> 4.3    3.5    0.8			
					kc <sub>2</sub> 55    54    49			
					K <sub>DST</sub> 102			

Well name Imperial Chin 7-10Location 7-10-9-18W4M (2625-2301, 2405-2437') Status 

1.	2.	3.	4.	5.		
Column Shows	Porosity Type	Porosity	Lithology	Grain or Crystal size	Description	
		%				
		<div><div>&gt;20</div><div>12-20</div><div>6-12</div><div>&lt;6</div></div>		<div>clay silt v. f. g. f. g. m. g. c. g. v. c. g.</div>		
2265ft.					S.S., f. gr., wht., mass. Shale, blk., blocky	
					S.S., f. med gr., wht., clean to sfp; v good perm.	
2301ft.					minor sh. lam.	
2405ft.					Shale, blk., blocky	
					S.S., f. gr., clean - wht - sfp	
					minor shal. strg.	
2437ft.					Siltst. - v. f. gr. s. s. minor sh. lam., some org.	

